Near field characterization of plasmonic nanostructures with electron energy loss spectroscopy

Dissertation

zur
Erlangung des Doktorgrades (Dr. rer. nat.)
der
Mathematisch-Naturwissenschaftlichen Fakultät
der
Rheinischen Friedrich-Wilhelms-Universität Bonn

vorgelegt von

Felix von Cube

aus
Neuss

Bonn 2014

Angefertigt mit Genehmigung der Mathematisch-Naturwissenschaftlichen Fakultät der Rheinischen Friedrich-Wilhelms-Universität Bonn

CONTENT

Chapter 1

Introduction

Over the past years, metallic nanostructures and their properties became one of the most active research areas in optics. Mostly, this can be attributed to their ability to focus light into subwavelength volumes. The intensity of the focused light thereby outranges the incident light intensity by orders of magnitude. Therefore, metallic nanoparticles are interesting for many fields of application, for example in nonlinear optics, solar cells, subwavelength optical waveguides, and photonic metamaterials. In particular, photonic metamaterials offer many new and exciting optical properties not available in natural materials. Besides the focusing of light, there can be e.g., magnetism at optical frequencies [1–3], a negative index of refraction [4,5], or strong chirality [6–8]. In most cases these properties can be attributed to the excitation of collective electron oscillations (so-called plasmonic modes) in the elementary building blocks ("'meta-atoms"') of a photonic metamaterial. The characteristics of plasmonic modes, in particular the electromagnetic near field distribution, can be tailored by their morphology and the dielectric environment.

Up to now most experimental studies on photonic metamaterials have concentrated on the far field by observing optical extinction or scattering spectra. There are a few optical techniques that even allow for the investigation of individual plasmonic nanostructures, e.g., attenuated total reflectance (ATR) spectroscopy [9], or a spatial modulation technique [10,11]. However, the in-depth understanding of the optical properties of a given photonic metamaterial requires the knowledge of the electromagnetic near field distribution. For this reason, electromagnetic field calculations based on efficient numerical schemes have become an essential tool for the metamaterial design process. Experiments capable of determining the spectral and spatial distribution of plasmonic modes with nanometer spatial resolution are required to verify such calculations and to study for example, the influence of structural imperfections.
Recently, it has been shown that electron energy loss spectroscopy (EELS), in combination with scanning transmission electron microscopy (STEM) is a powerful tool for the spatio-spectral characterization of plasmonic modes of metallic nanostructures [12–16]. This method relies on the fact that plasmons cannot only be excited by light, but also by fast moving electrons, as present for example in a transmission electron microscope

1

(TEM). Indeed the first prediction of plasmons was made in 1957 by R. Ritchie, who considered "a fast electron losing energy to the conduction electrons" in metals [17]. The crucial advantage of fast electrons is their short de Broglie wavelength of around 3 pm (for 200 kV acceleration voltage), which allows for interactions with the sample on very small dimensions.

In STEM-EELS, a tightly focused electron beam is raster scanned across the sample (focus diameter well below 1 nm, even for standard STEMs). A fast electron passing near or through the metallic nanostructure can excite one of the plasmonic modes resulting in an energy loss of the electron equal to the plasmonic resonance energy ($\hbar\omega \approx 1\,\mathrm{eV}$). Different plasmonic modes can therefore be distinguished by their resonance energies. By recording an energy loss spectrum for each position of the electron beam, one can map the spectral and spatial distribution of the plasmonic modes with nanometer resolution. So far, the majority of plasmon related experiments with electron microscopes have dealt with chemically synthesized metallic nanoparticles [12, 18–22]. However, in the context of plasmonics and photonic metamaterials, chemical synthesis is often not an option as it offers insufficient control over size, shape, and relative orientation of the metallic nanoparticles. Recently, some research groups have addressed this issue with lithographically defined metallic nanostructures [15, 23, 24].

In a first metamaterial related study, G. Boudarham et al. reported on spectral imaging of the four lowest-order plasmon modes of a silver split-ring resonator (SRR) [15]. The SRR is one of the paradigm metamaterials; it is a subwavelength metallic ring with one slit, and its eigenmodes have been identified as plasmonic standing waves with many characteristics resembling those of straight nanoantennas. Furthermore, plasmon mapping with electron microscopes was applied to a variety of metallic nanostructures such as nanotriangles [18, 25], nanorods and nanowires [19, 26], dimer structures [12, 13, 27], bow-tie antennas [24], nanodisks [14], and apertures in metal films [16].

In this thesis, STEM-EELS is used to characterize the near field of plasmonic nanostructures and the results are compared to optical experiments as well as numerical simulations.

Outline of this Thesis
Chapter 2 begins with the description of classical electrodynamics, the Drude model is used to explain the basic concepts of plasmons on surfaces and nanoparticles, and the excitation process of plasmons with fast moving electrons is explained. A more general introduction to metamaterials is given with a focus on split-ring resonators (SRRs) and their plasmonic behavior. The generalized Babinet's principle is introduced, which associates the electric and magnetic near fields of complementary nanostructures. Finally, the coupling behavior of two or more Lorentz oscillators is discussed. In chapter 3, the fabrication of nanostructures on electron transparent substrates via electron beam lithography is described. An emphasis is put on the STEM-EELS acquisition procedure, and the used transmission electron microscope, with its three non-standard components. Additionally, an optical setup to measure extinction spectra is presented and the basics of the simulation method are introduced.

Chapter 4 gives an understanding of how to interpret EELS measurements and plasmonic resonances using the example of an individual split-ring resonator. Furthermore, a complementary SRR is investigated to verify Babinet's principle. In chapter 5, the plasmon excitation with electrons is compared to the excitation with light. Chapter 6 elucidates coupling effects between two and more nanoparticles and in chapter 7, angular-resolved EELS is performed to investigate the three dimensional field distribution of a plasmon. Chapter 8 summarizes this thesis and provides a glimpse into future projects.

CHAPTER 2

FUNDAMENTALS

This chapter describes the fundamentals of electromagnetism in order to explain the behavior of localized plasmonic modes. In particular, it starts with Maxwell's equations and follows with a description of metallic particles in oscillating electromagnetic fields. This leads directly to the properties of plasmons, for which a closer look is presented on the excitation process of plasmons with fast electrons. The split ring resonator, as one of the most prominent examples of a metamaterial, will be discussed in detail and Babinet's principle is introduced to inter-relate the electric and magnetic near field of nanoparticles and their complementary structure. Finally, the coupling of two or more nanoparticles is analyzed.

2.1 Classical electrodynamics

2.1.1 Maxwell's equations

The behavior of electromagnetic fields within a medium are fully described by a set of equations, derived by James Clerk Maxwell in 1864 [28]. In SI-units they read:

$$\nabla \cdot \boldsymbol{D}(\mathbf{r}, t) = \frac{1}{\epsilon_0} \rho(\mathbf{r}, t), \tag{2.1}$$

$$\nabla \cdot \boldsymbol{B}(\mathbf{r}, t) = 0, \tag{2.2}$$

$$\nabla \times \boldsymbol{E}(\mathbf{r}, t) = -\partial_t \boldsymbol{B}(\mathbf{r}, t), \tag{2.3}$$

$$\nabla \times \boldsymbol{H}(\mathbf{r}, t) = \mu_0 \epsilon_0 \partial_t \boldsymbol{D}(\mathbf{r}, t) + \mu_0 \boldsymbol{j}(\mathbf{r}, t), \tag{2.4}$$

where $\boldsymbol{D}(\mathbf{r}, t)$ is the dielectric displacement, $\boldsymbol{B}(\mathbf{r}, t)$ is the magnetic induction, $\boldsymbol{E}(\mathbf{r}, t)$ is the electric field, $\boldsymbol{H}(\mathbf{r}, t)$ is the magnetic field, $\rho(\mathbf{r}, t)$ is the charge density, $\boldsymbol{j}(\mathbf{r}, t)$ is the current density, $\epsilon_0 = 8.85 \times 10^{-12} \text{F/m}$ is the permittivity in free space, and $\mu_0 = 4\pi \times 10^{-7} \text{N/A}^2$ is the permeability in free space. The latter two are connected via $\sqrt{\epsilon_0 \mu_0} = \frac{1}{c_0}$.

The electric and magnetic fields are related to the dielectric displacement and the magnetic induction via:

$$\boldsymbol{D}(\mathbf{r},t) \;=\; \epsilon_0 \boldsymbol{E}(\mathbf{r},t) + \boldsymbol{P}(\mathbf{r},t), \tag{2.5}$$

$$\boldsymbol{B}(\mathbf{r},t) \;=\; \mu_0 \boldsymbol{H}(\mathbf{r},t) + \boldsymbol{M}(\mathbf{r},t), \;, \tag{2.6}$$

here, the electric polarization $\boldsymbol{P}(\mathbf{r},t)$ and the magnetization (or magnetic polarization) $\boldsymbol{M}(\mathbf{r},t)$ were introduced. The two vector fields $\boldsymbol{P}(\mathbf{r},t)$ and $\boldsymbol{M}(\mathbf{r},t)$ express the density of permanent or induced electric/magnetic dipole moments in a material. Equations 2.5 and 2.6 can be rewritten as:

$$\boldsymbol{D}(\mathbf{r},t) \;=\; \epsilon_0 \epsilon(\omega) \boldsymbol{E}(\mathbf{r},t), \tag{2.7}$$

$$\boldsymbol{B}(\mathbf{r},t) \;=\; \mu_0 \mu(\omega) \boldsymbol{H}(\mathbf{r},t). \tag{2.8}$$

Here, the effective material parameters $\epsilon(\omega)$ and $\mu(\omega)$ were introduced, representing the permittivity and permeability, respectively. They describe how an electric/magnetic field affects (and is affected by) a medium. In case of an oscillating field, both are a function of the frequency ω.

2.1.2 The Drude model

In 1900 Paul Drude introduced a theory to describe the transport of electrons in materials and especially in metals [29]. The model assumes that conduction electrons move freely with respect to a fixed crystal, formed by the atoms. The movement of the electrons can be described by the kinetic gas theory, which led to the nomenclature *free electron gas*. The only interactions considered within this free electron gas are instantaneous collisions; long-range interactions between ions and electrons or among electrons are neglected.
In an external electric field, the electrons experience a force $\boldsymbol{F}$ proportional to the electric field $\boldsymbol{E}$: $\boldsymbol{F} = -e\boldsymbol{E}$, with e being the elementary charge. In case of an incident electromagnetic wave, the electric field is time dependent, and can be expressed as $\boldsymbol{E}(t) = E_0 e^{-\imath\omega t}$. For the free electron gas this leads to the equation of motion for a harmonic oscillator:

$$m_e \ddot{\boldsymbol{x}} + m_e \gamma_{\mathrm{D}} \dot{\boldsymbol{x}} \;=\; -e \cdot \boldsymbol{E}(t). \tag{2.9}$$

Where m_e is the effective mass of the electron, $\boldsymbol{x}$ corresponds to the displacement of the electron and γ_{D} is the damping ($\gamma_{\mathrm{D}} = 1/\tau$, with τ being the mean free time between collisions). The ansatz $\boldsymbol{x}(t) = \boldsymbol{x}_0 e^{-\imath\omega t}$ leads to the oscillation amplitude:

$$\boldsymbol{x}_0 \;=\; \frac{e\boldsymbol{E}_0}{\mathrm{m_e}} \left(\frac{1}{\omega^2 + \imath\gamma_{\mathrm{D}}\omega} \right). \tag{2.10}$$

For the electric polarization $\boldsymbol{P}$ of the free electron gas the density of charges n is introduced, which leads to:

$$\boldsymbol{P} = -ne \cdot \boldsymbol{x} = -\frac{ne^2}{m_e}\left(\frac{1}{\omega^2 + \imath\gamma_{\mathrm{D}}\omega}\right)\boldsymbol{E}. \tag{2.11}$$

From 2.5 one can derive the dielectric function of a metal in the Drude model:

$$\epsilon_{\mathrm{D}}(\omega) \;=\; 1 - \frac{\omega_{\mathrm{pl}}^2}{\omega^2 + \imath\gamma_{\mathrm{D}}\omega}, \tag{2.12}$$

with the plasma frequency $\omega_{\mathrm{pl}} = \sqrt{\frac{ne^2}{\epsilon_0 m_e}}$. It was empirically shown that an offset ϵ_∞ has to be added to 2.12, in order to consider the influence of the atomic cores, resulting in:

$$\epsilon_{\mathrm{D}}(\omega) \;=\; \epsilon_\infty - \frac{\omega_{\mathrm{pl}}^2}{\omega^2 + \imath\gamma_{\mathrm{D}}\omega}. \tag{2.13}$$

This model is a fairly good description of the behavior of metals at frequencies in the near-infrared region. For shorter wavelengths (higher energies) one has to account for excitations of electrons from lower bands into the conduction band, i.e. interband transitions, which can be triggered by an externally applied electric field [30]. These interband transitions occur for example in gold at an energy of $2.38\,\mathrm{eV}$ ($522\,\mathrm{nm}$), where an electron from the $5d$-band (valence band) is excited into the $6s$-band (conduction band). To improve the description of the permittivity for shorter wavelengths, a common ansatz is to accompany the Drude model with Lorentz oscillators [31, 32].

The Drude-Lorentz model
In the equation of motion 2.9 the Lorentz oscillators are taken into account by adding the term: $m_e\omega_0^2\mathbf{x}$, where ω_0 is the eigenfrequency of the undriven Lorentz oscillator. With the same procedure as before one gets a permittivity which can be added to the permittivity of the Drude Model 2.13, expressed as:

$$\epsilon(\omega) \;=\; \underbrace{\epsilon_\infty - \frac{\omega_{\mathrm{pl}}^2}{\omega^2 + \imath\gamma_{\mathrm{D}}\omega}}_{Drude} + \underbrace{\sum_j \frac{\Delta\epsilon_{\mathrm{L},j}\cdot\omega_{0,j}^2}{\omega^2 - \omega_{0,j}^2 - \imath\gamma_{\mathrm{L},j}\omega}}_{Lorentz}. \tag{2.14}$$

The sum accounts for several Lorentz oscillators, where $\Delta\epsilon_{\mathrm{L}} = \frac{\omega_{\mathrm{pl}}^2}{\omega_0^2}$ is the strength of the oscillator. Equation 2.14 can be used to simulate the permittivity in nanoparticles. In this respect, the oscillator strength $\Delta\epsilon_{\mathrm{L}}$ was introduced to add another fit parameter. Apart from the fit parameters of the Drude model ($\epsilon(\omega)$, ω_{pl}, and γ_{D}), this leads to three additional fit parameters: ω_0, γ_{L}, and $\Delta\epsilon_{\mathrm{L}}$ [33], which are needed to accurately model the behavior of metals at optical frequencies. The values are defined in section 3.4, where the simulations are explained in detail.

2.2 Plasmons

The collective oscillation of a free electron gas is also called a plasma oscillation. This oscillation can be quantized, with the plasmon being its quantum. This is analogous to a phonon, which is the quantum of mechanical vibrations. Plasmons coupling with a photon form a new quasi-particle, the plasmon polariton. The properties of the plasmon (-polariton) strongly depend on the shape of the metal. Plasmons can exist in bulk materials, on 2D interfaces, on 1D wires, and on nanoparticles. A special interest of this work lies on the latter case.

2.2.1 Surface plasmon polaritons

The propagation of waves in a homogeneous medium is described by Maxwell's equations, and the influence of electric fields on charged particles in a metal is described by the Drude-Lorentz model. Combining those two, one considers now the interface of a dielectric and a metal, where waves are allowed to propagate along the interface. These waves are called surface plasmon polaritons (SPP) and exhibit an exponential decay of the amplitude in the dielectric as well as in the metal. Let the interface be in the xy-plane ($z = 0$) and
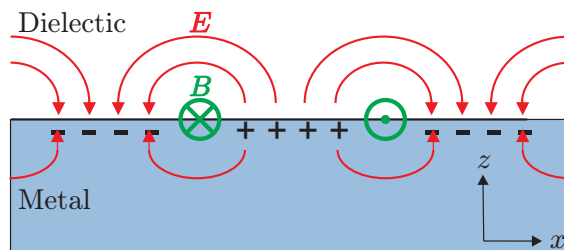

Figure 2.1: Schematic view of a surface plasmon polariton, bound to the interface between a metal and a dielectric. The charges as well as the electromagnetic fields are shown.

the propagation of the SPP be in the x-direction. For values of $z > 0$ there is a dielectric with $\epsilon = \epsilon(\mathbf{r}) = \epsilon_\mathrm{D}$ and for $z < 0$ a metal with $\epsilon = \epsilon(\mathbf{r}, \omega) = \epsilon_\mathrm{M}(\omega)$. The eigenmodes of the SPP can be described by Maxwell's equations and therefore are solutions of the differential equation [34]:

$$\nabla \times \nabla \times \boldsymbol{E}(\mathbf{r}, \omega) - \frac{\omega^2}{{c_0}^2} \epsilon(\mathbf{r}, \omega) \boldsymbol{E}(\mathbf{r}, \omega) = 0. \tag{2.15}$$

Since the SPP travels in the x-direction one is looking for real values of the dispersion relation in this direction (k_x):

$$k_\mathrm{x}^2(\omega) = \frac{\epsilon_\mathrm{M}(\omega)\epsilon_\mathrm{D}}{\epsilon_\mathrm{M}(\omega) + \epsilon_\mathrm{D}} \frac{\omega^2}{{c_0}^2}. \tag{2.16}$$

Comparing 2.16 with the dispersion relation for light ($k = \omega/c$) one finds that light cannot directly excite SPPs (for details see [34,35]). To overcome the wave vector mismatch a few methods have been introduced. The two most famous are an attenuated total reflection geometry (Otto [36] and Kretschmann [37] configuration) or a grating coupler [38].

SPPs can also be excited very efficiently by fast moving electrons [17], as is done in this work in a transmission electron microscope. In this case one does not have to account for a momentum mismatch. The fast moving electron is associated with an electric field, which evokes a sharp rise of the surface charges (see section 2.2.5).

2.2.2 Particle plasmons

In this section the confinement of the electron oscillation to a well-defined but in principle arbitrary volume is described. As was seen before, an external electric field accelerates the conduction band electrons in one direction. In a small metal particle, the free moving electrons thus travel to one side of the particle and form a negative charge density. On the opposite side of the particle the positive background remains and forms a positive charge density. This charge separation gives rise to an electric field and a restoring force acting on the electrons, resulting in a coherent plasma oscillation [31] (see fig. 2.2). Due to the confinement to the metal particle, one refers to this oscillation as particle plasmon. In contrast to SPPs, particle plasmons can be directly excited by light as well as by fast moving electrons.

For a better understanding of particle plasmons, first a metal sphere in the quasi-static regime is considered, i.e., the radius of the sphere (r_s) is much smaller than the vacuum wavelength of the considered electromagnetic wave. In this case the particle plasmon can to a first approximation be described using classical electrostatic theory and retardation effects can be neglected. In an external electric field $\boldsymbol{E}_0$ the free charges become separated and an internal electric field $\boldsymbol{E}_\mathrm{int}$ arises, given by [28]:

$$\boldsymbol{E}_\mathrm{int} \;\; = \;\; \boldsymbol{E}_0 \frac{3\epsilon_\mathrm{D}}{\epsilon_\mathrm{M}(\omega) + 2\epsilon_\mathrm{D}} \,, \tag{2.17}$$

with ϵ_D and $\epsilon_\mathrm{M}(\omega)$ being the permittivity of the environment and the metal, respectively. In the case of neglected retardation effects, 2.17 is also valid for oscillating external electric fields. Since the permittivity of a metal ($\epsilon_\mathrm{M}(\omega) = \epsilon'_\mathrm{M}(\omega) + \imath\epsilon''_\mathrm{M}(\omega)$) shows a frequency dependence, one can expect a resonance behavior of the metal particle. Assuming the imaginary part to be negligible ($\epsilon''_\mathrm{M}(\omega) \ll 1$) the resonance condition reads: $\epsilon'_\mathrm{M}(\omega) = -2\epsilon_\mathrm{D}$. The electrons oscillate with the frequency of the external field. If the frequency of the external field hits the resonance frequency of the metal particle, the internal field will be drastically enhanced. This field enhancement is not only present inside the metal particle, but also in the near surroundings of the particle. The local intensity in the vicinity of the nanostructures can exceed the incident light intensity by orders of magnitude. This effect can lead to enhanced light-matter interaction and is an important motivation for various
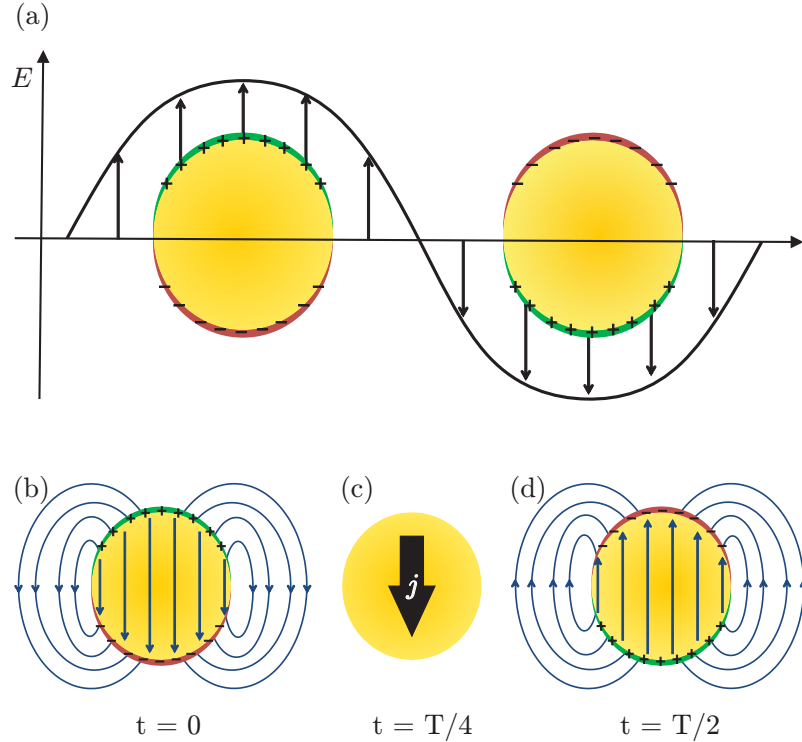
Figure 2.2: (a) Schematic view of an electromagnetic wave interacting with a gold sphere. The free conduction electrons in the sphere move according to the external field. In (b-d) the oscillation of a particle plasmon is sketched for different times. The charge separation is followed by an electrical current j, which is then followed by a charge separation. The electric field of the charge separation is indicated by blue lines. When the external electric field oscillates at the eigenfrequency of the nanoparticle, the internal electric field is resonantly enhanced.

research activities in the field of plasmonics, e.g., for plasmonic sensing applications [39], optical antennas [40], nonlinear plasmonics [41], or quantum plasmonics [42]. Effects like surface-enhanced Raman scattering (SERS) [43, 44], or nonlinear optical effects [45, 46] are also based on this field enhancement.

For particles in the quasi-static regime the dominant oscillation mode is the dipole mode (see fig. 2.2). Nevertheless higher order oscillation modes are possible, especially when the particle size is increased. To describe spherical particles with a diameter in the range of the considered electromagnetic wavelength, one can use the Mie theory [47].

In 1908 Gustav Mie introduced a theory to determine the optical scattering, absorption and extinction cross-sections of spherical nanoparticles [47]. He solved Maxwell's equations in spherical coordinates on the surface of a nanoparticle for an incident plane wave. To describe the optical properties he used the absorption cross-section σ_{abs} and the scattering cross-section σ_{scat}. Both of them contribute to losses from the incident beam, thus the total extinction cross-section σ_{ext} is defined by: $\sigma_{\mathrm{ext}} = \sigma_{\mathrm{abs}} + \sigma_{\mathrm{scat}}$. The extinction

and scattering cross-sections are:

$$\sigma_{\text{ext}} \quad = \quad \frac{2\pi}{|k|^2} \sum_{n=1}^{\infty} (2n+1) \cdot \text{Re}(a_n + b_n), \text{ and} \tag{2.18}$$

$$\sigma_{\text{scat}} \quad = \quad \frac{2\pi}{|k|^2} \sum_{n=1}^{\infty} (2n+1) \cdot (|a_n|^2 + |b_n|^2). \tag{2.19}$$

Here, k is the wave vector and a_n and b_n are expansion coefficients which incorporate the size and dielectric function parameters of the nanoparticle and the surrounding medium. The summation accounts for the multipole excitations (n=1: dipole mode, n=2: quadrupole mode, etc.).

2.2.3   Plasmon excitation with electrons

Surface plasmons were originally predicted for an electron beam that penetrates a thin metal film and thereby transfers energy to the plasmon [17]. Shortly after the prediction, plasmons were experimentally confirmed via electron energy loss spectroscopy (EELS) [48]. Before the excitation of particle plasmons via fast moving electrons is described, the local density of states (LDOS) is introduced. The LDOS describes the density of states (i.e., the number of states per energy interval that can be occupied by photons) at a certain position. In terms of formulae, one starts with Fermi's Golden Rule, which describes the spontaneous decay rate of an excited two-level atom, and proceeds with rewriting the LDOS in the eigenmodes of the system. This section closely follows the description given in [34, 49].

2.2.4   Local density of states (LDOS)

First, the decay rate γ of a two-level atom is considered. The decay rate increases with an increasing number of electromagnetic states that are available in the near surrounding of the atom. It can be described by Fermi's Golden Rule [34]:

$$\gamma \quad = \quad \frac{2\pi}{\hbar^2} \sum_{f} |\langle f|\hat{H}_{\text{I}}|i\rangle|^2 \delta(\omega_{\text{i}} - \omega_{\text{f}}) \,, \tag{2.20}$$

where $\hbar$ is Planck's constant, $|f\rangle$ denotes the final (ground) state of the atom, $|i\rangle$ denotes the initial (excited) state of the atom, $\delta(\omega_{\text{i}} - \omega_{\text{f}})$ is the Dirac delta function, and $\hat{H}_{\text{I}}$ is the Hamiltonian. In the considered case, $\hat{H}_{\text{I}}$ describes the electromagnetic interaction of an electric field $\boldsymbol{E}$ with an electric dipole moment $\boldsymbol{p}$ in the electric dipole approximation. $\hat{H}_{\text{I}}$ can thus be expressed as:

$$\hat{H}_{\text{I}} \quad = \quad -\hat{\boldsymbol{p}} \cdot \hat{\boldsymbol{E}} \,, \tag{2.21}$$

where $\hat{\boldsymbol{p}}$ and $\hat{\boldsymbol{E}}$ are the operators, describing the dipole moment and the electric field, respectively. Fermi's Golden Rule can therefore be written as [34]:

$$\gamma \;=\; \frac{\pi\omega}{3\hbar\epsilon_0}|\boldsymbol{p}|^2\rho_{\mathrm{p}}(\boldsymbol{r}_0,\omega_0)\,, \tag{2.22}$$

where $\boldsymbol{r}_0$ denotes the considered position. The local density of states ρ_{p} reads, in terms of the eigenmodes of the system [34]:

$$\rho_{\mathrm{p}}(\boldsymbol{r}_0,\omega_0) \;=\; 3\sum_k[\boldsymbol{u}_{\mathrm{p}}\cdot(\boldsymbol{n}_{\mathrm{k}}\boldsymbol{n}_{\mathrm{k}}^*)\cdot\boldsymbol{u}_{\mathrm{p}}]\delta(\omega_{\mathrm{k}}-\omega_0)\,, \tag{2.23}$$

where $\boldsymbol{u}_{\mathrm{p}}$ is the unit vector in the direction of the dipole moment, $\boldsymbol{n}_{\mathrm{k}}$ denotes the electromagnetic eigenmodes of the system that the two-level atom is placed in, and ω_{k} is the frequency of the eigenmodes. The eigenmodes of the system fulfill the orthogonality relation:

$$\int \boldsymbol{n}_{\mathrm{k}}(\boldsymbol{r},\omega_{\mathrm{k}})\cdot\boldsymbol{n}_{\mathrm{k}'}(\boldsymbol{r},\omega_{\mathrm{k}'})^*d^3\boldsymbol{r} \;=\; \delta_{\mathrm{kk}'}\,, \tag{2.24}$$

where the integration runs over the entire mode volume and $\delta_{\mathrm{kk}'}$ is the Kronecker delta. The eigenmodes must also fulfill the wave equation at the position $\boldsymbol{r}_0$:

$$\nabla\times\nabla\times\boldsymbol{n}_{\mathrm{k}}(\boldsymbol{r}_0,\omega_{\mathrm{k}}) - \frac{\omega_{\mathrm{k}}^2}{\mathrm{c}^2}\boldsymbol{n}_{\mathrm{k}}(\boldsymbol{r}_0,\omega_{\mathrm{k}}) \;=\; 0\,. \tag{2.25}$$

One can solve equation 2.25 with the use of the dyadic Green's function $\bar{\bar{G}}(\boldsymbol{r},\boldsymbol{r}',\omega)$, which is defined by:

$$\nabla\times\nabla\times\bar{\bar{G}}(\boldsymbol{r},\boldsymbol{r}',\omega) - \frac{\omega^2}{\mathrm{c}^2}\bar{\bar{G}}(\boldsymbol{r},\boldsymbol{r}',\omega) \;=\; \bar{\bar{I}}\delta(\boldsymbol{r}-\boldsymbol{r}')\,, \tag{2.26}$$

with $\bar{\bar{I}}$ being the unit dyad. Since the eigenmodes form a complete set of equations, the dyadic Green's function can be written as [34]:

$$\bar{\bar{G}}(\boldsymbol{r},\boldsymbol{r}',\omega) \;=\; \sum_k \mathrm{c}^2\frac{\boldsymbol{n}_{\mathrm{k}}^*(\boldsymbol{r}',\omega_{\mathrm{k}})\boldsymbol{n}_{\mathrm{k}}(\boldsymbol{r},\omega_{\mathrm{k}})}{\omega_{\mathrm{k}}^2-\omega^2}\,. \tag{2.27}$$

Applying the mathematical identity:

$$\lim_{\eta\to 0}\mathrm{Im}\left[\frac{1}{\omega_{\mathrm{k}}^2-(\omega+\imath\eta)^2}\right] \;=\; \frac{\pi}{2\omega_{\mathrm{k}}}\left[\delta(\omega-\omega_{\mathrm{k}})-\delta(\omega+\omega_{\mathrm{k}})\right]\,, \tag{2.28}$$

to the Green's function, leads to:

$$\mathrm{Im}\left[\bar{\bar{G}}(\boldsymbol{r},\boldsymbol{r}',\omega)\right] \;=\; \frac{\pi \mathrm{c}^2}{2\omega}\sum_{\mathrm{k}} \boldsymbol{n}_{\mathrm{k}}^*(\boldsymbol{r}',\omega_{\mathrm{k}})\boldsymbol{n}_{\mathrm{k}}(\boldsymbol{r},\omega_{\mathrm{k}})\delta(\omega - \omega_{\mathrm{k}})\,. \tag{2.29}$$

If this is inserted into formula 2.23, one can rewrite the LDOS in terms of the dyadic Green's function, resulting in:

$$\rho_{\mathrm{p}}(\boldsymbol{r}_0,\omega_0) \;=\; \frac{6\omega_0}{\pi \mathrm{c}^2}\left[\boldsymbol{u}_{\mathrm{p}}\cdot\mathrm{Im}\left[\bar{\bar{G}}(\boldsymbol{r}_0,\boldsymbol{r}_0,\omega_0)\right]\cdot\boldsymbol{u}_{\mathrm{p}}\right]\,, \tag{2.30}$$

In combination with equation 2.22, equation 2.30 allows for the calculation of the decay rate γ of a two-level system in an arbitrary environment. The only information needed is the dyadic Green's function. From a classical point of view one considers an excited atom, represented by a dipole, which generates an electric field. This electric field is influenced by its surrounding and acts back on the dipole (the excited atom). This in turn modifies the decay rate of the atom.

2.2.5 Fast moving electrons and plasmons

The main technique employed in this work is electron energy loss spectroscopy (EELS). EELS is performed in an electron microscope, where a fast moving electron interacts with the specimen and thereby loses some of its kinetic energy. The amount of energy that is lost can then be measured. A detailed description of the method can be found in section 3.3. For now, only the interaction taking place when a fast moving electron penetrates or pass by a metal nanoparticle and excites a plasmon is considered. The following derivation is based on the original work by R. Ritchie, published in 1957 [17] and a modified version from 2008 by García de Abajo et al. [50].

First of all, some assumptions are made to simplify the mathematical description of the plasmon excitation. (i) In the experiment the beam is focused onto the sample, to a spot with a diameter of a less than a nanometer. The investigated structures typically have sizes of a few hundred nanometers. Therefore one can model the electron using a Dirac delta function. (ii) A particular electron is allowed to interact with the sample only once (i.e., only single scattering processes are considered). (iii) At a given time, only one electron can interact with the sample. (iv) The kinetic energy of the incident fast moving electron is in the range of $100\,\mathrm{keV}$ and the expected energy loss is in the range of a few eV. This leads to a relative change of the kinetic energy of about 10^{-5}. Therefore one assumes that the electron is moving with a constant velocity.[1]
The principal idea of the following description is similar to section 2.2.3. A fast moving

---

[1]This assumption is only valid for the theoretical description of the excitation process. Later, when the detection of the energy loss is discussed, it is indeed the difference in the kinetic energies of the electrons that is measured.

electron is considered to induce an electric field ($\boldsymbol{E}_{\text{ind}}$) in the nanoparticle, this electric field then acts back on the electron, causing a loss of kinetic energy.

The force $\boldsymbol{F}$ acting on the electron is given by:

$$\boldsymbol{F} \;\; = \;\; -e\boldsymbol{E}_{\text{ind}}\,. \tag{2.31}$$

The magnetic force acting on the electrons is not taken into account, since it does not cause a change in the electron's kinetic energy. The work W of the electron in the induced electric field can then be derived by a path integral of the force along the electron path:

$$W \;\; = \;\; \int \boldsymbol{F}\, d\boldsymbol{r}\,. \tag{2.32}$$

With these two equations and the substitution $d\boldsymbol{r} = \frac{d\boldsymbol{r}}{dt}dt = \boldsymbol{v}dt$ one gets:

$$W \;\; = \;\; \int_{-\infty}^{\infty} -e\boldsymbol{v} \cdot \boldsymbol{E}_{\text{ind}}(\boldsymbol{r}_{\text{e}}, t)dt\,. \tag{2.33}$$

This equation states the average work that is performed by the electron moving along the electron trajectory $\boldsymbol{r}_{\text{e}}(t)$. If only a single scattering process is considered, where the energy $\hbar\omega$ is transferred from the fast moving electron to the plasmon excitation, one has to introduce the electron energy loss probability $\Gamma(\omega)$. The work of the electron can then be written as the integral of the electron energy loss probability over the frequency space, where each frequency is weighted by its energy $\hbar\omega$:

$$W \;\; = \;\; \int_{\omega=0}^{\infty} d\omega\hbar\omega\Gamma(\omega)\,. \tag{2.34}$$

For a better understanding of the electron energy loss probability $\Gamma(\omega)$, equation 2.33 is considered in relation to equation 2.34. Since the two equations are in time domain and frequency domain, respectively, a Fourier transformation of the induced electric field is performed, which leads to the expression:

$$\Gamma(\omega) = \frac{\text{e}}{\pi\hbar\omega} \int_{\text{t}=-\infty}^{\infty} dt\,\text{Re}\left[\text{e}^{-\imath\omega t}\boldsymbol{v} \cdot \boldsymbol{E}_{\text{ind}}\left(\boldsymbol{r}_{\text{e}}\left(t\right), \omega\right)\right]\,. \tag{2.35}$$

The induced electric field can now be expressed using the dyadic Green's function ($\bar{\bar{G}}(\boldsymbol{r}, \boldsymbol{r}', \omega)$) (see [34, 50]):

$$\boldsymbol{E}_{\text{ind}}(\boldsymbol{r}_{\text{e}}, \omega) \;\; = \;\; \imath\omega\mu_0 \int_V d^3r'\bar{\bar{G}}(\boldsymbol{r}, \boldsymbol{r}', \omega)\boldsymbol{j}\left(\boldsymbol{r}', \omega\right)\,, \tag{2.36}$$

which includes the current density $\boldsymbol{j}\left(\boldsymbol{r}, t\right)$, caused by the fast moving electron. The current density can be modeled via:

$$\boldsymbol{j}(\boldsymbol{r}, t) \;\; = \;\; \text{e}\boldsymbol{v}\delta[\boldsymbol{r} - \boldsymbol{r}_{\text{e}}(t)]\,. \tag{2.37}$$

If electrons that travel along the z-axis are considered, one obtains:

$$\boldsymbol{j}(\boldsymbol{R}, z, t) \;=\; ev\boldsymbol{u}_{\mathrm{z}}\delta(\boldsymbol{R} - \boldsymbol{R}_0)\delta(z - z(t)) \tag{2.38}$$

$$\;=\; e\boldsymbol{u}_{\mathrm{z}}\delta(\boldsymbol{R} - \boldsymbol{R}_0)\delta(z/v - t)\,, \tag{2.39}$$

with $\boldsymbol{u}_{\mathrm{z}}$ being the unit vector in the z-direction, $\boldsymbol{R}$ being the position vector in the plane perpendicular to z (i.e., $\boldsymbol{r} = (\boldsymbol{R}, z)$, with $\boldsymbol{R} = (x, y)$, and $\boldsymbol{R}_0$ being the position of the electron beam in the plane perpendicular to the z-axis). A Fourier transformation brings the current density into the frequency domain:

$$\boldsymbol{j}(\boldsymbol{r}, \omega) \;=\; \int dt\, \mathrm{e}^{\imath\omega t}e\boldsymbol{u}_{\mathrm{z}}\delta(\boldsymbol{R} - \boldsymbol{R}_0)\delta(z/v - t) \tag{2.40}$$

$$\;=\; \mathrm{e}^{\imath\omega z/v}e\boldsymbol{u}_{\mathrm{z}}\delta(\boldsymbol{R} - \boldsymbol{R}_0)\,. \tag{2.41}$$

With this current density one can now calculate the electron energy loss probability, by inserting 2.41 into 2.36 and then into 2.35:

$$\Gamma\left(\boldsymbol{R}_0, \omega\right) = \frac{\mathrm{e}^2\mu_0}{\pi\hbar} \int_{-\infty}^{\infty} \int_{-\infty}^{\infty} dt\,dt'\mathrm{Im}\left[\mathrm{e}^{-\imath\omega(t-t')}\boldsymbol{u}_{\mathrm{z}} \cdot \bar{\bar{G}}(\boldsymbol{R}_0, z(t), \boldsymbol{R}_0, z(t'), \omega)\boldsymbol{u}_{\mathrm{z}}\right]\,. \tag{2.42}$$

Performing a Fourier transform leads to:

$$\Gamma\left(\omega\right) = \frac{\mathrm{e}^2\mu_0}{\hbar}\mathrm{Im}\left[\boldsymbol{u}_{\mathrm{z}} \cdot \bar{\bar{G}}(\boldsymbol{R}_0, q, \boldsymbol{R}_0, -q, \omega)\boldsymbol{u}_{\mathrm{z}}\right]\,, \tag{2.43}$$

where $q = \omega/v$ denotes the wavenumber of the electron and $\bar{\bar{G}}(\boldsymbol{R}_0, q, \boldsymbol{R}_0, -q, \omega)$ is the partially Fourier transformed (with respect to z and z') dyadic Green's function. By inserting 2.30 into 2.43, one can make a connection between the electron energy loss probability and the projection of the LDOS along the electron trajectory:

$$\Gamma(\omega) = \pi\frac{\mathrm{e}^2}{6\hbar\epsilon_0\omega}\rho(\boldsymbol{R}_0, q, \omega)\,. \tag{2.44}$$

This direct connection between the energy loss probability and the local density of states (projected onto the electron beam trajectory) and hence the eigenmodes of the system was made in 2008 by García de Abajo. However, this interpretation was subsequently questioned by Hohenester et al. [51]. Based on numerical simulations, they concluded that the qualitative agreement between EELS and LDOS is often fairly good, but that there is no *direct* quantitative connection. The discrepancy between EELS and LDOS was mainly attributed to the fact that an electron cannot be described by a dipole. They also showed that EELS can even be blind to *plasmonic hot spots* in the gap region between coupled particles. The experimental approach to this controversy is discussed in chapter 7.

2.3 Metamaterials

Metamaterials are artificially designed materials that exhibit phenomena not found in natural materials. These phenomena can be traced back to their fundamental building blocks, so called meta-atoms, which are arranged on a lattice. The size of the meta-atoms is small compared to the wavelength of the considered electromagnetic wave, and therefore, one can describe the material properties using effective material parameters (especially the permittivity and permeability). By changing the shape of a meta-atom one can tailor the effect of each meta-atom and thus fabricate materials with adjustable properties.

There are meta-atoms that can be used as magnetic dipoles, oscillating at optical frequencies (there are no natural materials that show this behavior at optical frequencies) and lead to a negative permeability μ. In combination with a negative permittivity ϵ one obtains a material with a negative index of refraction ($n = -\sqrt{\epsilon\mu} < 0$), as was predicted by Veselago many years ago [52]. In such a medium light is refracted in the opposite direction compared to classical media and the Poynting vector is anti-parallel to the wave vector. A negative index material can for example be employed for perfect lensing [52, 53]. In principle a slab with a negative refractive index is sufficient to create a lens without a resolution limit; even sub-wavelength objects can be imaged. Before an example of meta-atoms is discussed, which is responsible for negative permeability, it is shortly explained how to achieve a negative permittivity. Usually, this is done by diluting a metal: The permittivity for a Drude metal is given by equation 2.12, where only the plasma frequency $\omega_{\mathrm{pl}} = \sqrt{\frac{ne^2}{\epsilon_0 m_e}}$ depends on the material properties. The electron density n can be changed by diluting the metal, i.e., introducing some dielectric defects to the metal. Typically this is done by producing cylinders of metal in air [54, 55]. This shifts the effective plasma frequency to smaller frequencies, and thus enables a negative permittivity. The meta-atoms, which show a negative permeability will be discussed in detail in the next section.

2.3.1 The split-ring resonator

The split-ring resonator (SRR) [56, 57] is the most prominent example of a magnetic photonic meta-atom. It was first designed to change the permeability at elevated frequencies. In 2001 it was shown that the SRR, in combination with a diluted metal, shows negative refraction at frequencies of about $10\,\mathrm{GHz}$ (wavelength of $3\,\mathrm{cm}$) [55]. For these frequencies, the structures can be easily fabricated on electronic circuit boards. However, for higher frequencies the SRR needs to be significantly smaller, as will be seen in the following. In 2004 a negative permeability was reported for 100 THz ($3\,\mu\mathrm{m}$) [1].

A SRR is a metallic ring, which features a small slit. When a light wave hits this structure a charge separation is induced (according to section 2.1.2), which leads to a current along the ring. This ring current induces a magnetic dipole moment, which is normal to the

plane of the SRR (see fig. 2.3 (a)). This magnetic dipole moment in turn behaves similarly to a Lorentz oscillator and can lead to a negative permeability. To tune the resonance frequency of the SRR one can change e.g., the geometry or the constituent materials. Before the SRR is discussed from the plasmonic point of view, one can consider a more intuitive way of understanding the SRR with the analogy of a *RLC*-circuit:
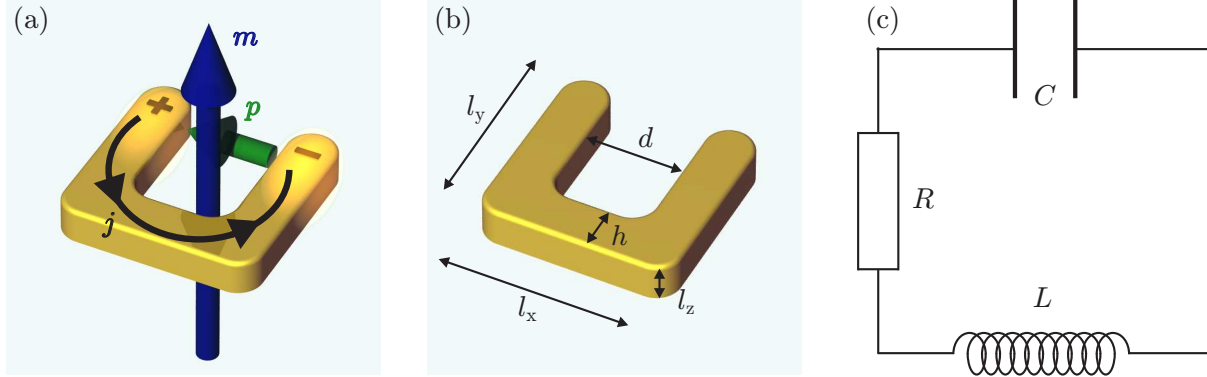

Figure 2.3: The split-ring resonator: (a) Sketch of a charge separation (indicated by the + and − sign) causing a ring current j, which results in a magnetic dipole moment m (blue arrow). The electric dipole moment p is indicated by the green arrow. (b) Dimensions of the SRR, and (c) the equivalent *RLC*-circuit.

A SRR excited by an external electric field can be described by a driven *RLC*-circuit. In this simplified picture, the ring of the SRR is represented by a coil (only one loop) with an inductance L. The gap (the split) is represented by a capacitor with a capacitance C (see figure 2.3). The resonance frequency of the *RLC*-circuit is then given by (see appendix 9.1):

$$\omega_{\mathrm{LC}} \;=\; \frac{c_0}{\sqrt{\epsilon l_x l_y}} \sqrt{\frac{d}{l_y - h}} \propto \frac{1}{\mathrm{size}}, \tag{2.45}$$

with the dimensions of the SRR given in figure 2.3. Equation 2.45 states that the resonance frequency is inversely proportional to the linear dimension of the SRR. Decreasing the size of the SRR leads to an increase of the resonance frequency. As will be seen later, this holds only for frequencies well below the plasma frequency [58–60]. In the quasi-static regime, the resonance frequency is independent of the particle size, as can be seen in equation 2.17. For a detailed view of the analogy of a SRR and a *RLC*-circuit, please see appendix 9.1.

2.3.2   The split-ring resonator in plasmonics

To understand the eigenmodes of the SRR, the eigenmodes of straight antennas can be considered, which have been known for many years and can be deduced from classical electrodynamics [28]. The plasmonic eigenmodes of a (nano-) antenna can be found by considering the well-known radio antennas, scaled with some geometry parameters [61]. The first-order mode (see fig. 2.4 (a)) of a straight antenna shows two opposite charge densities at the two ends of the antenna, resulting in an oscillation of the charges from one end to the other (this is the dipole mode, discussed in section 2.2.2).

From the straight antenna it is only a small step to understand the plasmonic resonances of a SRR. Therefore, the two outer parts of the antenna are bent upwards. The first-order plasmonic mode has the same quantitative form, i.e., the maxima of the charge density
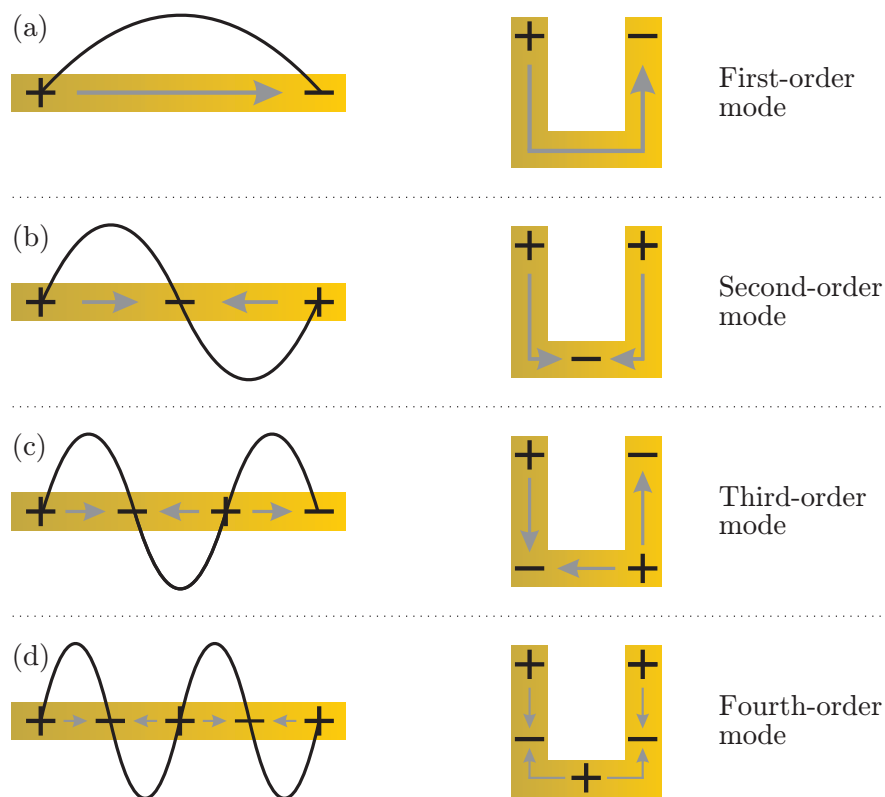

Figure 2.4: Plasmonic modes of an antenna (left) and a split ring resonator (right). The grey arrows indicate the direction of the current; the black curves indicate the current density distribution. The well-known mode distributions of a straight antenna can be adopted for the SRR: By bending the ends of the antenna upwards, one gets the mode distribution of the SRR. From (a) to (d), the number of maxima of the charge densities (indicated by + or −) increases linearly. Note that this is only an illustration of the currents and charge densities. According to section 2.2.2, a time-dependent oscillation is considered.

oscillation are at the two outer arms of the SRR, resulting in a ring current (which induces the magnetic dipole). The electric dipole moment is oriented parallel to the bottom wire (see fig. 2.3 (a)).

The second-order mode (see fig. 2.4 (b)) shows three maxima of the charge density oscillation in the antenna, as well as in the SRR. For the antenna, the effective electric dipole moment of this mode is significantly smaller than that of the first-order mode, and therefore the excitation with optical waves is suppressed. For the SRR, the effective electric dipole is perpendicular to the bottom wire (parallel to the arms).

The current density distribution of the m-th plasmonic mode is a standing wave with nodes at the ends and m nodes distributed along the SRR. The locations of the current density nodes coincide with the antinodes of the charge density oscillation. Two higher-order plasmonic modes can be found in fig. 2.4 (c-d).

2.4   Generalized Babinet's principle

In classical optics, Babinet's principle states that the diffraction patterns of two complementary apertures are identical (except for the total forward beam intensity), for example in the case of a slit and a wire of the same width [62]. This principle was extended to metamaterials in the last decade: According to the generalized Babinet's principle [63–65], the modes of a metal particle and those of the corresponding complementary metallic screen[2] are closely connected. Both structures exhibit modes with the same resonance energies but complementary mode profiles. They are related to each other by interchanging the E-field and B-field distributions. This was shown by Zentgraf et al., who recorded optical spectra of a SRR and the complementary structure (the C-SRR). They showed that for the C-SRR, illuminated by a complementary wave (polarization rotated by 90°), the transmittance and reflectance spectra can be interchanged [64].

How can Babinet's principle be of use in electron energy loss spectroscopy? Previously, it was shown that the first resonance of the SRR induces a magnetic field in the center of the ring. As mentioned in section 2.2.5, magnetic fields do not cause an energy loss and therefore cannot be detected with EELS. Thus, the magnetic field of a SRR cannot be measured. However, by investigating the complementary SRR (C-SRR) with EELS, its electric field information can be obtained and Babinet's principle states that from this electric field one can deduce the magnetic field of a SRR. In fig. 2.5 simulations of the electric and magnetic fields of a SRR and a C-SRR are depicted [66].

The $|E_z|$ field distribution of the first mode of the SRR has two pronounced maxima at the ends of the arms (fig. 2.5 (b)). They stem from the two charge densities, described in the previous section. The corresponding $|B_z|$ field distribution (fig. 2.5 (c)) is the result of the circulating ring current, which induces a strong magnetic field in the center of the SRR. When the two mode profiles are compared to the mode profiles of the C-SRR

---

[2]The complementary screen of e.g., a gold disc is a gold film, with a circular hole of the discs diameter.
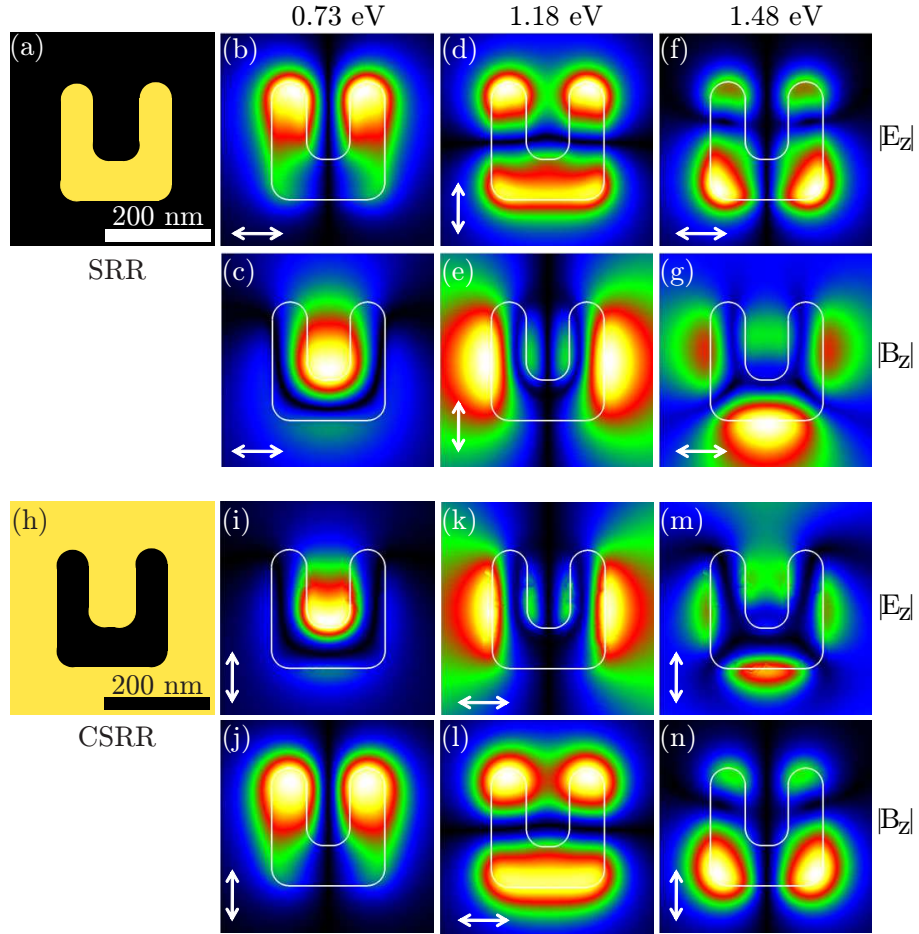
Figure 2.5: Simulated field distributions of $|E_z|$ and $|B_z|$ for the first three modes of a SRR and the corresponding C-SRR. The fields are recorded in a plane 20 nm above the structures. Each field plot has an independent color scale in which small field strengths are represented by dark blue and large fields correspond to yellow. Note that the exciting optical fields for SRR and C-SRR are in each case polarized orthogonally (see white arrows). The scale bars are 200 nm [66].

(fig. 2.5 (i,j)), one finds the confirmation of Babinet's principle: The electric field of the SRR (b) equals the magnetic field of the C-SRR (j) and the magnetic field of the SRR (c) equals the electric field of the C-SRR (i). The second mode of the SRR exhibits three maxima in the $|E_z|$ field distribution (fig. 2.5 (d)). The resulting currents in the left and right arm of the SRR are oscillating in phase (see fig. 2.4). The magnetic fields produced by these currents interfere destructively in the center of the SRR and constructively outside of the SRR (e). As expected, the second mode of the C-SRR exhibits a small $|E_z|$ component in the center part of the metallic screen and a strong $|E_z|$ component on the metal on the left and right side of the SRR-shaped aperture (k). The third mode exhibits four maxima in the $|E_z|$ field distribution (fig. 2.5 (f)). With analogous considerations, the corresponding magnetic field distribution can be found (g). A comparison with the

C-SRR mode profiles also confirms Babinet's principle.

2.5   Coupled plasmonic systems

In the case of two or more nanoparticles in the vicinity of each other, the electric fields of the plasmons overlap and an electromagnetic interaction between the plasmons arises. To describe this near field coupling, the first-order plasmon oscillation in each particle can be approximated by a simple Lorentz oscillation. Next, two antennas are considered with the dipole moments $P_{1/2} = eX_{1/2}$, with e the electron charge and $X_{1/2}$ the displacement amplitude of dipole 1 or 2. To derive the eigenfrequency of the coupled system, each antenna is described by the equation of motion of a damped Lorentz oscillator with an additional interaction term (W):

$$\ddot{\boldsymbol{x}}_1 + \gamma_{\mathrm{D}}\dot{\boldsymbol{x}}_1 + \tilde{\omega}_0^2 \boldsymbol{x}_1 + W(\boldsymbol{x}_1 - \boldsymbol{x}_2) = 0 \,, \tag{2.46}$$

$$\ddot{\boldsymbol{x}}_2 + \gamma_{\mathrm{D}}\dot{\boldsymbol{x}}_2 + \tilde{\omega}_0^2 \boldsymbol{x}_2 - W(\boldsymbol{x}_1 - \boldsymbol{x}_2) = 0 \,, \tag{2.47}$$

where $\tilde{\omega}_0$ is the resonance frequency of a single undriven antenna. Now, two identical antennas with a positive coupling constant $W = +\,|W|$ are considered and the already familiar ansatz 2.1.2 $\boldsymbol{T}(t) = \boldsymbol{X}_0 e^{-\imath\omega t}$ is used:

$$(-\omega^2 - \imath\gamma\omega + \tilde{\omega}_0^2 + W)\boldsymbol{X}_{0,1} - W\boldsymbol{X}_{0,2} = 0 \,, \tag{2.48}$$

$$-W\boldsymbol{X}_{0,1} + (-\omega^2 - \imath\gamma\omega + \tilde{\omega}_0^2 + W)\boldsymbol{X}_{0,2} = 0 \,. \tag{2.49}$$

Solving this set of equations leads to the two eigenfrequencies:

$$\omega_L = \sqrt{\tilde{\omega}_0^2 - \frac{1}{2}\gamma^2} - \frac{\imath}{2}\gamma \,, \tag{2.50}$$

$$\omega_H = \sqrt{\tilde{\omega}_0^2 - \frac{1}{2}\gamma^2 + 2\,|W|} - \frac{\imath}{2}\gamma \,. \tag{2.51}$$

Comparing ω_L and ω_H reveals that ω_H has the additional term $+2\,|W|$, and therefore $\omega_H \geq \omega_L$ (H = high; L = low). With 2.48 one finds the following relations between the two dipole amplitudes $\boldsymbol{X}_{0,1}$ and $\boldsymbol{X}_{0,2}$:

$$\text{for } \omega_L : \quad \frac{\boldsymbol{X}_{0,1}}{\boldsymbol{X}_{0,2}} = +1 \,, \tag{2.52}$$

$$\text{for } \omega_H : \quad \frac{\boldsymbol{X}_{0,1}}{\boldsymbol{X}_{0,2}} = -1 \,. \tag{2.53}$$

This shows that for a positive coupling constant there exists a low-frequency mode, where the two dipoles point in the same direction (the oscillation is symmetric) and a high

frequency mode, where the two dipoles are antiparallel (the oscillation is antisymmetric). The two modes are denoted by their relative oscillation amplitude: $(++)$ for the symmetric mode and $(+-)$ for the antisymmetric mode. A negative coupling constant $(W = -|W|)$ leads to:

$$\omega_H \;=\; \sqrt{\tilde{\omega}_0^2 - \frac{1}{2}\gamma^2} - \frac{\imath}{2}\gamma\,, \tag{2.54}$$

$$\omega_L \;=\; \sqrt{\tilde{\omega}_0^2 - \frac{1}{2}\gamma^2 - 2\,|W|} - \frac{\imath}{2}\gamma\,. \tag{2.55}$$

The comparison shows that the additional term reads: $-2\,|W|$, leading to the ratios of the two dipole amplitudes:

$$\text{for } \omega_L: \quad \frac{\boldsymbol{X}_{0,1}}{\boldsymbol{X}_{0,2}} \;=\; -1\,, \tag{2.56}$$

$$\text{for } \omega_H: \quad \frac{\boldsymbol{X}_{0,1}}{\boldsymbol{X}_{0,2}} \;=\; +1\,. \tag{2.57}$$

In case of a negative coupling constant, one thus obtains an antisymmetric low-frequency mode and a symmetric high frequency mode.

In the simple picture of two coupled antennas (with the dipole axes of the antennas pointing in x-direction), this can be connected to two cases of coupling. (i) For a negative coupling constant the antennas are displaced in y-direction (center of fig. 2.6) and (ii) for a positive coupling constant the antennas are displaced in x-direction (right hand side of fig. 2.6).
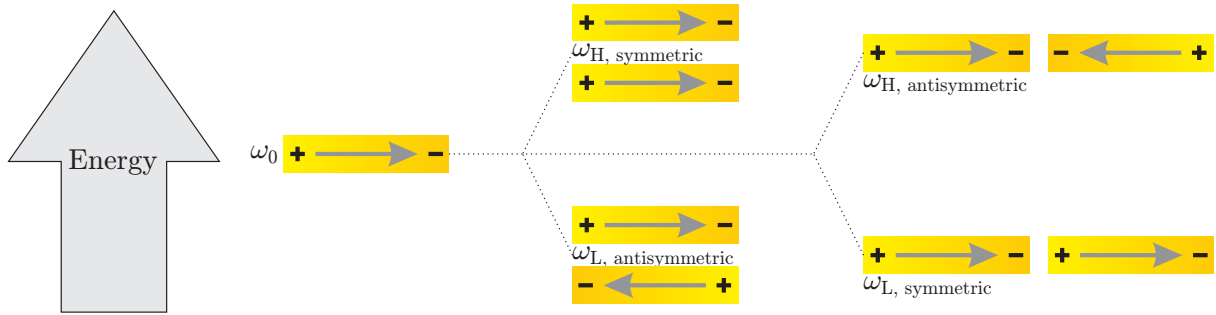

Figure 2.6: Coupling of two antennas. When a single antenna with the resonance frequency ω_0 interacts with a second antenna, two modes arise. In case of transversal coupling (center) the high energy mode is symmetric and the low energy mode is anti-symmetric. In case of longitudinal coupling (right hand side) the high energy mode is anti-symmetric and the low energy mode is symmetric.

In both cases, the antisymmetric mode exhibits a vanishing effective dipole moment. Therefore, the excitation of this mode with an electromagnetic wave is strongly suppressed. Hence, the antisymmetric mode is also called **optical dark mode**, in contrast

to the symmetric mode, which is called **optical bright mode**. For the excitation of plasmons with fast moving electrons the effective dipole moment does not play a role, as both modes are excitable by electrons.

Four coupled antennas

The assumptions applied to two interacting Lorentz oscillators in equation 2.47 can be easily expanded to four interacting Lorentz oscillators. First, the interactions beyond the nearest neighbor are neglected and the coupling of neighboring antennas is described by the interaction term W. The behavior of a single antenna is still described by the damped Lorentz oscillator (eq. 2.47), which from now on is represented by A. The interactions can then be written as:

$$\begin{pmatrix} A & W & 0 & 0 \\ W & A & W & 0 \\ 0 & W & A & W \\ 0 & 0 & W & A \end{pmatrix} \begin{pmatrix} x_1 \\ x_2 \\ x_3 \\ x_4 \end{pmatrix} = 0 \tag{2.58}$$

This problem can be solved analytically and yields the eigenvalues:

$$A - \frac{\sqrt{5}+1}{2}W, \quad A - \frac{\sqrt{5}-1}{2}W, \quad A + \frac{\sqrt{5}-1}{2}W, \quad A + \frac{\sqrt{5}+1}{2}W. \tag{2.59}$$

The approximate corresponding eigenvectors are:

$$\begin{pmatrix} 1 \\ 1.61 \\ 1.61 \\ 1 \end{pmatrix}, \begin{pmatrix} -1 \\ -0.61 \\ 0.61 \\ 1 \end{pmatrix}, \begin{pmatrix} 1 \\ -0.61 \\ -0.61 \\ 1 \end{pmatrix}, \begin{pmatrix} -1 \\ 1.61 \\ -1.61 \\ 1 \end{pmatrix}. \tag{2.60}$$

These four eigenvectors represent the four different eigenmodes of a coupled system with four antennas. With the assumptions made above, one cannot make a quantitative analysis of the appearance of the four vectors, though the signs of the vector-components helps with interpreting the orientation of the individual electric dipole moments. They are $(++++)$, $(--++)$, $(+--+)$, and $(-+-+)$. The first mode $(++++)$ corresponds to the case where all dipoles point in the same direction. The effective dipolmoment is thus different from zero and the mode can be excited by an optical wave (optical bright mode). On the other hand, the second mode $(--++)$ shows an electric dipolmoment which is zero and is thus an optical dark mode[3]. For clarity only nearest neighbor coupling was assumed in equation 2.59, though by considering coupling effects between each antenna, eigenvectors with the same signs but different values would be found. The exact values are not trivial to determine, but in principle represent the energies of the different modes.

---

[3]Optical dark modes cannot be excited by optical plane waves, but this has no influence on the excitation with electrons, as discussed in section 2.5.

The previous example of four interacting antennas can also be performed for tens or hundreds of dipoles, with the result that the number of interacting antennas equals the number of (different) modes, i.e., in the case of 10 antennas, one expects 10 modes. For a complete metamaterial, with in principle an infinite number of meta-atoms, the modes will overlap and form a quasi-continuum, in analogy to band formation in solid state physics.

In 2003 the group of Peter Nordlander described the interaction of plasmons in the plasmon picture, without the simplification of dipoles [67, 68]. They showed that the plasmons of two spherical nanoparticles hybridize to a bonding (symmetric) and anti-bonding (anti-symmetric) mode, at different energies. Their hybridization-model provides a more concrete understanding of the energies and the extinction cross-sections of the plasmons in nanosphere dimers. In their simulations they also investigated the influence of the distance between the two nanoparticles on the hybridization *strength* and found a decrease with increasing distances.

Chapter 3

Methods

In this chapter, the employed experimental and numerical techniques and methods are described. First, the fabrication of nanostructures on electron transparent membranes is presented. The main part of this chapter focusses on the transmission electron microscope (TEM) used in this work and the components which distinguish this microscope from standard TEMs. An optical setup to record extinction spectra of single nanoparticles is introduced as well as a numerical simulation method, based on the discontinuous Galerkin time-domain approach.

3.1   Electron beam lithography

The structure size of a plasmonic particle is usually in the order of tens or hundreds of nanometers. One method to fabricate structures on this scale is chemical synthesis [12, 20–22]. Unfortunately this method is very limited in the control over size, shape, and relative orientation of the produced metallic nanoparticles. Electron beam lithography (EBL) overcomes these limitations. It allows for the design and the very precise positioning of -in principle- arbitrary two-dimensional structures on a substrate. Over the past years, it has become a standard tool in plasmonics, even for the fabrication of multilayer structures [69]. For transmission electron microscopy (TEM), the structures have to be placed on electron transparent substrates. Therefore, 30 nm thin silicon nitride (Si_3N_4)-membranes are utilized, which are mounted on a 0.2 mm thick octagonal silicon frame with a maximum corner-to-corner distance of 3.05 mm (to fit into a TEM sample holder), see fig. 3.1. For the presented experiments, the size of the membrane varied between $100 \times 100\,\mu m^2$ and $250 \times 250\,\mu m^2$.
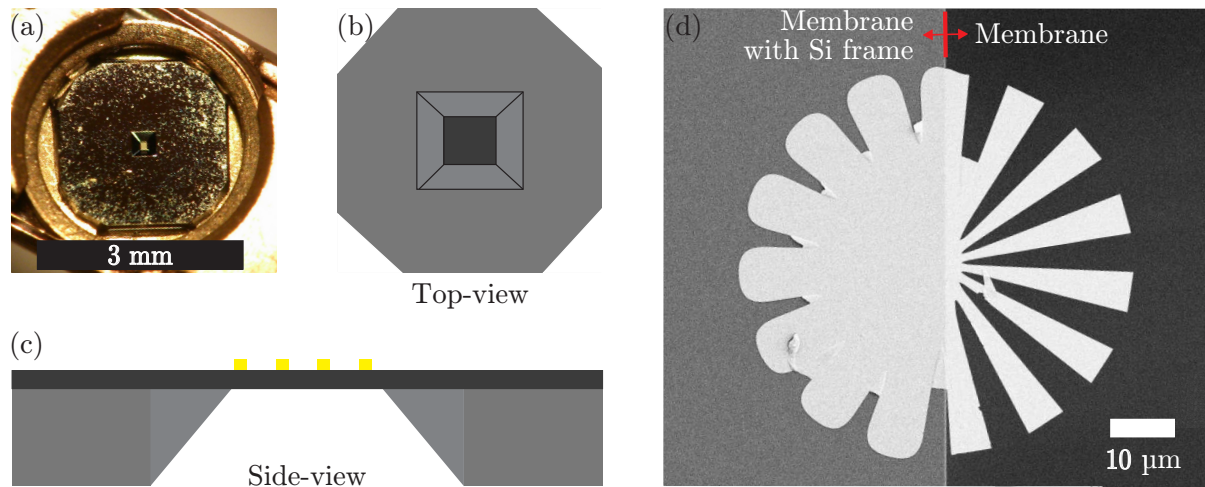
Figure 3.1: (a) Image of a Si$_3$N$_4$-membrane in a TEM holder. (b, c) Schematic view of the sample from the top and the side, respectively. (d) SEM image of a Siemens-star, which is partly on the bare membrane and partly on the membrane with a silicon frame beneath it. Siemens-stars can be used to determine the resolution of an optical system.

Sample processing

The standard EBL procedure is illustrated in fig. 3.2. The first step (see fig. 3.2 (a)) is the spin-coating of a positive resist onto the membranes. For this purpose, TEM membranes were purchased in an array of 4×4 frames from Silson[1] and were spin-coated either individually or in the whole array. For the spin coating[2], $45\,\mu$L poly(methyl methacrylate) (PMMA) dissolved in anisole[3] was used and the procedure was performed in two steps: (i) 5 seconds at 500 rpm to disperse the resist and then accelerate within 1 second to (ii) 4000 rpm for 90 seconds. The result is an approximately 200 nm thick layer of PMMA. The absolute thickness is not important; the reproducibility of the thickness on the other hand is very important, since it determines the electron dose. The sample was then baked in a convection oven at 175 °C for 1 hour to remove the remaining solvent. Samples spin-coated in the whole array showed a higher reproducibility in the layer thicknesses. The 16 silicon frames were isolated with tweezers after the baking process.

In the second fabrication step (see fig. 3.2 (b)), the sample is exposed to an electron beam in a scanning electron microscope (SEM)[4]. The beam is controlled by a lithography system[5], and illuminates only pre-defined regions of the PMMA resist. The electrons cause a structural change in the PMMA. The actual writing process is a standard

---

[1]Silson Ltd., United Kingdom
[2]Model WS-650MZ-23NPP/LITE, Laurell
[3]PMMA 950K A4
[4]Carl Zeiss NTS GmbH, Germany
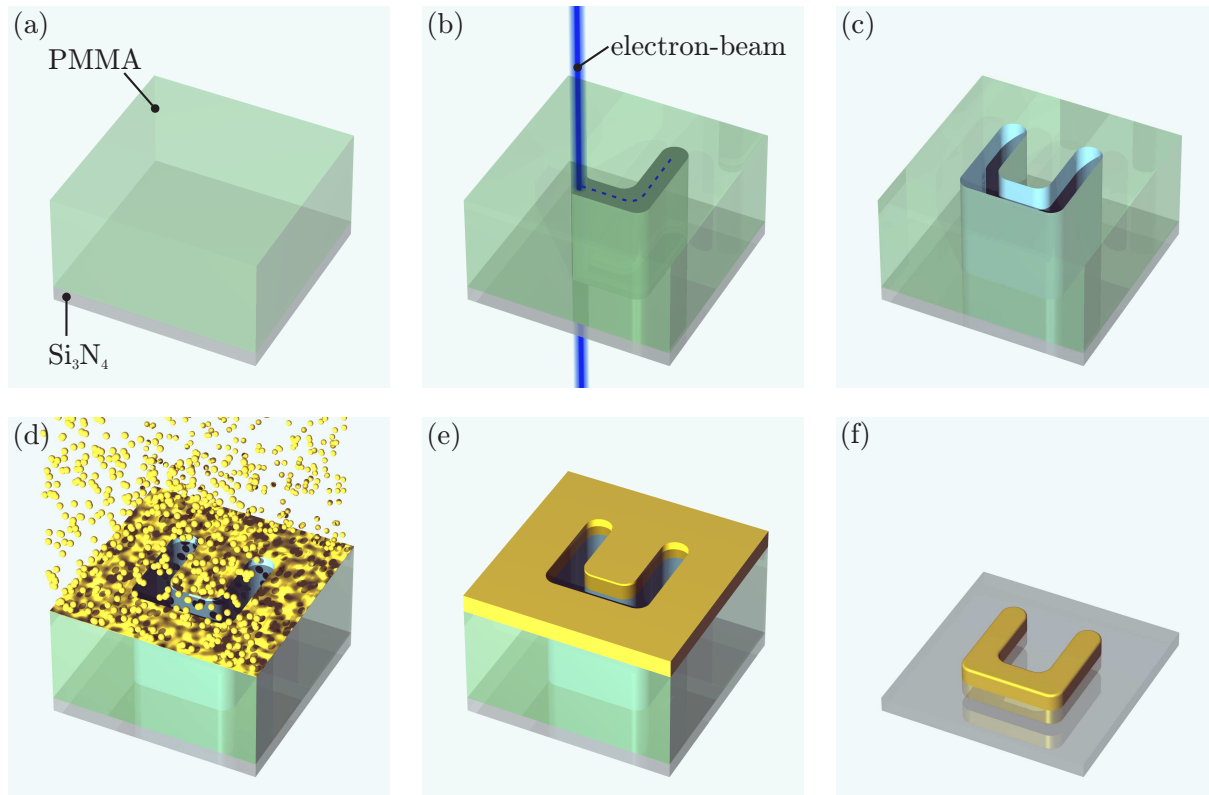[5]Raith e_Line, Raith GmbH, Germany

Figure 3.2: A schematic view of the electron beam lithography process, starting with the spin coating of a 200 nm thin layer of PMMA (a), followed by (b) the electron beam exposition to certain areas, which then can be removed by a developer (c). In a resistive evaporator, chromium (2 nm) and gold ($25 - 35$ nm) are evaporated (d, e); the lift-off process removes the remaining PMMA (f).

procedure, which will not be explained here (please see [49, 70]). The chosen aperture size of the microscope was 10 µm, the working distance was 8 mm and the acceleration voltage was 20 kV. This resulted in a current on the order of 35 pA.

Using Si_3N_4-membranes leads to some peculiarities that one has to account for:

- Si_3N_4-membranes exhibit sufficient conductivity for EBL; the usual ITO (indium tin oxide) layer as used on glass substrates is not needed.

- Every scan of the electron beam over the PMMA contributes to structural changes in the PMMA. Therefore, great care has to be taken when searching the membranes in the SEM. Since the membrane is always located in the center of the silicon frame, one knows the distance to the frame boundaries (depending on the size of the membrane) and therefore can approach the membrane without scanning the whole membrane.

- The proximity effect[6] is less present on the thin membranes (compared to thick glass substrates) and thus a higher dose is needed for the EBL process (compared to EBL on 'normal' substrates), as can be seen in fig. 3.1 (d).

Figure 3.1 (d) shows an image of a Siemens-star, fabricated half on the bare membrane and half on the membrane with the silicon frame beneath it. The exposed areas have the same dose; the less defined structures on the frame result from the proximity effect.

Post processing
The illuminated PMMA areas are dissolved by a developer, consisting of 3/4 isopropanol and 1/4 Methyl isobutyl ketone (MIBK), with additional 1.5 vol% butanone. For this purpose, the sample is dipped into the 8 °C cold developer for 45 sec and is subsequently blown dry with nitrogen. The resulting PMMA layer shows recesses at the areas previously defined by the electron beam (fig. 3.2 (c)).
In the next step (fig. 3.2 (d)) layers of chromium and gold are deposited onto the sample. A resistive evaporator[7] was used at 10^{-6} mbar with an evaporation rate of 0.1 nm/s for chromium and 0.2 nm/s for gold. The chromium layer has only a thickness of 2 nm and serves as an adhesion layer[8]. The thickness of the gold layer varies between 25 nm and 35 nm.
In the final lift-off procedure, the remaining PMMA (and the gold layer on top of it) is removed: The sample is placed in a 60 °C hot N-Methyl-2-Pyrrolidone (NMP) bath for $2 - 3$ hours[9] and is subsequently rinsed with NMP, acetone and ethanol. Great care has to be taken during the washing procedure due to the fragile membrane: The jet of the chemicals must to be almost parallel to the membrane. To remove chemical residues, the sample is washed with distilled water and blown dry with nitrogen.

The highest reproducibility of the structures was achieved, when the electron beam was scanned (in line mode) twice over the desired structure. This was achieved by duplicating the elements in the writing software and shifting them by 5 nm into the x- and y-direction. The nominal dose was $400\,\mu\text{C/cm}^2$ and each element had a dose factor of 5-8 (depending on the desired final width) and an additional *internal dose factor* of 2. Thus, the total dose was between 4000 and $6400\,\mu\text{C/cm}^2$. The step size was set to 1.6 nm.

3.2 Transmission electron microscopy

In conventional optical microscopy, the resolution is limited by the wavelength of visible light to about 200 nm. In transmission electron microscopes (TEM), where fast electrons

---

[6]The proximity effect: Primary electrons generate secondary electrons in the PMMA as well as in the substrate, which contribute to the exposure [71]. By this multiple scattering, the electron beam "blurs".
[7]Oerlikon Leybold Vacuum GmbH, Germany
[8]At these thicknesses the chromium layer is not continuous but forms small droplets. Samples were also produced without the adhesion layer, though, they show a lower reproducibility.
[9]A magnetic stirrer was not used, due to the fragile membrane

with energies in the range of 200 keV are used, the de Broglie wavelength of the electrons is on the order of 2.5 pm. The resolution limit by Abbe therefore predicts a resolution of $\sim$ 32 pm, which is a theoretical value that can never be achieved due to aberrations of the electron lenses. While lenses in optical microscopes are made of glass, electrons in a TEM are focused or deflected by electric and magnetic fields. Due to inhomogeneities in the fields, the electromagnetic lenses show similar aberrations as lenses made out of glass. Some of them can be compensated by stigmators or aberration correctors, while others cannot. A conventional TEM (without aberration correctors), operated at 100 kV has a resolution on the order of 0.25 nm, while high-end microscopes can resolve down to 0.05 nm [72]. For a general introduction to TEM, please see [73].

3.2.1   The Libra 200 (scanning) transmission electron microscope

In the following the general setup of the Libra 200 MC C_s-STEM[10] will be discussed. In particular the *monochromator*, the C_s-*Corrector*, and the Ω-*type energy filter* are essential for the project and will thus be described in more detail. The Libra 200 MC C_s STEM is a scanning transmission electron microscope (STEM), optimized for imaging in scanning mode. For this work, two Libra 200 microscopes were used, one located at caesar[11], called CRISP[12] and the other located at Harvard University[13]. The principle construction of the two microscopes is identical, though the latter one was built a few years after CRISP and has a more convenient and stable system. This is especially valid for the electron source (a Schottky type field emission gun (FEG)), which can be operated at 200 kV or 80 kV. Experiments which were performed at caesar were only possible at 200 kV, while the microscope at Harvard allowed for switching between the two acceleration voltages within days. The following principle setup is identical for both microscopes and can be seen in fig. 3.3.

In the FEG, the electrons are extracted from a tungsten tip with a voltage of 4.1 kV. Then they pass the gun-lens and are collimated into the monochromator (see section 3.2.2). The monochromator enhances the energy resolution from 0.7 eV to 0.15 eV for 200 kV acceleration voltage and to 0.09 eV for 80 kV acceleration voltage. The energy resolution of the microscope is defined by the FWHM (Full Width at Half Maximum) of the energy spread of the beam, after it has passed all electro optical elements. After the electrons have passed the monochromator, they are accelerated to their final energy of 200 keV/80 keV.

The FEG is followed by three condenser lenses and the C_s-Corrector. The C_s-Corrector is designed to fully correct second order aberrations of the illumination system. It can be adjusted using an automated software alignment procedure and is employed to increase

---

[10]Carl Zeiss NTS GmbH, Germany

[11]Research center caesar - center of advanced european studies and research, Bonn, Germany

[12]CRISP = corrected illumination scanning probe

[13]Harvard School of Engineering and Applied Science (SEAS), Cambridge, Massachusetts, United States
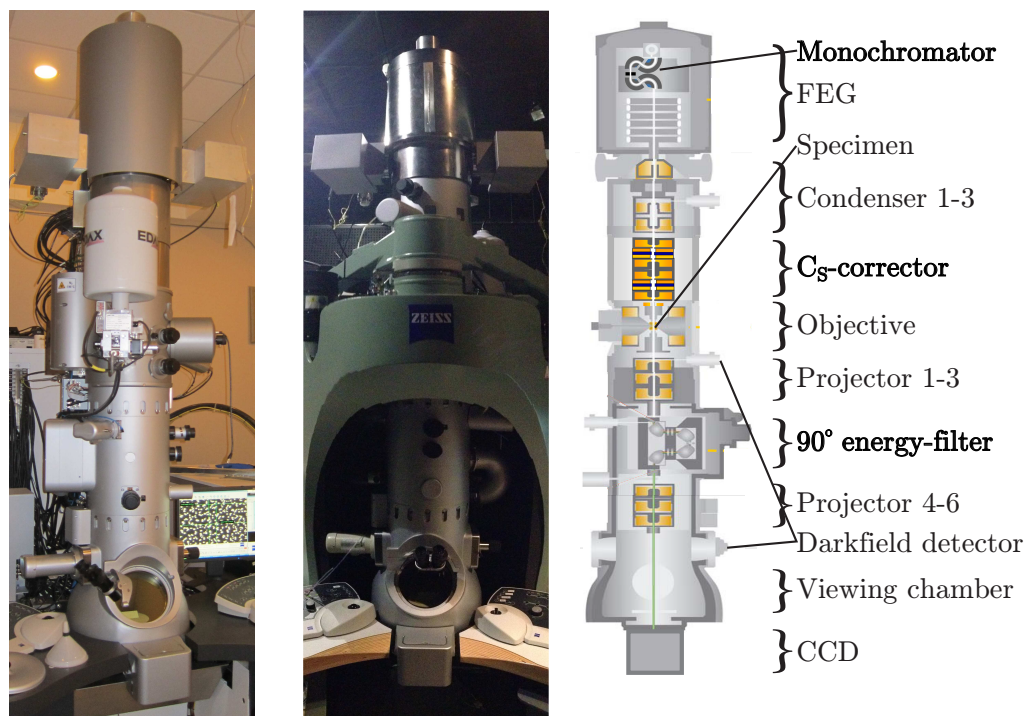
Figure 3.3: The two images show the TEMs utilized for this work. Both of them are Libra 200 MC C_s-STEM, one located at Harvard university (left) and the other located at caesar (right). The only apparent difference is the solid metal frame, which was designed to enhance the stability and decrease mechanical vibrations. The sketch on the right hand side shows the interior of the two microscopes, adapted from [74].

the beam current and the spatial resolution (see section 3.2.3). The C_s-Corrector is followed by the scan generator and the objective. While in TEM mode, the whole sample is illuminated at once. In scanning TEM (STEM), the electron beam is focused down to a subnanometer spot and is raster scanned over the sample. The signal is collected in a serial acquisition mode, either in bright field mode or in dark field mode. Dark field images are acquired with high angle annular dark field (HAADF) detectors. One HAADF detector is positioned right below the objective and the other one further below, just before the viewing chamber. After the electrons have passed the objective and the specimen, the electron beam is magnified by the first three projector lenses, which are followed by an in-column Ω-type energy-filter. In normal imaging mode, the filter acts as an additional lens, while in spectroscopy mode, the filter acts as an energy dispersive element (see section 3.2.4).

Before the beam reaches the viewing chamber, it passes through the last three lenses of the projector system. Inside the viewing chamber a fluorescence screen converts the electrons directly into a visible signal, which can be viewed in situ with binoculars. Alternatively, the viewing screen can be lifted and the electrons are detected with a CCD camera[14]. The

---

[14] 2k × 2k slow scan CCD camera (Gatan, Ultrascan 1000), the pixel size is $14\,\mu m^2$.

microscope is operated with the WinTEM and DigitalMicrograph (DM)[15] software.

3.2.2 Monochromator

To reduce the chromatic aberration (and thus increase the spatial resolution) and to enhance the energy resolution of the microscope, the employed TEM is equipped with a monochromator. In the monochromator, electrons pass through an electric field (up to 1000 V) and are dispersed according to their energy. A mechanical slit then uses the spatial distribution of electrons to blank out those electrons with energies that are not desired. There are a few different designs for monochromators. Here only the Ω-type monochromator[16] used in the Libra 200 will be described.
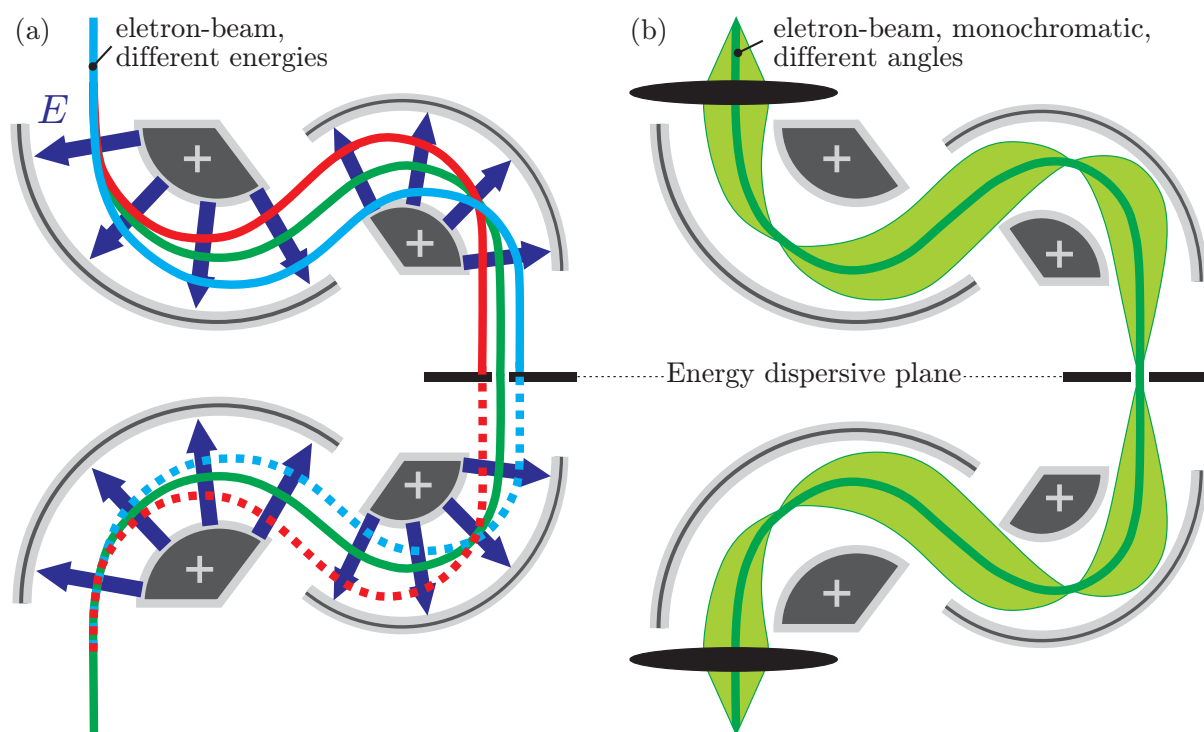
Figure 3.4: Schematic view of the monochromator integrated in the Libra 200. (a) Shows the behavior of electrons with different energies: The electron beam passes an electric field and is dispersed. (b) Shows the behavior of electrons of the same energy, but different inclination angles; an image of the virtual source is formed in the symmetry plane. Thus, in the symmetry plane all electrons are spatially distributed according to their energy. With different mechanical slits one can select an energy window for the trespassing electrons. In the second half of the monochromator the dispersion is reversed and all electrons leave the monochromator as one beam.

---

[15]Gatan, Inc, United States
[16]Developed and manufactured by CEOS GmbH

The Ω-type monochromator was invented by H. Rose [75] and was designed to fulfill the following requirements within one optical component: (i) A small size, to reduce unwanted artifacts, (ii) a high dispersion, and (iii) no additional resolution limiting aberrations. Especially (i) and (ii) are hard to combine since a high dispersion is connected to an elongated electron trajectory. The solution is a device in which the electrons are deflected along a path that resembles a Ω symbol (see fig. 3.4). The symmetry of the system accounts for the third requirement and assures that the electrons do not exhibit dispersion after they have passed the monochromator. However, the curved electron path results in a more complicated alignment procedure.

In the Ω-type monochromator the electron selection happens in the symmetry plane of the system, where a dispersive astigmatic image of the virtual source is formed. With different slit-apertures one can optimize the energy resolution versus the beam current; the widths of the slits reach from $0.5\,\mu$m to $60\,\mu$m. Since it is a tradeoff between beam current and energy resolution, a slit-width of $1\,\mu$m was chosen, which results in an energy resolution of $150\,$meV at $200\,$kV acceleration voltage, and $90\,$meV at $80\,$kV acceleration voltage. The slit can be moved mechanically by piezo-slides, but the fine-tuning is preferably done by slightly changing the primary electron energy. The monochromator can also be switched off and the microscope can then be operated in conventional mode with a straight beam. Details of the employed monochromator can be found in [76].

3.2.3 Aberration-corrector

There are different types of aberrations in an electron microscope. Some of them can be easily compensated for, while others are much harder to correct. It has already been discussed how chromatic aberrations are minimized by using a monochromator. For other aberrations, some TEMs are equipped with a C_s-Corrector. The C_s-Corrector of the Libra 200 is based on two hexapole corrector elements, which are combined with several other corrector elements and round lenses (see fig. 3.5). The tuning of the corrector is done by a semi-automated software with the Zemlin-tableau method [77]. The Zemlin-tableau method uses the contrast transfer to determine the quality of the beam. A measure for the contrast transfer can be extracted from a diffractogram of a high contrast sample. For this purpose, a silicon membrane with small gold droplets ($< 10\,$nm) is examined. The diffractogram can be derived using fast Fourier transforms (FFT) of the images. In general, a diffractogram shows concentric ellipses, where the spacing and the distortion of the ellipses depend on the aberrations present. For example, a vanishing twofold astigmatism (A_1) results in perfect circles.

Higher order aberrations cannot be seen in a single diffractogram: Therefore, the Zemlin-tableau method combines diffractograms of several tilt angles [78]. The influence of the higher order aberrations increases with increasing tilt angles. A schematic representation of the aberrations on the Zemlin-tableau can be seen in fig. 3.2.3. Since first-order aberrations such as defocus (C_1) and twofold astigmatism (A_1) do not depend on the tilt angle, one can correct these without the tableau. For aberrations of higher order ($n \geq 2$), such as

threefold astigmatism (A_2), axial coma (B_2), spherical aberrations (C_3), star aberrations (S_3), and fourfold astigmatism (A_3), the Zemlin-tableau method is mandatory. Once one of the higher order aberrations has been corrected, the first order aberrations have to be recorrected, before recording the next Zemlin-tableau. A measure for the beam quality is the opening angle, for which the beam is aberration free. For the experiments described herein, the beam was usually corrected for an opening angle of 16 mrad[17].
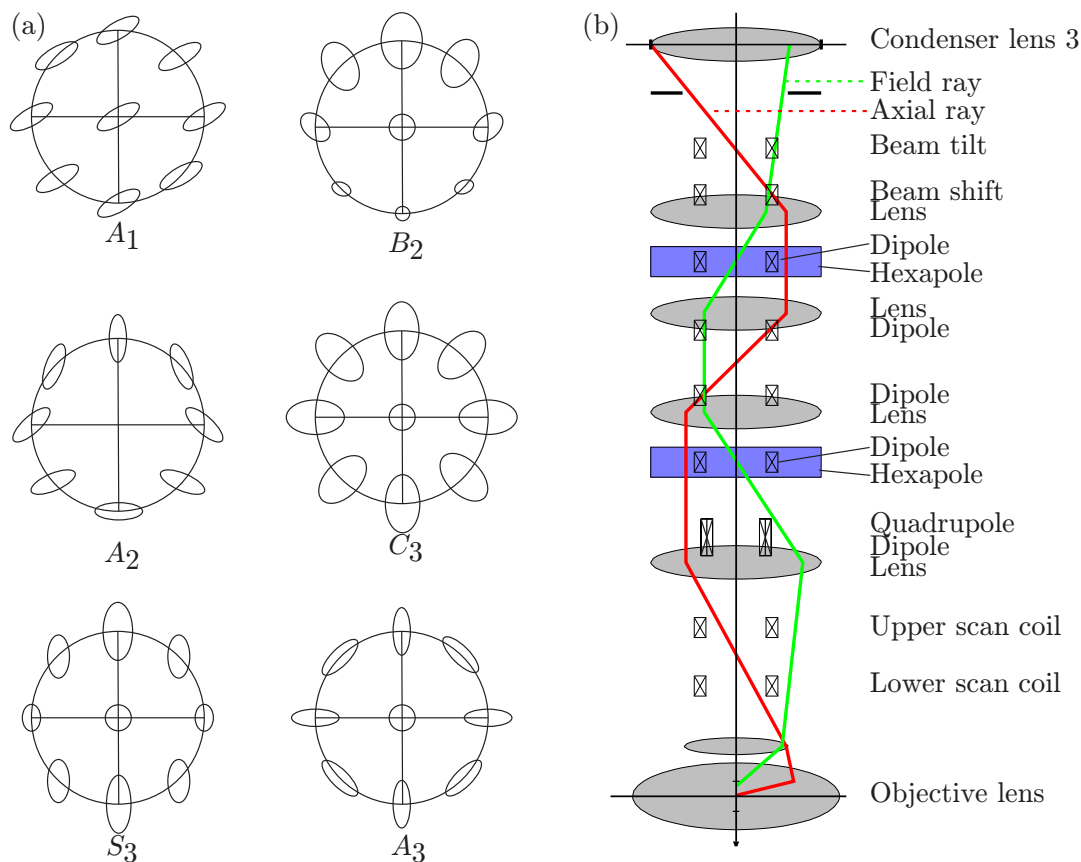
Figure 3.5: (a) Schematic view of the Zemlin-tableau for aberrations up to the third order: twofold astigmatism (A_1), threefold astigmatism (A_2), axial coma (B_2), spherical aberrations (C_3), star aberrations (S_3), and fourfold astigmatism (A_3). The nine (distorted) circles for each aberration represent a FFT from high contrast image acquired under a different angle. (b) Schematic representation of the C_s-Corrector employed in the Libra 200. The red and green lines indicate the pathway of an axial- and field-ray, respectively; adapted from [79].

---

[17]This corresponds to: $C_1 \leq 1$ nm, $A_1 \leq 5$ nm, $A_2 \leq 80$ nm, $B_2 \leq 80$ nm, $C_3 \approx 0$ nm, $S_3 \leq 1000$ nm, $A_3 \leq 1000$ nm.

3.2.4 Energy-filter

Energy-filters are designed to disperse electrons with respect to their kinetic energy. The principle idea is very analogous to the dispersion of white light in a glass prism. Instead of a glass prism, for electrons one can employ magnetic fields that use the Lorentz force to influence the electron trajectory.

Energy-filters can either be mounted on a microscope as post-column filters below the microscope, such as the Gatan imaging filter (GIF) [80, 81], or as in-column filter, such as the Ω-type energy-filter [82, 83] or the mandolin filter [84]. While the post-column filter is based on a single magnetic element, in-column filters use a set of four separate magnetic prisms to disperse the beam. The Libra 200 is equipped with an in-column 90° Ω-type filter [85], which is fully corrected for second order aberrations. The four magnetic prisms are arranged in an Ω-shape, which gives rise to its name. The two facing surfaces in each element are slightly curved to reduce aberrations (not shown). Additional aberration correction is achieved using seven hexapole elements, which are placed between
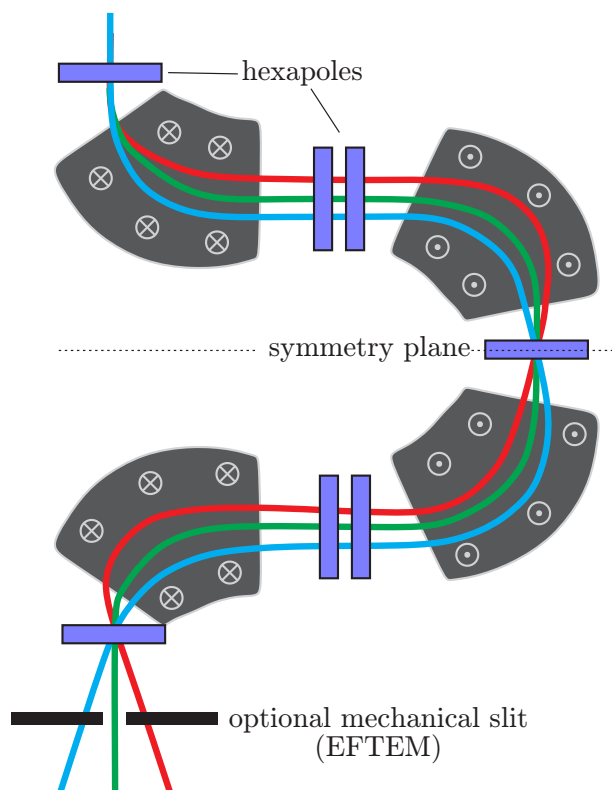

Figure 3.6: Schematic view of an in-column 90° Ω-type filter. Most important are the four magnetic deflector elements in which the electron beam is dispersed. The seven hexapoles correct for aberrations up to the second order. The filter can be employed for energy-filtered TEM (EFTEM) and EELS studies.

the deflection elements (see fig. 3.6). Electrons that enter the spectrometer and have suffered an energy loss (by inelastic scattering in the specimen) are deflected further than those electrons with no energy loss. Thus, at the exit plane (dispersion plane), an electron energy loss spectrum (EEL spectrum) is formed. Note that from the plane perpendicular to the electron beam one spatial coordinate is dispersive, while the other is non-dispersive. Figure 3.6 depicts the in-column energy-filter for electrons with different energies (indicated by their color). Note that electrons that have suffered the same energy loss but enter the filter under different angles travel along different trajectories, but are focused at the same distance on the dispersion axis.

The projector lens system behind the filter can then magnify the spectrum and project it onto a CCD camera. The camera integrates over the dispersion free coordinate and delivers an EEL spectrum with the energy loss on the x-axis and the intensity on the y-axis. For the microscopes at caesar and Harvard, the dispersions are $0.016\,\text{eV/channel}$ and $0.008\,\text{eV/channel}$, respectively. For the calibration of the filter, one can use the L_2 and L_3 edges of rutile (TiO_2), which have a well-known energy difference of $\Delta E = 7.5\,\text{eV}$ [86]. The energy-filter can also be used for energy-filtered TEM (EFTEM). A mechanical slit after the energy-filter selects electrons with a certain amount of energy. The transmitted electrons are then used to form an image.

3.3 Electron energy loss spectroscopy (EELS)

The major part of the experimental work in this thesis was done with a scanning transmission electron microscope (STEM). In contrast to traditional TEM, in STEM the sample is not illuminated all at once, but by a tightly focused beam, which is raster scanned over the sample. This technique provides the advantage that a spectroscopic measurement can be made at each position of the electron beam. The employed electrons have energies on the order of $200\,\text{keV}$, and thus a broad range of excitations and scattering processes are possible. Elastically scattered electrons only change their momentum and do not transfer energy to the specimen. Therefore, these electrons do not contribute to the spectroscopic measurements but only for imaging, i.e., they are collected by one of the two dark field detectors. The inelastically scattered electrons on the other hand, do transfer energy to the specimen, e.g., in form of excitations of the core or valence electrons. The excited specimen can in turn release this energy in form of secondary electrons or photons. The energy spread of the latter is quite immense.

This thesis focuses on the detection of primary electrons, which have 'lost' some of their energy in the specimen. At each position of the electron beam, the energy-filter is used to acquire an EEL spectrum, i.e., an intensity profile of the energy loss. In general, an EEL spectrum can be divided into two energetic regions: The "low-loss" region, with energy losses up to $50\,\text{eV}$, and the "core-loss" region with energy losses higher than $50\,\text{eV}$. The core-loss region provides direct elemental and structural information about the specimen. This information is provided mainly by electron excitations from the inner or core shells.
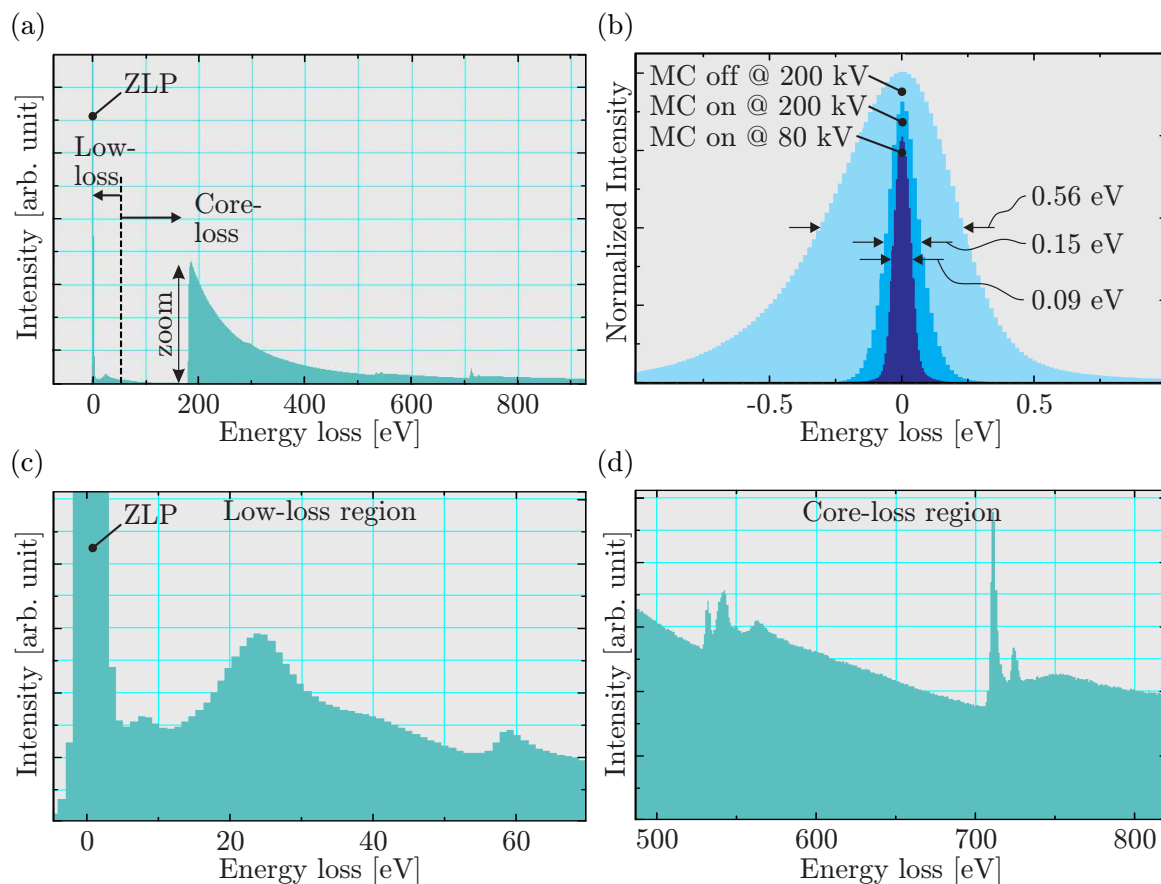
Figure 3.7: (a)Electron energy loss spectrum of a Fe_2O_3 sample. (b) The zero loss peak (ZLP) for different acceleration voltages and monochromator (MC) settings. (c) A close-up of the low-loss and (d) the core-loss region of the Fe_2O_3 spectrum.

For example, the ionization energy of a K-shell electron of a lithium atom is 55 eV, while a K-shell electron of uranium has an ionization energy of 99 keV [73]. In Figure 3.7 (a,c,d) the electron energy loss spectrum of Fe_2O_3 is depicted, where the L_2 (excitation of the 2p electron of the L-shell) and L_3 edges of iron are emphasized (at ~ 720 eV).

Figure 3.7 (c) shows the zero loss peak (ZLP) at an energy loss of 0 eV. This peak is very intense since it represents all electrons that did not change their energy. Right next to the ZLP, there is the low-loss region with an obvious resonance arising due to the excitation of a bulk-plasmons. The core-loss region can be found at higher energy losses (see fig. 3.7 (d)); the overall signal intensity drops with increasing energy loss and reaches negligible values for a few keV (not shown).

The energy resolution of an electron microscope is defined by the FWHM of the ZLP. It is mainly determined by the electron source, the monochromator slit width, and the spectrometer. Figure 3.7 (b) shows the ZLP for different settings of the microscope. The broadest peak corresponds to an acceleration voltage of 200 kV, with the broadest

monochromator (MC) slit (60 μm). This resembles the situation of the monochromator in the off-state. The other two peaks show the ZLP of the microscope located at caesar (200 kV) and the microscope located at Harvard (80 kV) with 1 μm[18] monochromator slits.

3.3.1   STEM-EELS acquisition and EELS maps

For the data acquisition in STEM, the tightly focused electron beam raster scans over the specimen and stops after defined intervals. At each position the beam stops for a defined time, typically from a few milliseconds up to several seconds. In normal imaging mode, electrons scattered from the specimen are collected by a high angle annular dark field detector (HAADF detector, a ring detector that integrates all counts and delivers one value for each beam position). The resulting HAADF images are dark-field images, where objects with a high scattering cross-section (e.g., gold) appear bright and objects with a small scattering cross-section (e.g., Si_3N_4) appear dark.

Electrons that did not change their trajectory in the specimen are dispersed in the energy-filter and the dispersive plane is projected onto the CCD camera. The camera records a separate spectrum for each position of the electron beam on the sample. The result is a three dimensional data-cube, where x and y are spatial coordinates, and the third axis is an energy loss spectrum. This is illustrated in figure 3.8 (a). This data-cube (or spectrum image) allows for the extraction of single spectra, as well as a xy-plane, where the intensity of a certain energy loss is displayed from each spectrum. Such a plane is called an EELS-map. The x and y coordinates of the EELS-map represent spatial coordinates of the specimen while the color code represents the intensity of the energy loss. For the experiments of this work, bright colors are connected to a high intensity (and thus a high energy loss probability), while dark colors are connected to a low intensity (and thus a low energy loss probability). The extraction of an EELS-map is shown in figure 3.8 (b).

Experimental procedures and microscope settings
For the experiments, samples were mounted in a high tilt tomography sample holder[19]. This sample holder allows tilt angles up to 70° and a rotation around the surface normal of the sample. The silicon chip with the Si_3N_4-membrane was fixed in the TEM holder by a manually modified clamp ring. The clamps in the original clamp ring point away from the sample. In the modified version the clamps point inwards, which allows for a more secure fixing of the sample. Before the sample holder was inserted into the microscope, the sample was plasma cleaned[20] in an oxygen plasma for two minutes. The plasma removes organic residues on the samples and prevents carbonate contamination on the

---

[18]The monochromator allows for a smaller slit (0.5 μm) which results in a better energy resolution. Since the experiments were performed with the 1 μm slit, those ZLPs are illustrated.

[19]Model 2040, E.A. Fischione Instruments, Inc., PA, USA

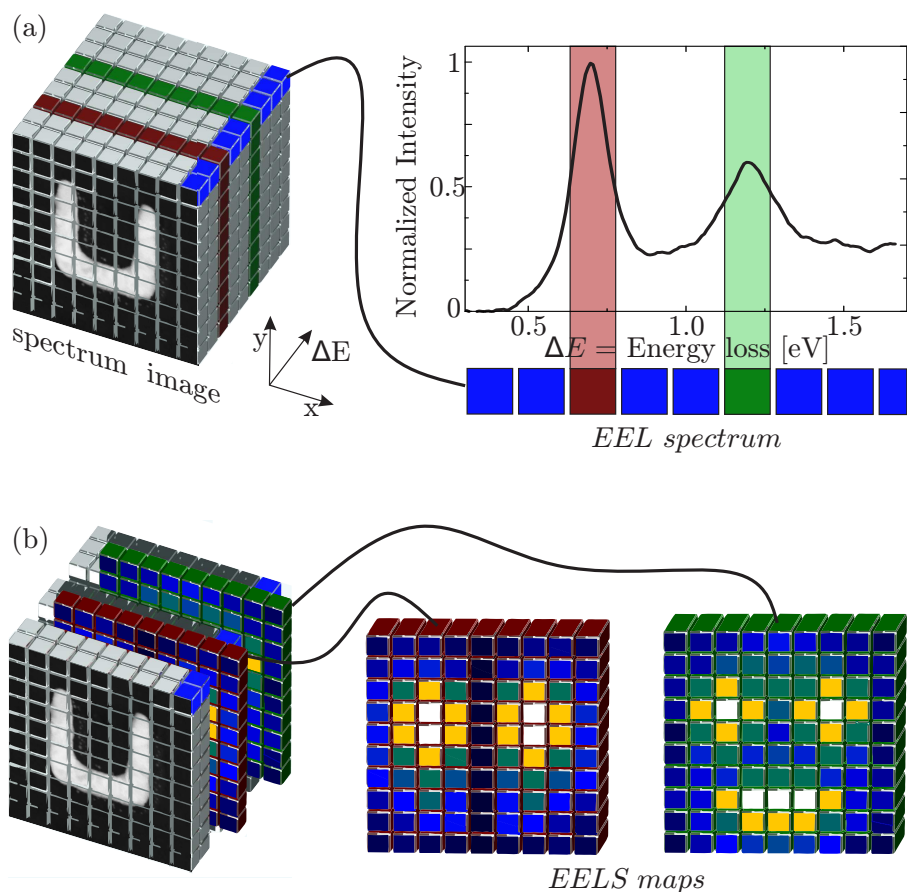[20]Fischione, plasma cleaner model 1020. Gas: 25% oxigen + 75% argon.

Figure 3.8: Acquisition procedure in STEM-EELS. (a) In a pre-defined region, the electron beam is raster scanned over the sample, and pauses for a defined time at predefined positions. In the illustrated example, the scan area is in the x and y directions, with nine pixels in each direction. At each of the $9 \times 9 = 81$ pixels, the electron beam pauses and an electron energy loss spectrum is acquired. For the top-right pixel such a spectrum is shown in detail on the right hand side of (a). The combination of the 2D (sample-) image and the 1D spectrum (one spectrum for each pixel) leads to a 3D data cube, the "spectrum image". The spectrum image thus contains of two spatial coordinates x and y, and the energy loss in the third dimension. (b) The spectrum image can be sliced into images, which display the energy loss intensity for different energies. Such an EELS map is shown on the right hand side of (b) and consists of the spatial coordinates from the spectrum image, where each pixel represents the intensity of the energy loss at this position. The color scale shows high intensities with bright colors and low intensities with dark colors.

sample during scanning inside of the TEM. The transfer to the microscope should be executed immediately after the plasma cleaning, to avoid further contamination in the atmosphere. Before the sample holder is inserted, the microscope should already be in perfectly aligned STEM mode (especially the C_s-corrector). The alignment procedure for STEM will not be discussed here (see [73]).

The following microscope settings (from top to bottom) were used in spectroscopy mode: The monochromator was used with a 1 μm slit. For the condenser system, the best tradeoff between resolution and intensity was found for a 25 mrad aperture. The camera length was set to 720 mm and for the energy-filter entrance plane, the smallest aperture (40 mrad) was used. Thus, the system was operated with a beam convergence semiangle of 25 mrad and a collection semiangle of 7 mrad. The alignment of the spectrum was done in spot mode, i.e., the beam was kept fixed at a position (next to the gold structure, on the Si_3N_4-membrane). The spectrum focus (width of the ZLP) was aligned and the spectrum rotation was corrected. For fine-tuning, the gun-lens voltage was changed by a few volts. An indicator for the optimal gun lens value is the total counts on the CCD. These three steps were repeated until the alignment was satisfying. Note that the zero loss peak does not necessarily have to be centered at 0 eV. This can be done during data processing. Indeed, for the microscope located at caesar, it is mandatory to shift the ZLP by about 5 eV (usually this was done to negative values). This has no effect on the measurement but is needed to avoid the recording of a mirror ZLP, which appears as an artifact on the CCD camera. The origin of this peak was not found, but with the above procedure its appearance can be avoided.

The 16 bit CCD camera allows for a maximum of 65,535 counts per pixel. To avoid saturation or damage of the camera or the fluorescence screen, the acquisition time per spectrum was chosen such that the maximal counts per pixel were between 25,000 and 30,000 (electron probe on the Si_3N_4). Typically, the acquisition time per spectrum was between 0.2 and 0.7 seconds. The spatial step width between two spectra is in principle arbitrary, though one has to take into account that the stability of the microscope is finite. For the experiments in this work, the microscopes showed a stable behavior for up to 10 hours before the spectrum had to be re-aligned (in worse situations, the C_s-corrector also needs to be realigned, which is associated with a specimen change). This limits the total number of spectra that can be acquired to about 15,000 (120×120). Therefore, the step width of the electron beam was typically between 3 nm and 7 nm. The acquisition time and step width are set in the DigitalMicrograph software, which can also be used to correct for the sample drift. The drift is calculated and corrected after every 100 spectra via a cross-correlation. The correction is automated, but accounts only for drifts along the x- and the y-axis. The defocus cannot be automatically corrected, but it can (if necessary) be done manually.

Data processing

The data processing includes several steps, which will be listed chronologically:

- Due to instabilities of the microscope, the zero loss peak is not always centered at exactly the same position. Over short time periods (between two successive spectra) the spectrum moves up to 200 meV. Over long time periods on the order of hours, this shift can be a few eV. To correct for these shifts, the DigitalMicrograph software has implemented a tool to align the center of each ZLP, and to set this position to 0 eV (see fig. 3.9 (a)).

- When the electron beam is scanned over the sample, it interacts with different materials and penetrates different thicknesses. Obviously, the total intensity of the transmitted beam strongly depends on its position. Therefore, each spectrum has a different intensity. To account for that, each spectrum was normalized by its total number of counts. This was done via a self-written DM-script (see fig. 3.9 (b)).

- The spectra are now aligned and normalized. When a single low-loss spectrum is considered, the predominant feature is the ZLP (see fig. 3.9 (c)). Magnifying the spectrum reveals the actual (plasmon) resonances that are of interest. As can clearly be seen in figure 3.9 (d), the resonances overlap with the tail of the ZLP. Thus, the ZLP has to be subtracted from the spectrum. For the subtraction, different approaches were tested (pre-measured ZLP, reflected tail, Gaussian and Lorentzian fits, ...). A power law fit to the tail showed the best results. The fit region should be clearly separated from the plasmon resonances to avoid artifacts (red area in fig. 3.9 (d)). The fit was done individually for each spectrum.
  This procedure was developed for spectra recorded with a 200 kV acceleration voltage (energy resolution 0.15 eV) and was consistently used for the spectra recorded at 80 kV (energy resolution 0.09 eV) acceleration voltage, although in the latter case the peaks were clearly distinguishable (see fig. 3.9 (f-h)). In other microscope setups, where the energy resolution is not as good as in the present case, data processing includes lengthy deconvolution algorithms to extract the signal (as, e.g., [15]).

- To reduce the signal to noise ratio in the displayed spectra, 15-30 individual spectra are averaged. To reduce the signal to noise ratio in the displayed EELS maps, two adjacent EELS maps are averaged. With a dispersion of 0.016 eV/channel, the presented energy window of an EELS map is thus 0.032 eV.
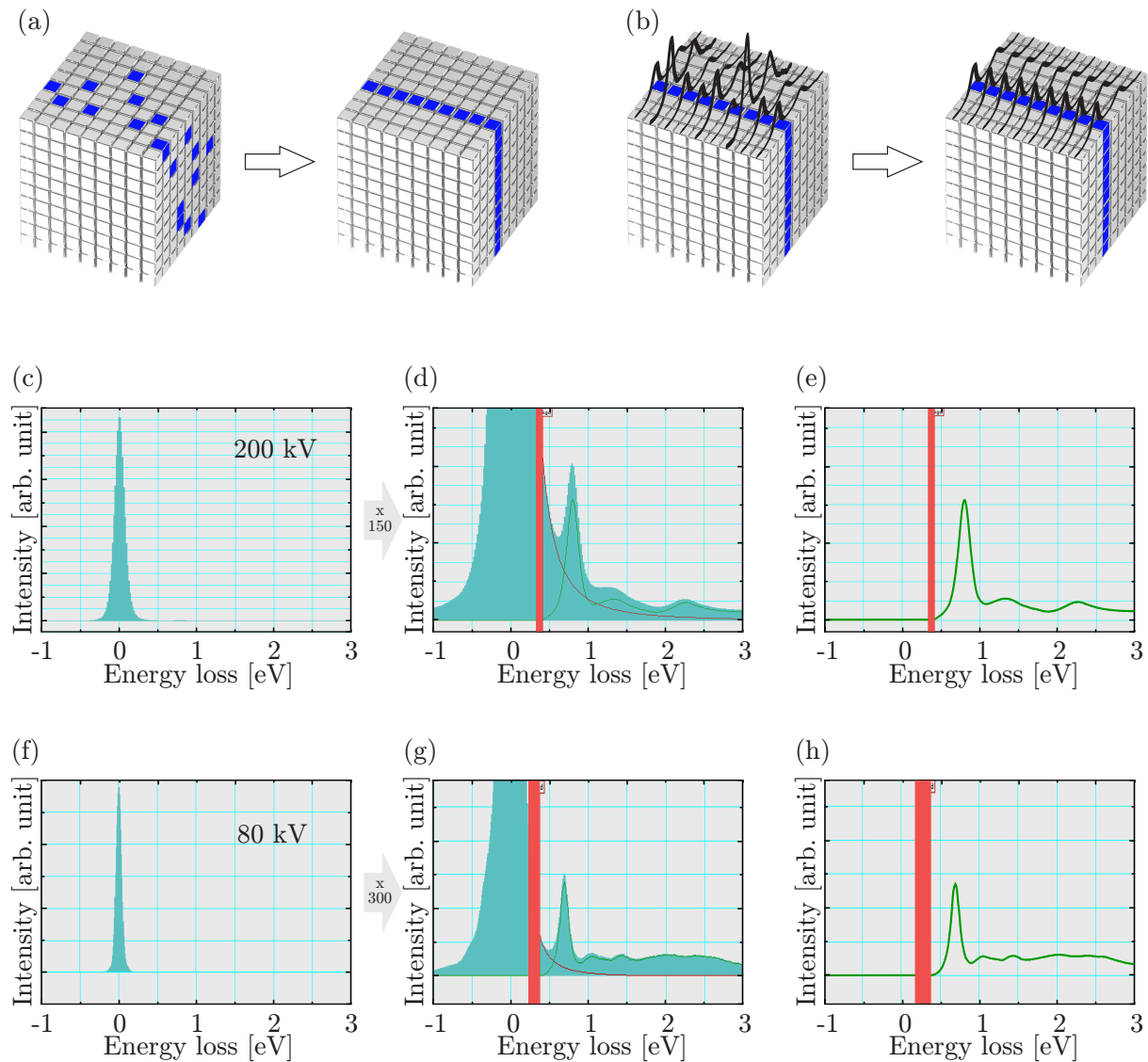
Figure 3.9: A schematic view of the data processing. (a) The centers of the ZLP are aligned and set to zero. (b) Each spectrum is normalized by its total number of counts, to account for different absorptions in the sample. (c) The low-loss spectrum of a plasmonic structure; the plasmon resonances become visible by magnifying the spectrum with a factor of 150. (d) The magnified spectrum shows an overlap of the ZLP-tail and the resonances. Therefore, a power law function is fitted to the ZLP-tail (in the red region) and subtracted from the spectrum. The final spectrum is shown in (e), where the plasmon resonances are clearly visible. (c-e) Show the subtraction procedure for a spectrum acquired with 200 kV acceleration voltage, (f-h) for 80 kV acceleration voltage.

3.4   Discontinuous Galerkin time-domain simulations

In order to compare the measurements with theory, numerical ab-initio calculations of the electron energy loss spectra were performed. The calculations were made by a group initially located at the Karlsruhe Institute of Technology, consisting of: Dr. Jens Niegemann (now ETH Zürich), Dr. Richard Diehl, and Prof. Kurt Busch (now HU Berlin). Since the near fields of plasmonic nanostructures are highly sensitive to the geometrical details of the system, one needs a simulation technique which allows for accurate modeling of the rounded geometry of the nanostructures. For this work, a nodal discontinuous Galerkin time-domain (DGTD) method was employed [87]. It is well suited for the efficient and accurate simulation of plasmonic nanostructures [88, 89]. In the discontinuous Galerkin method the considered (nano-) structure is divided into a set of sub volumes (tetraeders), which form a mesh (see fig. 3.10 (c,f)). Each element is initially considered separately, with its own set of basis functions. These basis functions are zero on all other elements, especially on the neighboring elements. This leads to two different field values on the interface between two neighboring elements, and allows for a discontinuous representation of electromagnetic fields at the interface of two materials. Thus, each element can be treated separately and the electromagnetic field of complex structures can be reduced to a set of small, manageable matrices. Nevertheless, the single elements have to be coupled in some way to allow for wave propagation. This is done using the concept of numerical flux, which is borrowed from finite volume methods [90]. It leads to a semi-discrete description of Maxwell's equations, with a discretized position dependence. For details of the DGTD method please see [33].

Recently, it was demonstrated that one can extract electron energy loss spectra from DGTD calculations [91]. For the simulations a tightly focused electron beam excites an electromagnetic field, which then acts back on the electrons and causes an energy loss. This energy loss is then recorded. All numerical calculations in this work follow the procedures described in [91] with the exception that a pure scattered-field excitation was used instead of the total-field/scattered-field source originally proposed. This allows for the calculation of electron energy loss spectra for electron beams penetrating the plasmonic nanostructures. The calculations include the 30 nm thin Si_3N_4-membrane, where a refractive index of $n = 2$ was assumed. In order to calculate accurate EELS distributions of large structures, the code was ported to run on graphics processing units (GPUs). All calculations were performed on NVIDIA GeForce GTX 580 cards, which led to a speed-up factor of more than 50 for the calculations when compared to equivalent calculations on a traditional CPU.

Since the DGTD method is a time-domain approach, one needs to employ a suitable material model to describe the dispersive response of gold [89]. Therefore, a Drude-Lorentz model is used, given by (see 2.14):
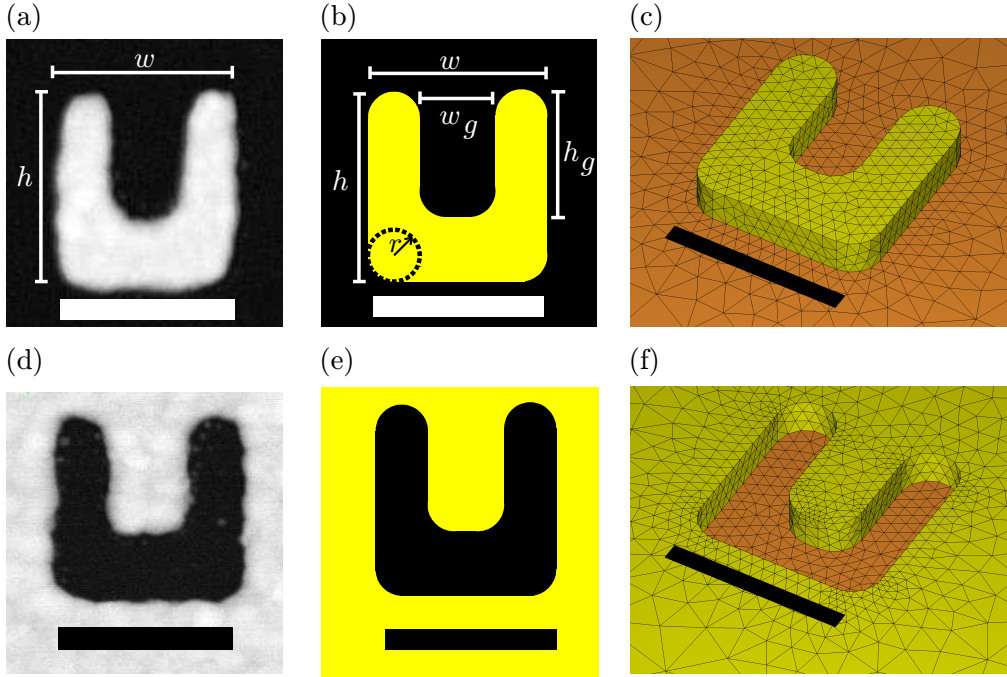
Figure 3.10: (a) HAADF image of a typical SRR fabricated using electron beam lithography. The HAADF image is the foundation for the geometry of the SRR assumed in the DGTD calculations (b). (c) Mesh of the SRR for the coarsest refinement. (d) HAADF image of the corresponding complementary SRR. (e) Geometry and (f) mesh of the CSRR. The scale bars are 200 nm.

$$\epsilon(\omega) \;\; = \;\; \epsilon_\infty - \frac{\omega_{\mathrm{pl}}^2}{\omega^2 + \imath\gamma_{\mathrm{D}}\omega} - \sum_j \frac{\Delta\epsilon_{\mathrm{L},j} \cdot \omega_{0,j}^2}{\omega^2 - \omega_{0,j}^2 - \imath\gamma_{\mathrm{L},j}\omega} \; . \tag{3.1}$$

The free parameters are determined by fitting the model to experimental data of Johnson and Christy [92] in the wavelength region from 500 nm to 2000 nm. This results in $\epsilon_\infty = 6.21$, $\omega_{\mathrm{pl}} = 8.794$ eV, $\gamma_{\mathrm{D}} = 0.066$ eV, $\Delta\epsilon = 1$, $\omega_0 = 2.646$ eV, and $\gamma_{\mathrm{L}} = 0.382$ eV.

3.5   Optical spectroscopy

There is a wide spread of alternatives for the investigation of plasmon resonances, and some of them are based on optical spectroscopy. The spatial resolution of optical experiments is obviously not even close to the resolutions achievable with electron microscopes. However, optical spectroscopy itself is far more advanced and allows for a higher energetic resolution. Most optical experiments are not designed to investigate single nanostructures

but arrays of nanostructures, with total sizes of several hundred μm^2. There are only a few optical techniques to examine single structures; one experiment capable of this was set up and run by Dr. Martin Husnik, who finished his PhD on that topic in the group of Prof. Martin Wegner at the Karlsruhe Institute of Technology, in Karlsruhe, Germany [11,93]. The biggest challenge in investigating single nanostructures is that the cross section of the nanoparticle is small compared to the cross section of the laser beam. Therefore, the extinction signal of the nanoparticle is very small and in the range of the noise of the detector. To better detect the small signal a spatial modulation technique is employed, which enhances the signal-to-noise ratio and reveals the relative signal drop caused by a nanoparticle. The technique was developed in 2004 by Arbouet et al. [94] and was applied to spherical gold nanoparticles in 2006 [10].

Figure 3.11 (a) shows the simplified setup of the experiment: A laser beam is focussed by a microscope objective onto the sample, which is mounted on a 3D piezo stage. Behind the sample, the beam is collected by a second microscope objective and analyzed by a detector. Before the beam hits the sample, it is spatially modulated by a mirror. The mirror is moved sinusoidally, causing a lateral shift of the focus on the sample in the range of a few μm (see fig. 3.11 (b)). The same modulation signal is send to a Lock-In amplifier, which multiplies it with the detector signal, integrates over a specific time, and delivers the desired output signal. By knowing the size of the focused laser beam one can calculate the real part of the scattering amplitude from the difference between the signals with the nanostructure interior and exterior the laser spot. From the scattering amplitude, one can calculate the extinction cross section [11]. In order to find the nanoparticle on the sample, the sample is moved in the plane perpendicular to the propagation direction of the laser, and at each position the signal of the Lock-In amplifier is recorded. This leads to a 2D map, which clearly indicates at which position the sample is located. This movement is completely independent of the modulation of the focus position. Once the position of the nanoparticle is known, the spatial modulation technique is performed for different wavelengths. A white light laser is filtered by a monochromator, which selects one wavelength out of the broad spectrum of the laser. For each selected wavelength the modulation signal is recorded, and the extinction cross section is calculated. This leads to a spectrum as shown in fig. 3.11 (c). The experiment can be performed with different polarizations, as is indicated by the colored arrows in the inset of 3.11 (c).
Husnik et al. further developed the spatial modulation technique by combining it with an interferometer setup (not shown). From the interference of a reference beam with the beam that interacted with the nanostructure, one can extract the phase information and thus measure the imaginary part of the extinction cross section. Hence, the absolute extinction and scattering cross section and thus the absolute absorption cross section of single nanostructures can be calculated [95].
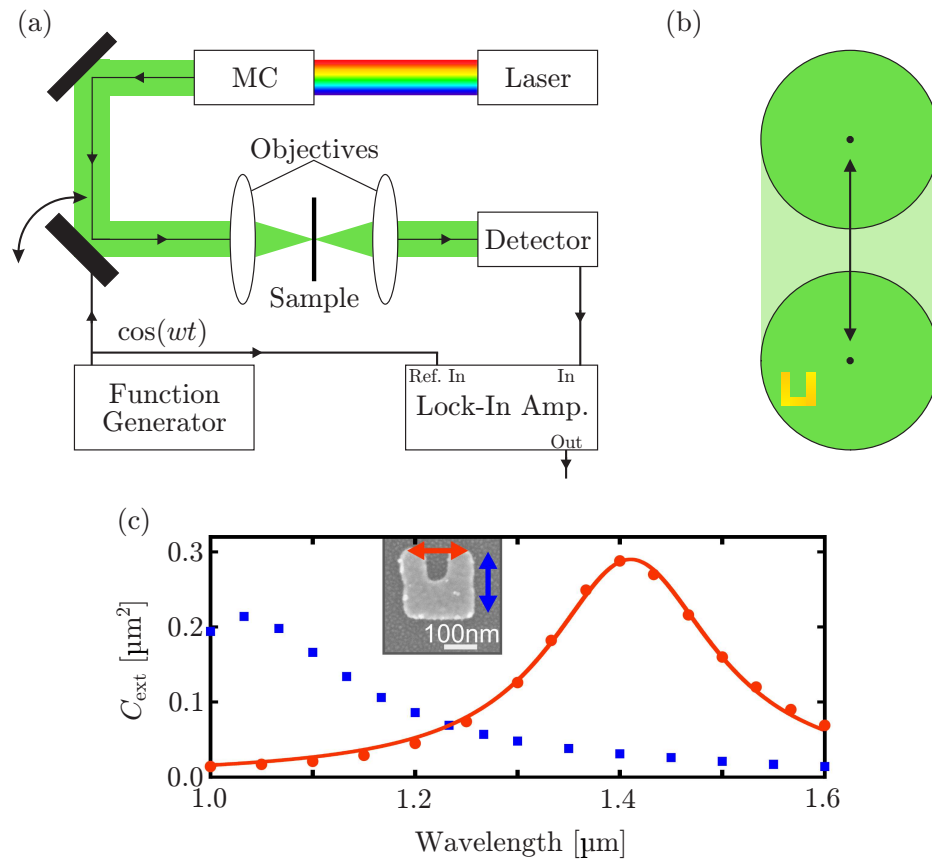
Figure 3.11: (a) Shows a simplified version of the experimental setup of the spatial modulation technique. A sinusoidal modulation of one mirror helps to detect small signal changes with the Lock-In technique. The monochromator (MC) allows for a selection of different wavelengths of the white light laser. (b) Shows the modulation of the Gaussian beam focus over a nanostructure, in this case a SRR. The Lock-In amplifier enables the measurement of small differences in the intensity of the beam on the sample and next to it. From this signal difference, one can calculate the extinction cross section for each wavelength, which leads to a spectrum as depicted in (c). The red dots show the signal of a horizontally polarized laser (polarization parallel to the SRR bottom wire). In this configuration, the first-order mode is excited. The solid line is a Lorentzian fit to the data. The blue data points correspond to a vertical polarized laser beam (second-orde mode). (c) Is taken and adapted from [11].

Chapter 4

EELS on individual plasmonic nanostructures

In this chapter, EELS measurements on isolated split-ring resonators are presented. The discussion of the measurements will first focus on the question of how to interpret the EELS data. Single spectra from different positions on the SRR are depicted and show, at which energies the excitation of the different plasmonic modes is possible. Furthermore, the spatial mode profiles will be discussed on the basis of EELS maps. With the knowledge of how to interpret the EELS measurements, this chapter then covers the effects of size scaling on the plasmonic modes of SRRs. Furthermore, the comparison of the plasmonic maps of a SRR and the corresponding complementary SRR allows for a direct visualization of Babinet's principle. This chapter closely follows [66].

4.1   The split-ring resonator (SRR)

4.1.1   Electron energy loss spectra

In a classical picture, the energy loss experienced by an electron results from the work done by the electron against the induced electric field of the excited mode (see section 2.3.2). A strong EELS signal occurs if the plasmonic mode has a large electric field component E_z along the trajectory (z-axis) of the electron [15]. For planar metallic nanostructures like SRRs, a large E_z-component is connected to the antinodes of the charge density oscillation. Hence, the EELS map of a given mode qualitatively resembles its charge density distribution. Individual EEL spectra, acquired at distinct positions, therefore reveal diverse features.

Figure 4.1 (a) shows a HAADF image of a SRR with a width of 220 nm. The three colored dots mark positions where the three exemplary spectra were acquired. The spectrum
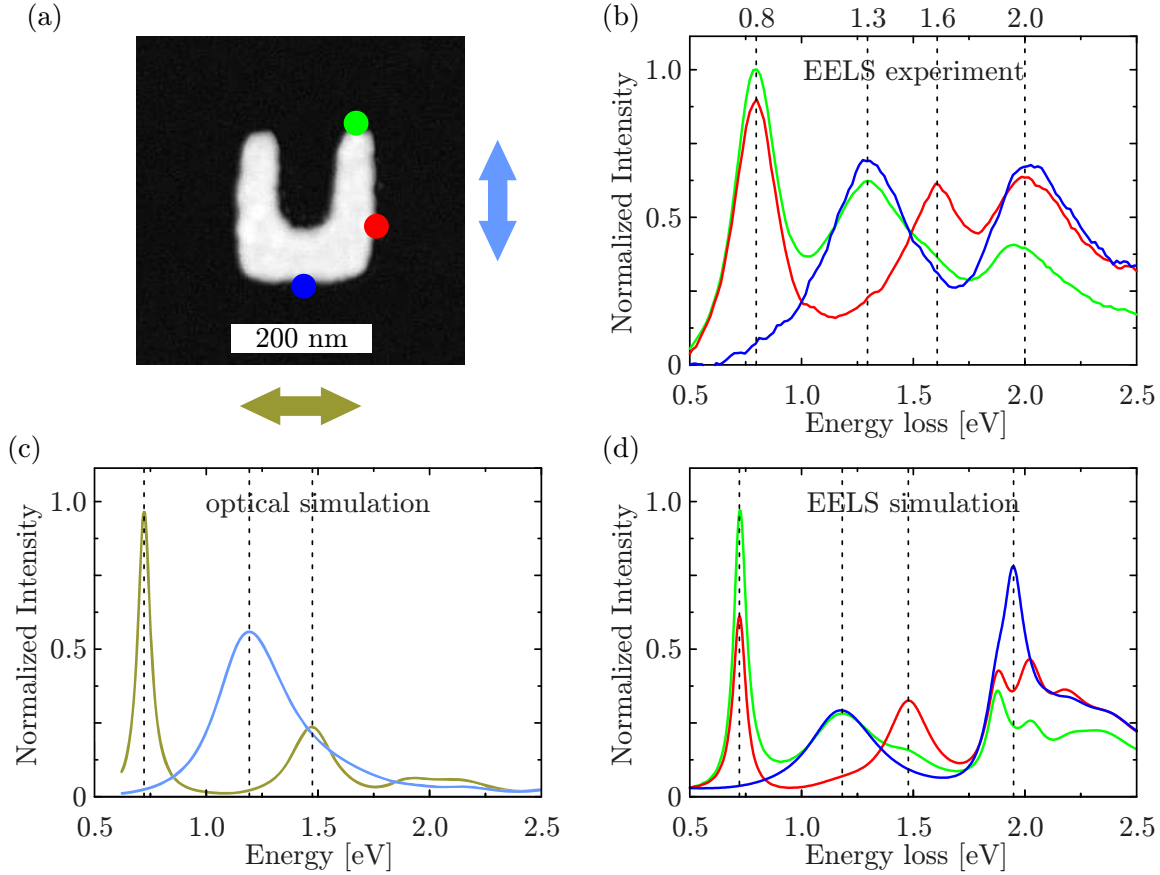
(a)

(b)

(c)

(d)

Figure 4.1: (a) Shows a HAADF (high angle annular dark field) image of the considered SRR, the two arrows indicate the two polarizations for the optical simulations. The three colored dots represent the positions, where the EEL spectra were recorded. (b) Shows the experimental spectra acquired at those positions and (d) shows the corresponding simulated EEL spectra. (c) Depicts simulated optical spectra. The overall agreement between experimental and simulated data is quite well. However, at higher energies the three graphs slightly differ.

from the top end of the arm (bright green in fig. 4.1 (b)) shows three clearly distinguishable resonances located at 0.8 eV, 1.3 eV and 2.0 eV. These three resonances correspond to three different modes that can be excited at this position. When one considers the spectrum from the center right part of the SRR (red spectrum), one finds three maxima located at 0.8 eV, 1.6 eV and 2.0 eV, respectively. The resonances at 0.8 eV and 2.0 eV correspond to the two modes already observed in the spectrum from the top end of the arm, but the resonance at 1.6 eV indicates a new mode, not found in the previous spectrum. Indeed, a closer look shows that this mode is also present in the green curve, though only as a faint shoulder of the second peak. The third spectrum from the bottom center of the SRR (blue curve) shows only two resonances, corresponding to two modes already found in the previous spectra. The spectra in figure 4.1 (b) thus indicate that there are at least four different plasmonic modes on the SRR which cannot be excited at every position on

the SRR. An electron penetrating the bottom center of the SRR can, for example, not excite the first plasmonic mode (at 0.8 eV).

The experimental findings can be compared with numerical simulations. For this, the HAADF image of the SRR (fig. 4.1 (a)) is analyzed and the dimensions are used to model a SRR for the discontinuous Galerkin time-domain (DGTD) simulations. The simulated EEL spectra are shown in figure 4.1 (d) and have the same color code as the experimental spectra. Considering the first three resonances, one finds a good agreement between the experimental results and the simulations. The peak positions of the simulated data are slightly red shifted. This can most likely be traced back to the sample designs of the simulated and the experimentally investigated structure. Obviously, the structure employed for the experiments contains impurities and has small deviations from the simulated structure. The chromium layer beneath the gold film is not considered with an individual dielectric function. The sample thickness is another uncertainty. The nominal thickness of the sample is 37 nm (2 nm Cr and 35 nm Au), but small changes in the thickness result in a shift of the resonance energies [49] as well as in a change of the dielectric function of gold.

The second difference between the experimental and simulated data is the line width of the peaks. While the line width in the experimental data is broadened by the microscope (determined by the energy resolution), the simulations do not suffer this broadening. Therefore, the simulated data show much smaller line widths. This leads to the discussion of the fourth resonance found in the experiments. The simulations reveal that this peak is actually a superposition of two or three peaks. In other words: from the spectra of the measured positions, one detects only four modes, while the simulations predict up to six modes. This can be attributed to the peak broadening of the microscope. To see in detail which mode can be excited at which position, one needs to take a look at the EELS map of the SRR. Before this topic is addressed in the next section, simulated optical spectra are discussed.

The optical simulations, i.e., the excitation of the SRR with an electromagnetic wave instead of an incident electron, were performed for polarizations perpendicular and parallel to the arms (olive-green and light-blue in fig. 4.1 (c), respectively). The first three resonances are clearly visible and match the EELS data. However, the higher energy modes cannot be found in the optical spectra. This is due to the small electric dipole moment of these modes, which leads to a small excitation probability by the incoming wave.

4.1.2 EELS maps

Before the EELS maps are presented, the anticipated EELS intensity distributions are discussed for different resonances of a SRR. From section 2.3.2 one expects the modes of a SRR to be plasmonic resonances of increasing order in the entire structure [15,96]. To a first approximation, the current density distribution of the m-th plasmonic mode is a simple standing wave with nodes at the ends and m-1 nodes distributed along the SRR. The locations of the current density nodes coincide with the antinodes of the charge

density oscillation. For example, the first mode (m = 1) exhibits antinodes of the charge density oscillation at the two ends of the SRR and the second mode (m = 2) has an additional antinode in the middle of the SRR. Hence, one expects that the EELS map of the first mode has a maximum at each end of the SRR. For the EELS map of the second mode, one anticipates three maxima - two at the ends and one in the middle of the SRR. The number and locations of the EELS maxima of the higher-order SRR modes can be deduced from analogous considerations. In general, an alternating series of even and odd numbers of EELS maxima is expected [15].
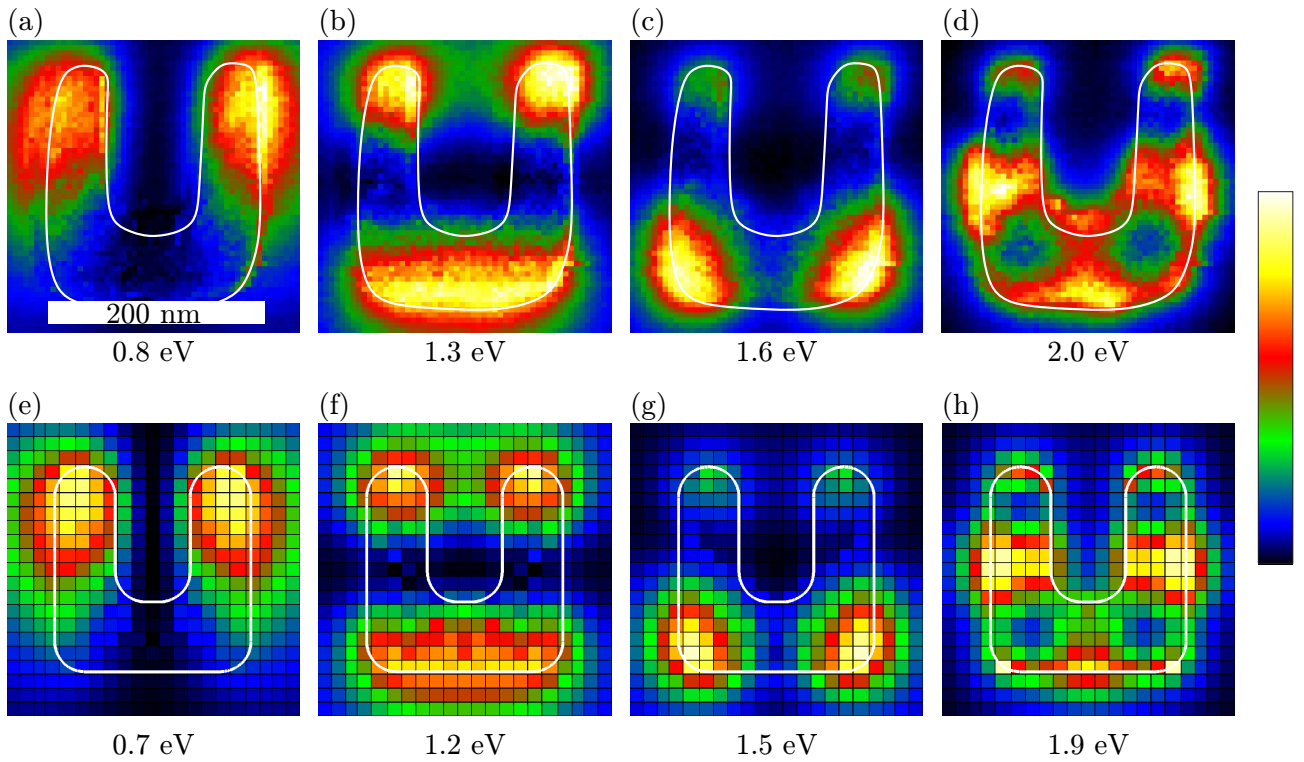

Figure 4.2: EELS maps of the SRR depicted in fig. 4.1 (a). The top row (a-d) shows the first four modes found in the experiment, with resonance energies corresponding to the values found in the spectra (see fig. 4.1 (b)). Bright areas correspond to a high energy loss probability and thus to a region with a strong electric field component E_z (with the electron trajectory in z-direction). Dark regions correspond to a low energy loss probability. In (e-h) the simulated EELS maps are depicted, the displayed energies correspond to the values from the simulated spectra (fig. 4.1 (d)) and are slightly red shifted compared to the experimental findings. The white lines indicate the boundaries of the SRRs.

Figure 4.2 shows the EELS maps of the SRR depicted in figure 4.1 (a). The center energies of the EELS maps correspond to the resonance energies of the plasmonic modes from 4.1 (b). Each EELS map has an independent color scale in which small signals are represented by dark blue and large signals by bright yellow. As expected, one finds for

the first mode (0.8 eV) strong EELS signals at the two ends of the SRR. The EELS map of the second mode (1.3 eV) exhibits an additional strong maximum in the bottom wire. Significant EELS signals at the lower corners partially stem from the low energy tails of the third resonance (1.6 eV). The EELS maps of the third and fourth mode (2.0 eV) exhibit four and five maxima, respectively. In a second step, one can now take a look at the simulated EELS maps shown in figure 4.2 (e-h). As expected from the spectra shown in the previous section, the resonance energies are slightly red shifted. Nevertheless, the mode profiles of the four modes perfectly match the mode profiles found in the experiment.

In section 2.3.2 the modes of a SRR were connected to charge density oscillations. For example the first resonance shows two opposite charge densities at the two arms. Thus, one would intuitively expect "opposite" EELS signals at the two arms of the SRR. Though, the EELS map (figure 4.2 (a)) exhibits identical signals at the two arms. This is due to the lack of phase sensitivity of EELS [97], i.e., at each position of the electron beam, the mode is either excited or not. Therefore, the electrons either lose energy or not. The phase information can not directly be extracted from the EELS maps. To determine the phase information of the plasmonic modes one has to utilize simulations.
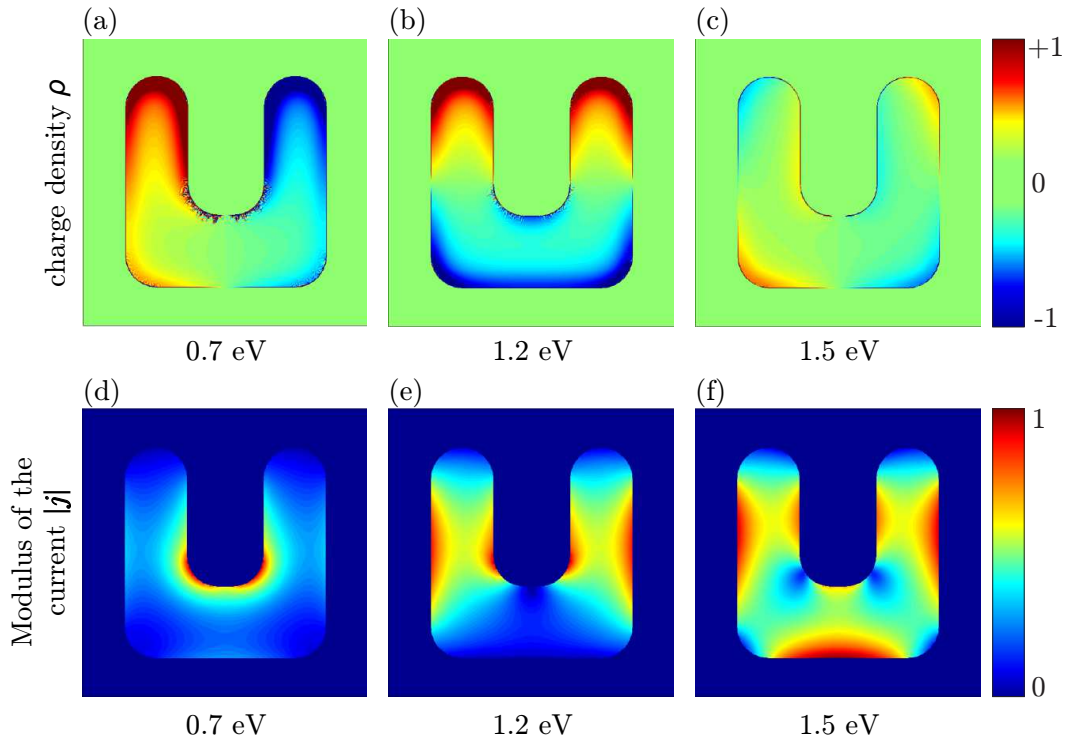

Figure 4.3: (a-c) Simulated snapshots of the charge density (ρ) for the first three modes of a SRR. The current j can be calculated via the continuity equation and its modulus is shown in (d-f).

Figures 4.3 (a-c) show snapshots of the charge density distribution for the first three SRR modes. As expected, the first mode shows a positive charge density at the one arm, and a negative charge density at the other. The second mode shows three charge densities; two positive charge densities at the arms, and a negative charge density at the bottom wire. The third mode also shows the expected charge density distribution. The phase information of the three modes can be used to calculate the current ($\boldsymbol{j}$), resulting from the charge separation (via the continuity equation $\frac{d}{dt}\rho + \nabla\boldsymbol{j} = 0$). In figure 4.3 (d-f) the modulus of the current ($|\boldsymbol{j}|$) is plotted for the first three modes. As expected, the first mode shows a strong current from one arm to the other (responsible for the magnetic moment discussed in section 2.3.1). The higher modes also show the expected behavior.

With the knowledge of how to read EELS maps and single spectra, and by knowing what information can be provided by the simulations, one can now go one step further. For example, one can investigate the influence of the size of the SRR on the plasmonic modes.

4.2 Size scaling

With the simple approximation of the SRR as a *RLC*-circuit, an inverse proportion-ality between the resonance frequency of the first mode and the size was found (see section 2.3.1). To experimentally investigate this relation, a series of SRRs with lateral dimensions (width w × height h) ranging from 120 nm × 110 nm to 480 nm × 465 nm were produced and a spectrum image was acquired for each SRR. All SRRs of the series possess approximately the same ratio of width and height. However, due to limitations in the fabrication process, not all lateral geometric parameters of the SRR can be scaled by exactly the same factor when changing the size of the SRR. Furthermore, the thick-ness of all SRRs of the series is the same (2 nm Cr and 35 nm Au). These experimental constraints should be kept in mind during the following discussion of the spectroscopic data. Previous studies on the size-scaling were restricted to the first mode [60], while the EELS experiments also allow for an investigation of the higher modes. Considering the eleven investigated SRRs, all EELS maps exhibit the same mode distribution as discussed previously (shown in fig. 4.2). Nevertheless, the corresponding resonance energies shift to higher energies if the lateral size of the SRRs is decreased. The highest recordable plas-mon energy is approximately 2.2 eV. Beyond that energy no modes can be detected, since their resonance energies overlap with interband transitions in gold [92]. For this reason, only the four lowest-order plasmonic modes can be resolved for the smaller SRRs in the series ($w < 300$ nm). The low-energy detection limit of plasmons is determined by the zero loss peak. When the resonance is below approximately 0.35 eV, the signal cannot be extracted from the ZLP. Within these limits larger SRRs show up to 6 modes, as can be seen in fig. 4.4. The first four modes are identical (in their shape) to the four modes of the SRR presented in fig. 4.2. According to the model presented previously, one would expect
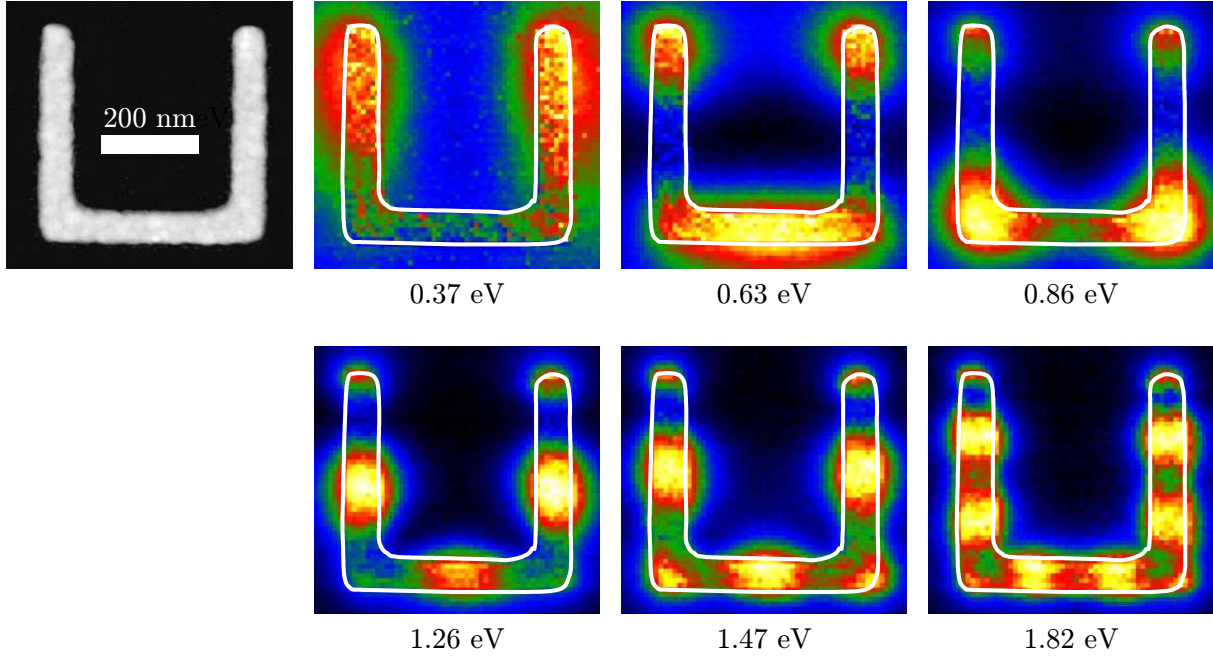
Figure 4.4: The HAADF image shows the largest investigated SRR of this study with (width × height = 480 nm × 465 nm). The six EELS maps show the six observed modes for this SRR. The first four modes show the same mode profile as the SRR previously discussed. Nevertheless, the resonance energies of the large SRR are considerably red shifted. This red shift allows for the detection of two higher order modes whose resonance energies are well below the energy of interband transitions. The mode at 1.47 eV shows seven EELS maxima, and the mode at 1.82 eV shows eight EELS maxima. The detection of modes is limited for small energies by the zero loss peak and for high energies by interband transitions.

that the fifth mode is a mode with six EELS maxima distributed along the entire wire and a minimum of the EELS signal in the middle of the bottom wire. Instead, one finds that the EELS map of the next mode at 1.47 eV better fits to the characteristics of the sixth mode, i.e., it features seven EELS maxima with one of them located in the middle of the bottom wire. Numerical calculations of the spectra reveal (not shown) that the fifth plasmonic mode of this SRR can be efficiently excited with a plane wave polarized along the bottom wire of the SRR. It is not clear why this mode is absent in the EELS experiments. Most probably this is due to the energy resolution of the microscope. The seventh plasmonic mode (1.82 eV) features eight maxima. There are also indications of at least one more mode with 2.0 eV resonance energy (not shown). However, the EELS maxima are not clearly separated in the corresponding EELS map, which prevents an unambiguous identification of the nature of this (these) mode(s).

Since all SRRs exhibit the first four plasmonic resonances, the interpretation of the size scaling experiment is restricted to these modes. Figure 4.5 summarizes the resonance energies of the modes as a function of the inverse width $1/w$ of the SRRs. For resonance
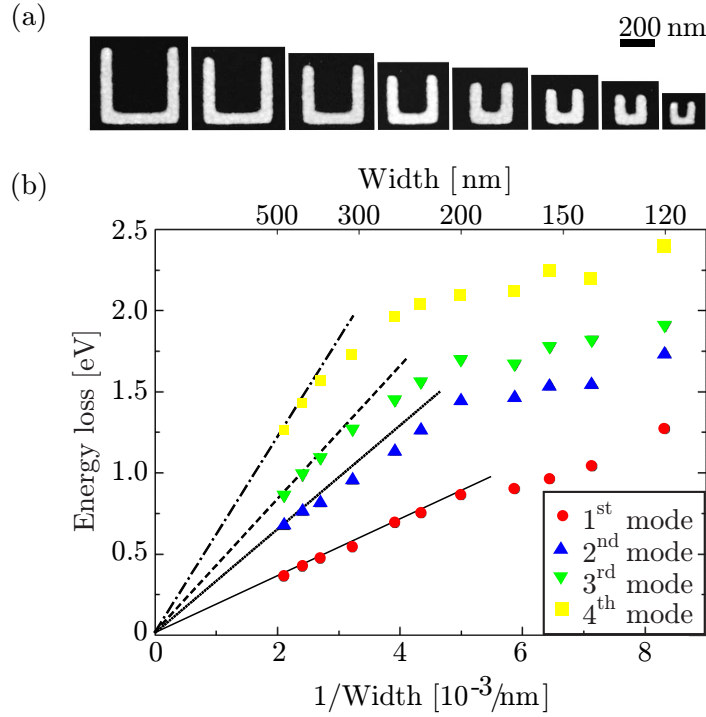
(a)

(b)

Figure 4.5: In (a), eight HAADF images of the eleven investigated SRRs are displayed. The SRRs reach from w x h = 480 nm × 465 nm to 120 nm × 110 nm. (b) The resonance energies of the first four resonance are plotted against the inverse width ($1/w$) of the SRRs. For large SRRs, the resonance energy increases linearly with decreasing width (lines are guides to the eye) as it is expected for perfect conductors. For small SRRs, the resonance energies almost saturate as is expected for metal particles in the quasistatic approximation.

frequencies much smaller than the plasma frequency of gold, the metal basically acts as a perfect conductor. Within this limit, i.e. for large SRRs, the resonance energy of the first mode is inversely proportional to the size of the SRR. This scaling law also holds to a very good approximation if only the lateral dimensions of the SRR are changed and its thickness is kept fixed [60]. Here, the largest SRR of the series is assumed to be within this size-scaling limit. Without material dispersion, the resonance energies of the first mode of all SRRs would fall on a line defined by the origin and the data point of the largest SRR (see guide to the eye in fig. 4.5 (b) for the first mode). The data points of the smaller SRRs show deviations from this straight line. This can be attributed to the influence of the frequency dependent permittivity of gold. Therefore, the evolution of the first mode is no longer in accordance with the simple scaling law for $w < 200$ nm. The resonance frequency of the first mode grows slower as the size is further decreased. This effect is even more pronounced for the other three modes. These modes only follow the scaling law for the largest SRR sizes ($w > 300$ nm). For smaller SRRs, the resonance frequencies of the second to fourth plasmonic modes start to saturate as the size of the SRRs is further decreased. The quasistatic limit would be reached when the resonance frequency becomes

independent of the size. Since a complete saturation is not observed, the considered SRRs are metal particles between the quasistatic limit and a perfect conductor. The comparison of the resonance energies also shows that the higher order modes are more susceptible to the influence of the material dispersion of gold than the first mode.

4.3   Babinet's principle

In the following section, EELS is used to investigate the near field distributions of complementary photonic meta-atoms. According to the generalized Babinet's principle (section 2.4), the modes of a metal particle and those of the corresponding complementary metallic screen are related to each other by interchanging the $\boldsymbol{E}$-field and $\boldsymbol{B}$-field distributions. Since magnetic fields cannot be detected with EELS, one is particularly interested in the connection between the B_z-component of the mode of a SRR and the E_z-component of the corresponding complementary SRR (CSRR) mode. For the test of the generalized Babinet's principle, a SRR with $w = 220$ nm and $h = 210$ nm was chosen. The lateral dimensions of the CSRR do not exactly match those of the SRR (see HAADF images in fig. 4.6) which results in a slight red shift of the resonance energies of the CSRR compared to the SRR resonances. The EELS maps of both structures can be found in figure 4.6 (a,b). The SRR shows the expected mode profiles, as already observed in the previous sections. For the CSRR, the first mode exhibits a strong EELS signal in the center of the CSRR. Recalling the predictions for the magnetic field of the SRR, one indeed expects a strong signal at this position (the oscillating ring current in the SRR induces a strong magnetic field in the center of the SRR). For the second mode of the CSRR, one finds two pronounced maxima at the outside of the two arms. The expected magnetic field of a SRR results from the two currents along the arms. The currents oscillate in phase, thus the magnetic field in the inside of the SRR vanishes and is strong at the outside, next to the arms. Thus, a good agreement is again found between the B_z-component of the SRR and the E_z-component of the CSRR. The magnetic field of the third mode results from a strong current along the bottom wire and two weak currents along the arms. In the center of the SRR, the magnetic fields due to the currents of the arms add up, and cancel out the magnetic field of the bottom wire. Therefore, the expected magnetic field distribution shows no signal in the center of the SRR, a strong maximum at the outside of the bottom wire, and two faint maxima at the outside of the two arms. These expectations are fully met by the third plasmonic mode of the CSRR.

Figure 4.6 (c) and (d) show the simulated EELS maps for a SRR and a CSRR, respectively. The dimensions of the two structures are identical and adapted from the experimentally investigated SRR. The EELS maps of both structures are in excellent agreement with the experimentally acquired data. The resonance energies of both simulated structures are identical (as expected), and show a slight red shift in comparison to the experimentally determined resonance energies. This red shift can again be attributed to deviations in
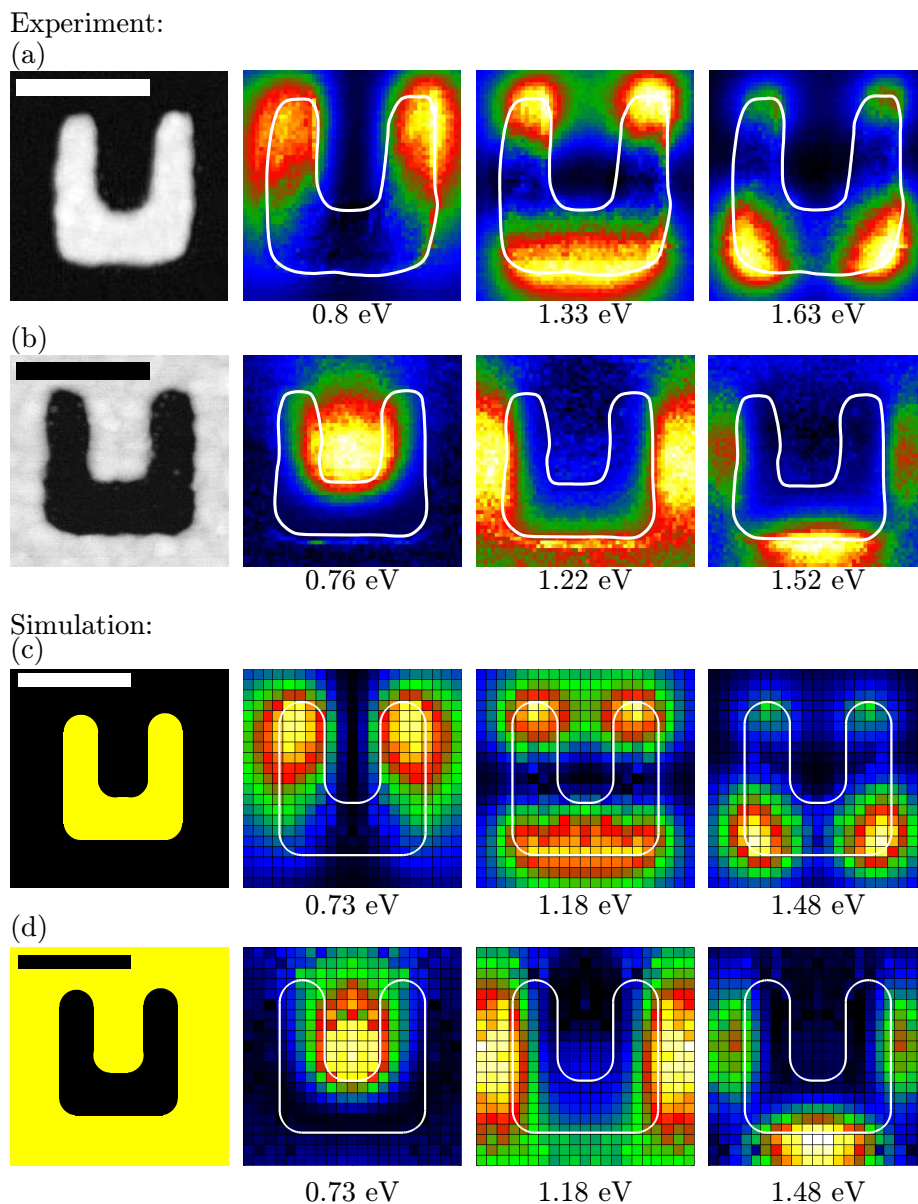
Figure 4.6: (a) HAADF image of a SRR and EELS maps of the three lowest-order SRR resonances. (b) HAADF image of the corresponding CSRR and EELS maps of the three lowest-order CSRR resonances. The resonance energy of each mode is indicated below its EELS map. The white curves show the boundaries of the SRR and the SRR-shaped aperture, respectively. (c, d) Show the simulated EELS maps. The scale bars are 200 nm. The anticipated EELS signal of the CSRR can be found by considering the magnetic field generated by the SRR mode.

shape and thickness from the experimentally investigated sample.

The comparison of the experimentally acquired mode distributions and the predicted (electric and magnetic) field distributions, clearly shows a very good agreement. Thus, Babinet's principle is indeed applicable for nanostructures with resonances in the near-infrared up to the visible frequency regime. For plasmon mapping with EELS, Babinet's principle opens up new possibilities. Since magnetic fields cannot be detected with EELS, so far the information on the $\boldsymbol{B}$-fields of metallic structures could only be found by theoretical approaches. Investigating the complementary structure changes that. Although EELS still measures electric fields, it was shown that Babinet's principle allows to deduce from the $\boldsymbol{E}$-field of the complementary structure the $\boldsymbol{B}$-field of the original structure.

Chapter 5

EELS compared to optical extinction spectra

In this chapter the excitation of plasmons is performed with electrons and with photons. The experiments are carried out on a set of four different antenna types. EEL spectra recorded at one tip of the antennas are compared to extinction cross sections from an optical experiment and possible reasons for different resonance positions are discussed. This chapter closely follows [98].

5.1 Transition from a straight wire to a SRR

The sizes of the antennas were chosen such that the resonance frequency of the respective first mode lies around $0.9\,\text{eV}$ (approximately $1.4\,\mu\text{m}$ wavelength), as the used optical setup (section 3.5) is optimized for this frequency region. The thickness of the gold structures is $35\,\text{nm}$, and no adhesion layer (chromium) was used[1]. The structures are displayed in figure 5.1 (a-d), with the corresponding EELS maps of the first plasmonic mode in figure 5.1 (e-h). Each of the four EELS maps displays two pronounced maxima at the ends of the structures. These are the expected nodes of the charge density oscillation in each antenna. While the length of the wires stays approximately the same, the shape of the maxima changes slightly between the structures. The maxima of the straight antenna are almost spherical, while the maxima of the other structures have an elliptical shape. The asymmetry of the maxima increases with decreasing distance between the maxima. This behavior can be traced back to coupling effects between the two arms of the SRR. These coupling effects also result in a quantitative difference between the energy dispersion of SRRs and that of nanoantennas [15]. Nevertheless, the assumption made in section 2.3.2 that the plasmonic modes of a SRR can be found by considering

---

[1]The sample fabrication and the optical characterization was performed by Martin Husnik.
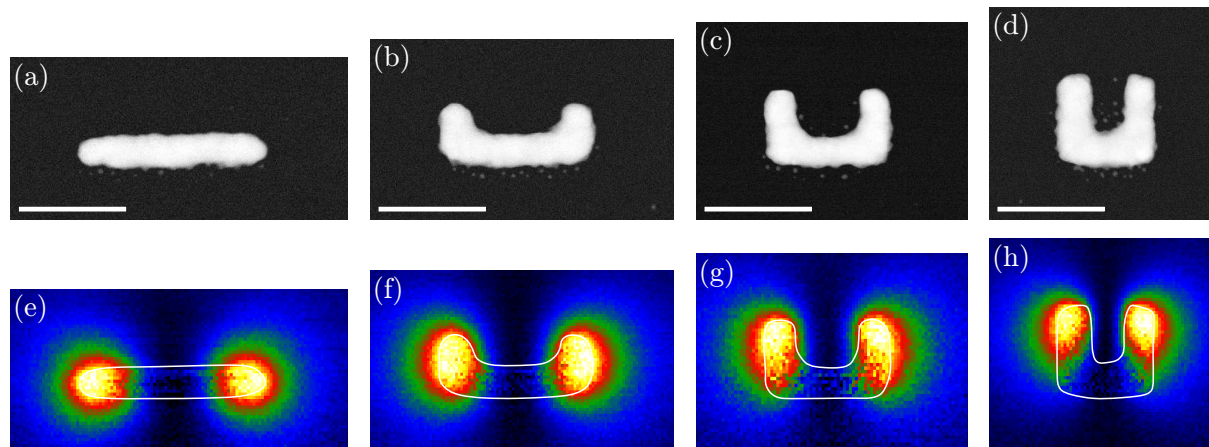
Figure 5.1: (a-d) HAADF images of four different antennas. By bending the arms upwards, the straight antenna becomes a split-ring resonator (left to right). The scale bars are 200 nm. In (e-h) the corresponding EELS maps of the first plasmonic mode are displayed. The resonance energy for each antenna is around 0.9 eV (see fig. 5.2). The white lines indicate the boundaries of the structure.

a straight antenna where the arms are bent upwards is still applicable. This also holds for the higher order plasmonic modes (not shown). For the following, the exact same antennas were investigated using optical spectroscopy.

5.2 Comparison of EEL spectra and optical spectra

5.2.1 Results of previous studies

There are a few studies which compare the excitation of plasmons by electrons with optical excitation. The outcome of these studies is ambiguous when it comes to the question of whether one can expect different or identical resonance positions using these two experiments. In 1970 EEL spectra were compared to optical spectra of silver and gold nanoparticles with diameters ranging from 10 to 100 nm [99]. It was shown that the EELS spectra are systematically blue shifted with respect to the optical extinction spectra and that the blue shift is correlated to the particle size, with a maximum shift of 800 meV for silver particles with a diameter of 80 nm. In 2008 a theoretical work on prolate gold spheroids came to the same conclusion; EEL spectra are blue shifted with respect to optical spectra [100]. The magnitude of the shift was in the range of the values stated in [99]. Another experimental work from 2011 on higher order plasmonic resonances in silver nanorods did not show a clear correlation between the EELS resonances and optical dark-field scattering spectra [101]. A more recent experimental work from 2012 showed a blue shift of the first resonance of gold nanodecahedra, with respect to optical scattering and cathodoluminescence spectra, in the order of 100 meV [102]. The results

were compared to a numerical approach based on a simple harmonic oscillator model [103, 104]. The harmonic oscillator approach shows that techniques, which probe the near field show resonances that are red shifted with respect to resonances probed in the far field. Since EELS probes the near field, the literature shows shifts of opposite sign in experiment [102] and theory [103]. There is also a theoretical work that predicts no significant shifts between EELS and optical experiments [105].

Since the literature does not give clear indication of whether to expect different resonance positions between EELS and optics, some influences are presented that might have an effect on the resonance positions.

- The two experiments are performed in different environments. While optical experiments are usually carried out in ambient conditions, EELS requires high-vacuum conditions. Samples in an ambient environment are often covered by a thin water film. Since water has a higher refractive index than air/vacuum, a small blue shift of EELS compared to optical experiments could be expected.

- Prior to the EELS measurements, the samples are cleaned in an oxygen plasma, to remove organic residues. This is necessary to reduce the deposition of carbon when the electron beam is scanned over the sample. For optical spectroscopy, this cleaning is neither necessary nor common and thus usually not performed. The removal of organic residues results in a blue shift of the resonance.

- The aforementioned carbon deposition is reduced by the plasma cleaning, but not completely eliminated. Therefore, one expects a red shift of the EELS signal with time.

- In an electron microscope, charging effects can occur when the substrate is not sufficiently conductive. Charging of the structures results in a shift of the resonance position, which is particularly strong for thin structures [106]

- The fitting procedure in the EELS experiments has an error in the range of $10 - 20 \, \mathrm{meV}$ (which corresponds to $15 - 30 \, \mathrm{nm}$ error at the considered wavelengths). The optical experiments have a far better resolution.

5.2.2   Results

Being aware of the influences EELS and plasma cleaning can have on the resonance energy, the optical experiment was performed first, followed by the EELS experiment, and as a third measurement, the optical experiment was repeated. With this sequence one can account for the changes occuring during the TEM measurement and the sample preparation. Figure 5.2 shows the optical spectra of the four antennas depicted in figure 5.1. The corresponding EEL spectra were taken at the position of the maxima found in the
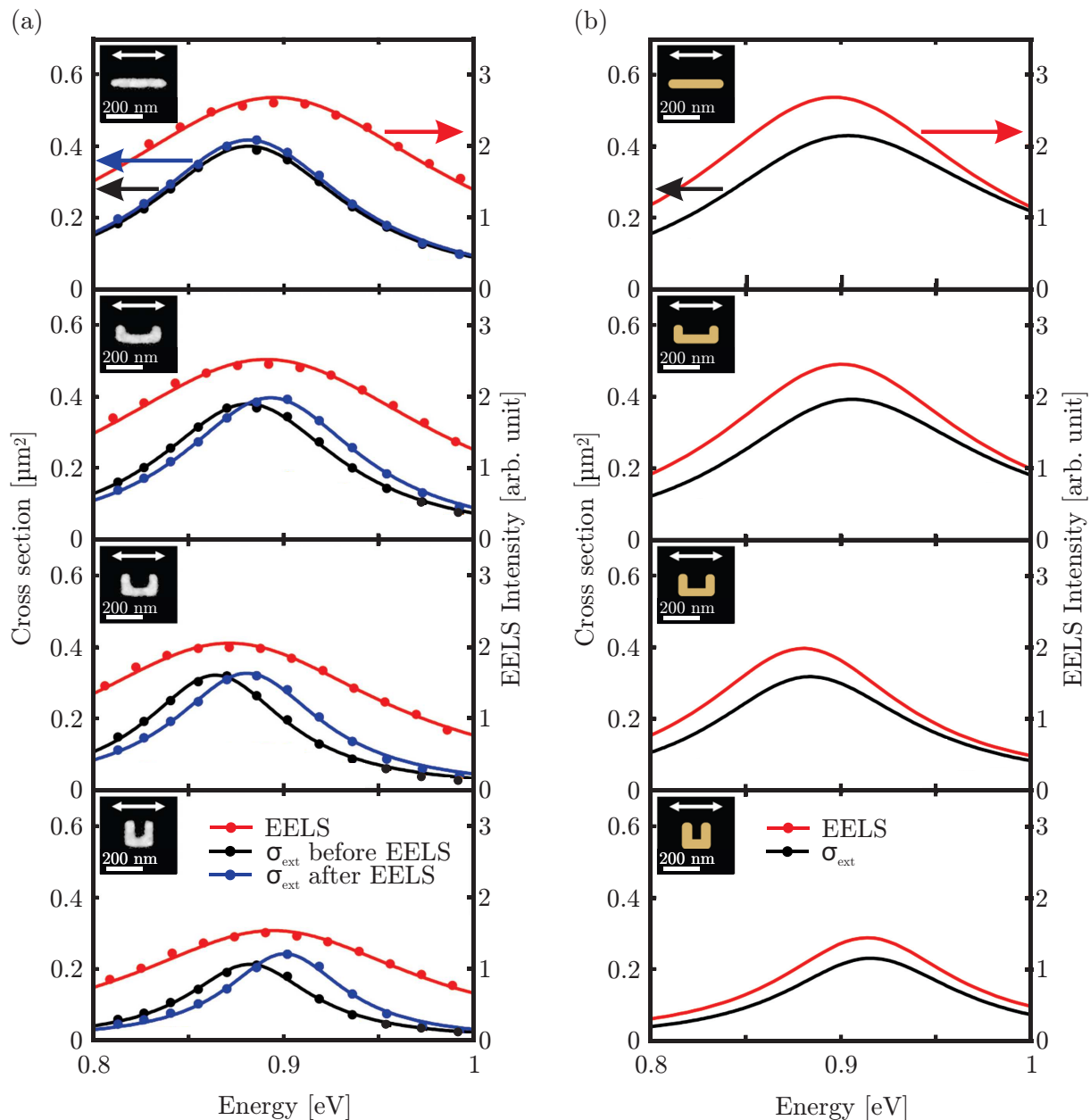
Figure 5.2: (a) Shows the experimental spectra of the four antennas depicted in the insets. The red curve corresponds to the EELS experiments and the black and blue curves to the optical extinction spectra recorded before and after the EELS measurement. (b) Shows the simulated data for EELS (red) and optical extinction spectra (black).

EELS maps shown in fig. 5.1 and are displayed in red. In general, the EEL spectra show a much broader resonance due to the finite EELS resolution. Nevertheless, the positions of the peaks can be determined and compared: The optical extinction spectra recorded prior to the EEL spectra (black curves) are red shifted with respect to the extinction spectra recorded after the EELS experiments (blue curves). This can be attributed to the plasma cleaning in between the two measurements, which is mandatory for the EELS experiments. This behavior was also shown in additional independent experiments, where optical spectra were recorded before and after plasma cleaning (not shown).

Next, the EEL spectra are compared to the optical spectra recorded after the EELS experiments. For the lower three antennas, the EEL spectra are slightly red shifted, when compared to the optical spectra. The straight antenna is an exception. Thus a clear tendency of a spectral shift cannot be found. Four additional sample series were examined which also indicate no significant spectral shift between the maxima of EELS and optical extinction after EELS. A time dependency of the EELS signal could not be measured and additional plasma cleaning steps did not lead to a shift of the resonance frequency.

In figure 5.2 (b) the corresponding numerical calculations of the extinction cross-section and the EEL spectra are depicted. The simulations cannot simulate "before" and "after" experiment/preparation. The calculated EEL spectra show a rather small red-shift with respect to the optical extinction cross-section, which is consist with [103]. The red shift is smaller than the anticipated uncertainties, discussed above. Note that the spectral width of the EEL spectra and the optical spectra are identical in the simulations (contrary to the experiments). The bottom spectrum shows a considerably smaller line width than that of the spectra above, which stems from the smaller electric dipole moment of the SRR, which in turn results in smaller radiative damping. This behavior is also observable in the optical spectra of the experiments and is discussed in [95].

Overall, the study of different antennas demonstrated how closely the mode profiles of a straight antenna are related to the mode profiles of a SRR. The comparison with the optical experiment revealed a higher spectral resolution for the optical experiments, but no significant shifts between the two spectra (within the experimental uncertainties). The simulations predict a slight red shift of the EEL spectra with respect to the optical spectra.

CHAPTER 6

COUPLING EFFECTS OF PHOTONIC STRUCTURES

The metamaterial concept is based on the ability to tailor the effective optical material parameters of an artificial medium by a proper design and fabrication of its subwavelength building blocks, the meta-atoms. A qualitative understanding of the features of a given metamaterial can often be obtained by considering the plasmonic resonances of an isolated meta-atom, as was done in the last two chapters. However, for an efficient interaction of light with a metamaterial, areas of at least a few hundreds of μm^2 are needed. In that case, the meta-atoms can no longer be treated individually, but have to be treated as an ensemble where the meta-atoms exhibit electromagnetic interactions amongst themselves.

A number of recent experimental and theoretical investigations have shown that electromagnetic interactions between the meta-atoms can have a significant impact on the properties of the metamaterial. For instance, experiments on two dimensional arrays of SRRs [107,108] and SRR-dimers [109] have demonstrated that the resonance energy and the spectral width of the first plasmonic resonance depend on the separation and relative orientation of the SRRs. The interplay of electromagnetic interactions has been found to play a crucial role in the optical properties of stereometamaterials [69] consisting of stacked layers of SRRs. Other examples of coupling effects in metamaterials are the formation of magnetoinductive waves [110], Fano resonances [111], a non-trivial dependence of the second harmonic generation efficiency of metamaterials on the lattice period [112] and the observation of plasmon-induced transparency [113]. Furthermore, electromagnetic interaction effects between metallic nanostructures have also been theoretically [114] and experimentally [115–117] investigated in the context of plasmonic particles.

Most studies on coupling effects in metamaterials rely on optical far field methods, e.g., linear transmittance or reflectance spectroscopy. However, a great wealth of information regarding the electromagnetic interaction is encoded in the near field, which is not accessible to these experiments. Furthermore, these methods are only sensitive to modes of the metamaterials that exhibit a non-vanishing electric dipole moment (bright-modes) (see

section 2.5). In contrast, modes with a vanishing electric dipole moment (dark modes) are not directly accessible in far field experiments. However, these dark modes play an important role, e.g., in the coupling of quantum emitters to metallic nanostructures, in the context of optical antennas [40] or the spaser [118].

In this chapter STEM-EELS is used to study collective near field phenomena in the course of the transition from an isolated meta-atom to a photonic metamaterial. This chapter closely follows [97].

6.1 Expectations

In section 2.3.1 it was shown that the first mode of the SRR has a magnetic dipole moment perpendicular to the plane the SRR lies in and an electric dipole moment pointing from one arm of the SRR to the other. The coupling behavior of dipoles was explained in section 2.5, and it was shown that the number of participating coupling elements determines the number of different eigenmodes of a system. For small ensembles containing only a few SRRs, the anticipated electromagnetic interaction between the SRRs results in plasmon hybridization [114], i.e., the first plasmonic mode of a single SRR evolves into a set of discrete optical bright and dark modes (see fig. 6.1). The number of participating SRRs thereby equals the number of modes. Whether a mode of the ensemble is bright or dark depends on how the electric dipoles of the different SRRs couple and how strong the resulting net dipole moment is. For example, the most obvious bright mode corresponds to the case where all of the electric dipoles point in the same direction.

By adding more and more SRRs to the ensemble, the energetic distance between the discrete modes decreases and the line width of each mode comes into play. When the line width is larger than the energetic distance to the next mode, single modes can no longer be distinguished. Therefore one expects, for large SRR arrays with ten thousands of meta-atoms, the formation of a quasi-continuum of modes in analogy to the tight-binding model of solid state physics (see fig. 6.1) [119].
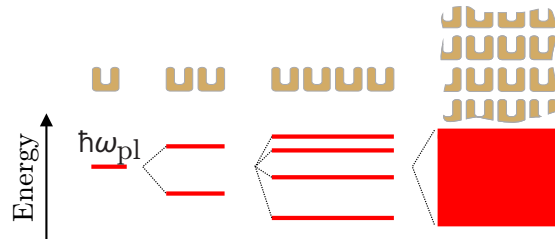

Figure 6.1: Plasmon hybridization model: The number of plasmonic modes increases linearly with the number of SRRs. In the case of an infinite array of SRRs the coupled modes form a continuum.

6.2   SRR dimers

6.2.1   Side-by-side configuration

The most intuitive way to understand coupling effects in metamaterials is to examine a dimer of SRRs, i.e., two SRRs that are arranged in the side-by-side configuration (see inset of fig 6.2). By considering the two electric dipole moments of the dimer (one for each SRR, pointing from one arm to the other), this arrangement resembles the case of two coupling dipoles, which was discussed in section 2.5. Thus, one expects to find a mode splitting of the first resonance of the SRR dimer into two modes; a higher energy mode and a lower energy mode. To compare the energetic shifts of the resonances of the SRR dimer, an isolated SRR with the same dimensions as one of the dimer SRRs is investigated as well.
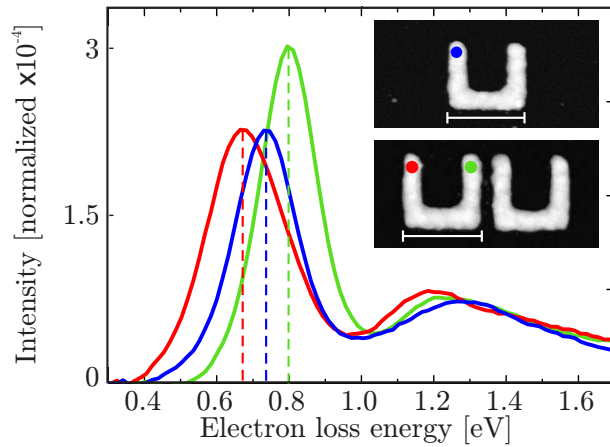

Figure 6.2: EEL spectra of an isolated SRR (blue) and a SRR dimer (red, green). The dashed lines indicate the spectral positions of the resonance peaks. Each spectrum is normalized to its total number of counts. A quantitative difference in height can be connected to a different excitation probability. In the insets, the corresponding electron beam locations are marked in the same color as the respective spectra. The size of the SRRs are (width × height × thickness) = 200 nm × 200 nm × (2 + 35) nm (Cr + Au). The scale bars are 200 nm.

The EEL spectrum recorded at one end of the isolated SRR is shown in fig. 6.2 (blue). The two maxima at 0.75 eV and 1.3 eV correspond to the first and the second order plasmonic mode, respectively. Since most optical phenomena (especially the induced magnetic dipole) originate from the first mode, the following discussion will concentrate on this mode. The corresponding experimental EELS map of the isolated SRR is depicted in fig. 6.3 (a). In accordance with previous EELS experiments, one finds pronounced maxima at the ends of the SRR wire. This behavior is also reproduced by the DGTD calculations (see fig. 6.3 (b)). The slightly smaller value of the calculated resonance energy (0.69 eV) can be attributed to deviations of the fabricated SRR from the ideal shape.
 Figure 6.2 also shows two spectra from the SRR dimer; one recorded at the inner arm and one recorded at the outer arm of the left SRR. The first resonance of the spectra clearly shows shifts in the peak position, when compared to the resonance of an isolated SRR. The corresponding EELS maps at the two resonance energies 0.69 eV and 0.8 eV
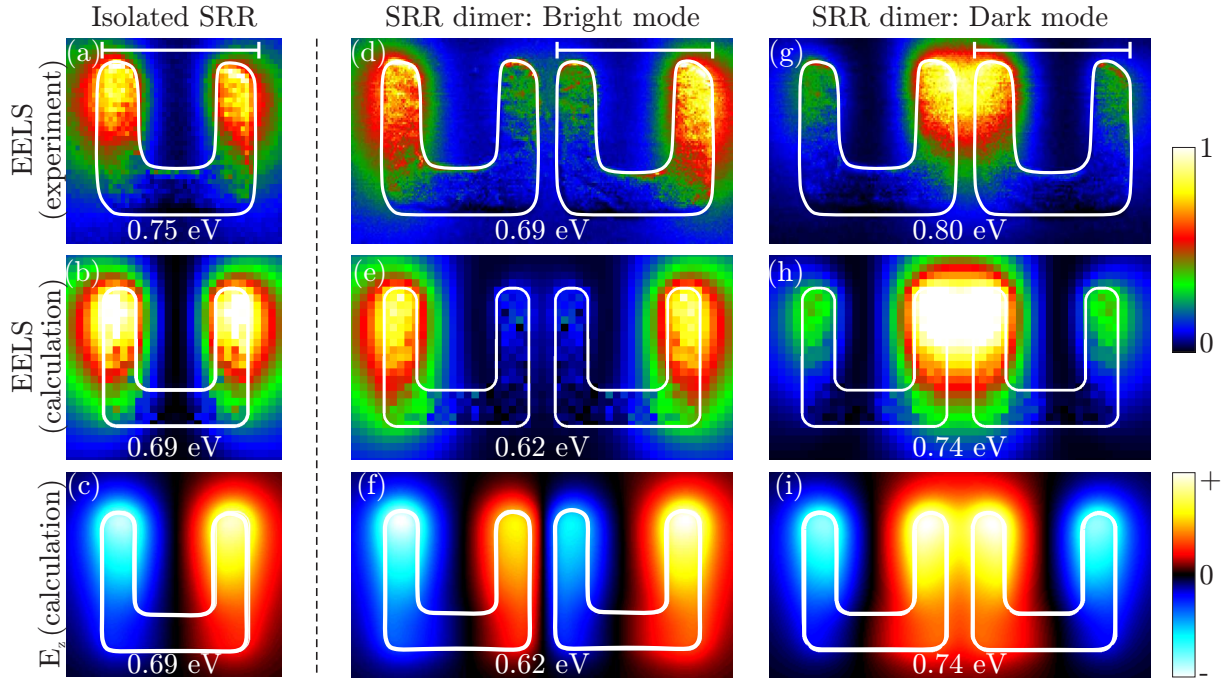
Figure 6.3: Single SRR and SRR dimer (side-by-side configuration). (a) The experimental EELS distribution, (b) the calculated EELS distribution, and (c) a snapshot of the calculated E_z distribution of an isolated SRR are presented in the left column. The corresponding data of the optical bright (d,e,f) and dark mode (g,h,i) of the SRR dimer are depicted in the center and right column, respectively. The white lines indicate the boundaries of the SRRs. The resonances energy is stated in each case. The scale bars are 200 nm.

can be found in fig. 6.3 (d) and (g), respectively. The simulated EELS maps, as well as the phase information can also be found in fig. 6.3. The results show clear evidence that coupling of the two SRRs lifts the energetic degeneracy (see fig. 6.1) and leads to the formation of two new eigenmodes with distinct EELS signal distributions. Both, the experimental data and the numerical calculations show that the low-energy mode exhibits strong EELS signals at the outer arms of the dimer. In contrast, the maximum of the EELS signal is found in the middle of the dimer for the high energy mode (see fig. 6.3 (g) and (h)). The energetic splitting of the two modes, their optical character, and the positions of the maxima in the corresponding EELS maps can be qualitatively understood in terms of the plasmon hybridization model: The in-phase coupling of the individual plasmonic modes (see fig. 6.3 (f)) yields an optical bright mode whose resonance energy is lowered compared to an isolated SRR [109]. The consequences for the EELS map are the following: Between the two SRRs, the electric field is mainly oriented perpendicular to the trajectory of the electron beam. In section 2.2.5 it was show that the energy loss probability vanishes in that case. Thus, only a small EELS signal can be detected at the inner arms of the dimer. In contrast, the anti-phase coupling of the two individual plasmonic modes results in an optical dark mode with increased resonance

energy. It exhibits a strong E_z component (see fig. 6.3 (i)) and hence a strong EELS signal in the middle of the dimer. Note that the optical dark mode has not been observed in previous optical experiments.

Electric vs. magnetic dipoles
The in phase coupling of the side-by-side dimer results in an optical bright mode, where the two electric dipole moments are aligned in a row and point in the same direction. The interaction of the electric dipoles leads to the low energy mode. At the same time, the magnetic dipoles are aligned parallel to each other and point in the same direction (see fig. 6.4 (a)), which leads to the high energy mode. Since the experiments (and simulations) show that the in-phase coupling of the SRRs results in the low energy mode, the interaction of the electric dipoles has a bigger influence than the interaction of the magnetic dipoles. Analog considerations can be made for the out-of-phase coupling, where the electric dipole coupling predicts a high energy mode, and the magnetic coupling predicts a low energy mode. In that case, the high energy mode is observed, which again implies the dominance of the electric dipoles. Therefore, further considerations will concentrate on the electric dipoles. Nevertheless, the magnetic dipoles might contribute to the coupling, but with a significantly smaller impact.
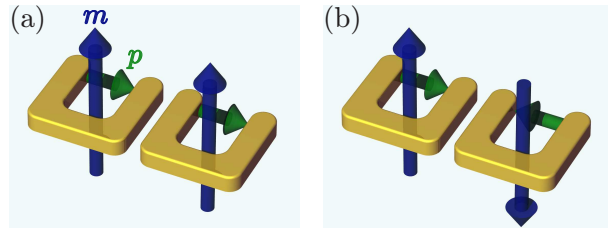

Figure 6.4: The electric and magnetic dipoles of the in-phase (a) and out-of-phase (b) coupling. The electric and magnetic dipoles predict opposite behaviors for the mode splitting. The experimental (and simulated) results suggest that the electric dipoles play the dominant role in the interaction.

6.2.2   On-top configuration

In a second step, the on-top dimer configuration is considered. In the model of coupling dipoles (presented in section 2.5), this case corresponds to a negative coupling constant, i.e., one expects a symmetric high energy mode and an anti-symmetric low energy mode. By considering single spectra from the on-top dimer configuration (see fig. 6.5 (b)), the formation of two new eigenmodes can indeed be observed. The spectra acquired at the top and bottom SRR show their first resonance at 0.76 eV and 0.67 eV, respectively. The corresponding EELS maps are displayed in figure 6.5 (c) and (f). The simulated EELS maps and the E_z distribution can be found in the same figure.

Again, the agreement between experiment and simulations is excellent. In contrast to the side-by-side dimer configuration, the low-energy mode is an optical dark mode which results from an anti-phase coupling of the two individual plasmonic modes (see fig. 6.5 (e)).
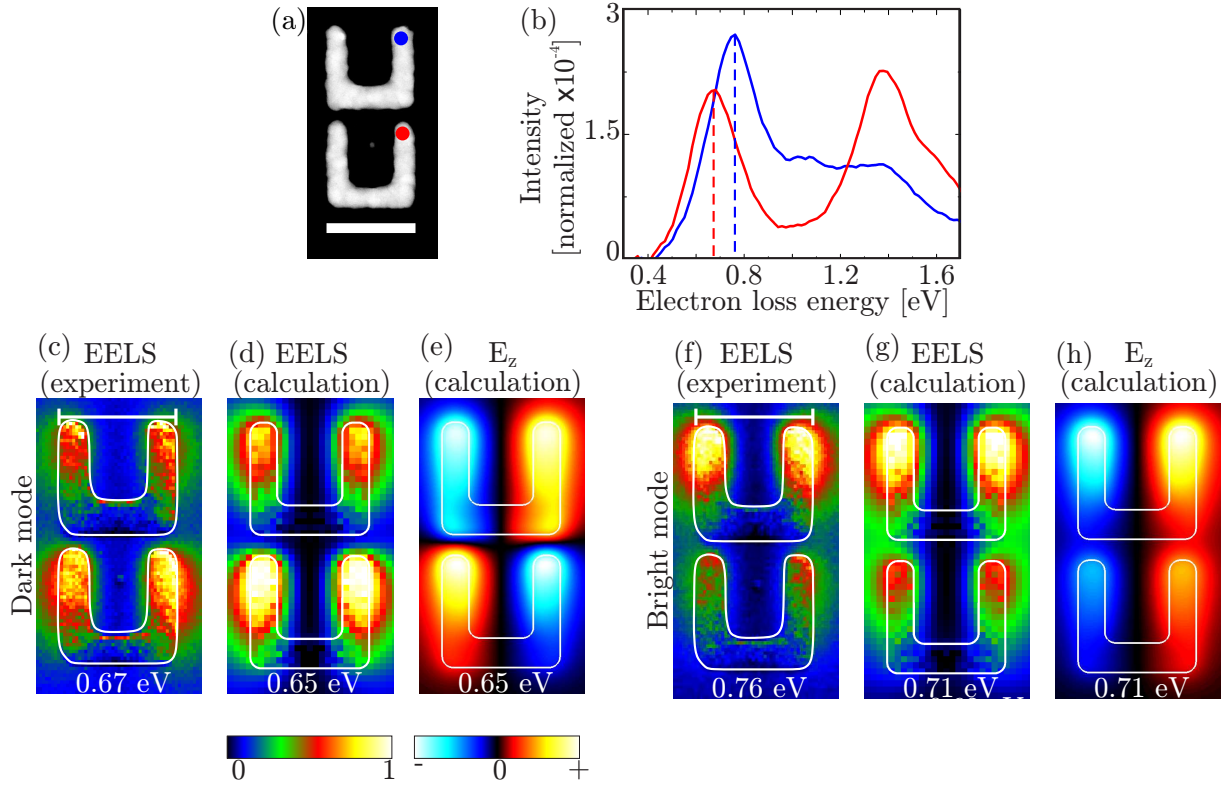
Figure 6.5: SRR dimer (on-top configuration). (a) Dark field image of two SRRs in the on-top configuration. The scale bar is 200 nm. (b) Two EEL spectra recorded at the positions color-coded in (a). The maxima of the red and blue curve correspond to the resonance energy of the optical dark and bright mode, respectively. (c) Experimental EELS distribution, (d) calculated EELS distribution, and (e) snapshot of the E_z distribution of the optical dark mode. (f-h): Corresponding data of the optical bright mode. The scale bars are 200 nm.

It has strong EELS maxima at the ends of the bottom SRR (see fig. 6.5 (c,d)). The in-phase coupling of the electric dipoles (see fig. 6.5 (h)) evokes an optical bright mode whose resonance energy is raised with respect to an isolated SRR and which exhibits strong EELS maxima at the ends of the top SRR (see fig. 6.5 (f,g)).

For two coupling dipoles in the side-by-side or on-top configuration, the predictions made in section 2.5 could be confirmed. By considering the dominant electric dipoles, the in-phase coupling of two dipoles in the side-by-side configuration lead to a low energy mode, while the in-phase oscillation of two dipoles in the on-top configuration lead to a high energy mode. The predictions of the simple dipole coupling model therefore hold in case of two interacting SRRs. The only deviation lies in the quantitative energy splitting: While in the side-by-side configuration the energy difference between the in-phase and out-of-phase mode is 0.11 eV, it is only 0.09 eV in the on-top configuration. This difference can be traced back to the distance between the electric dipoles. In the side-by-side configuration the two dipoles are separated by approximately the distance between the

two SRRs, while they are separated by approximately the whole height of a SRR in the on-top configuration. The influence of the separation on the energy splitting is shown in figure 6.6. As a measure of the separation, the gap size between the two SRRs is consid-
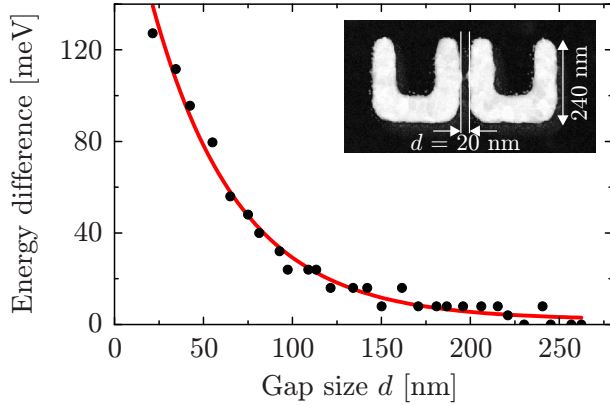

Figure 6.6: The energy difference between the in-phase and out-of-phase mode as a function of the gap size d between the two SRRs. The red line is an exponential fit that serves as a guide to the eye. For this study, SRRs with slightly different dimensions were chosen, (width×hight×thickness) $= 240\,\mathrm{nm} \times 240\,\mathrm{nm} \times (25+2)\,\mathrm{nm}$ (Au + Cr).

ered. The graph clearly shows a decrease in the energy difference of the two modes with an increasing gap size. When the gap size reaches approximately 250 nm, the two modes can no longer be separated and the SRRs can be considered as isolated meta-atoms.

6.3 Multiple SRRs

According to the plasmon hybridization model, one expects that the number of eigenmodes increases linearly with the number of SRRs in the ensemble. As an example, the case of four SRRs arranged in the side-by-side configuration (see fig. 6.7 (a)) is considered, where the formation of four different eigenmodes is anticipated. In the calculated EELS signals one can indeed identify four different modes (see fig. 6.7 (f-i)) with the corresponding calculated E_z distributions as depicted in fig. 6.7 (j-m), respectively. These four modes are equivalent to the modes identified with the coupling model of dipoles. By considering the electric dipoles, the four modes correspond to the previously found (see section 2.5) dipole orientations[1]: $(++++)$, $(--++)$, $(+--+)$, and $(-+-+)$.

Contrary to the calculations, the experimental EELS data only reveal three modes (see fig. 6.7 (c-e)). This inconsistency between experiment and theory is a result of the spectral resolution of the experimental setup and the spectral overlap of the eigenmodes. A comparison with the calculated EELS maps suggests that the experimental EELS distribution in fig. 6.7 (e) results from the superposition of the EELS signals of the two highest energy modes (fig. 6.7 (h,i)). Experimental EEL spectra recorded at characteristic positions of the four SRRs are depicted in fig. 6.7 (b).

---

[1]The dipoles are oriented parallel to the bottom wires, and point either to the right $(+)$ or left $(-)$.

(a)

(b)

EELS (experiment)   EELS (calculation) E_z (calculation)

(c) 0.56 eV (0.69 eV)   (f) 0.55 eV   (j) 0.55 eV

(d) 0.65 eV (0.73 eV)   (g) 0.66 eV   (k) 0.66 eV

(e) 0.82 eV (0.77 eV)   (h) 0.73 eV   (l) 0.73 eV
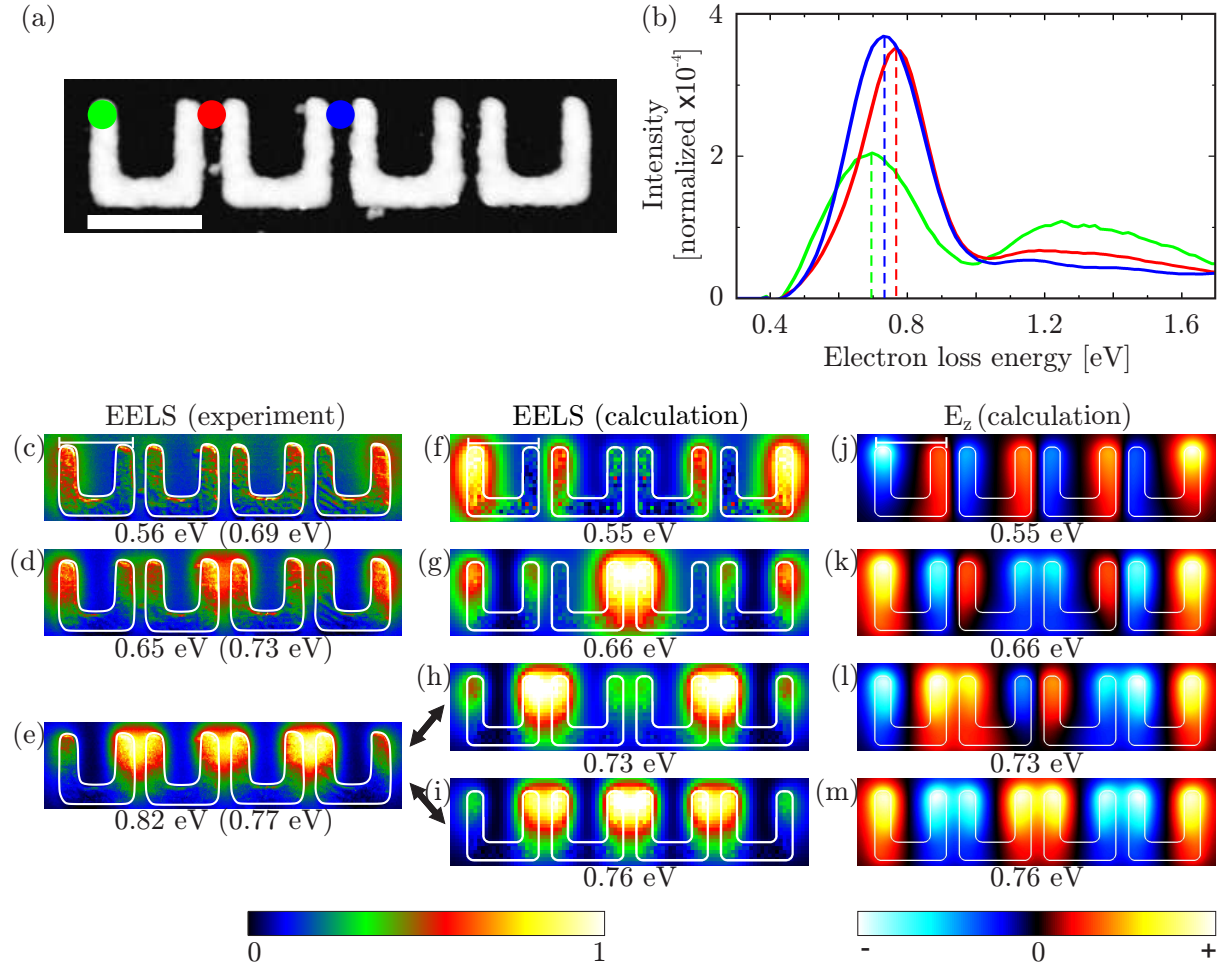
(i) 0.76 eV   (m) 0.76 eV

Figure 6.7: Ensemble of four SRRs. (a) Dark field image of 4 SRRs in the side-by-side configuration. The scale bar is 200 nm. (b) The three EEL spectra are recorded at the positions color-coded in (a). The maxima of the three curves correspond to the resonance energies of the modes depicted in (c-e).The left, center, and right column depict the experimental EELS distributions, the calculated EELS distributions, and snapshots of the calculated E_z distributions, respectively. The scale bars are 200 nm. Note that the experimental EELS distributions in (c) and (d) do not correspond to the respective resonance energies of the modes, but to slightly smaller electron loss energies. Through this shift, the spectral overlap with the higher energy modes is reduced and thus a better visual separation of the modes is obtained. The first stated value corresponds to the displayed energy, while the second value in brackets corresponds to the resonance energy obtained from the spectra.

For typical two-dimensional metamaterials containing ten thousands of SRRs (see fig. 6.8 (a)), one anticipates that coupling results in the formation of a quasi-continuum of modes, where the spectral separation of neighboring modes is much smaller than their spectral widths. In optical far field experiments, this quasi-continuum of modes gives rise to a single plasmonic resonance whose spectral width depends on the properties of
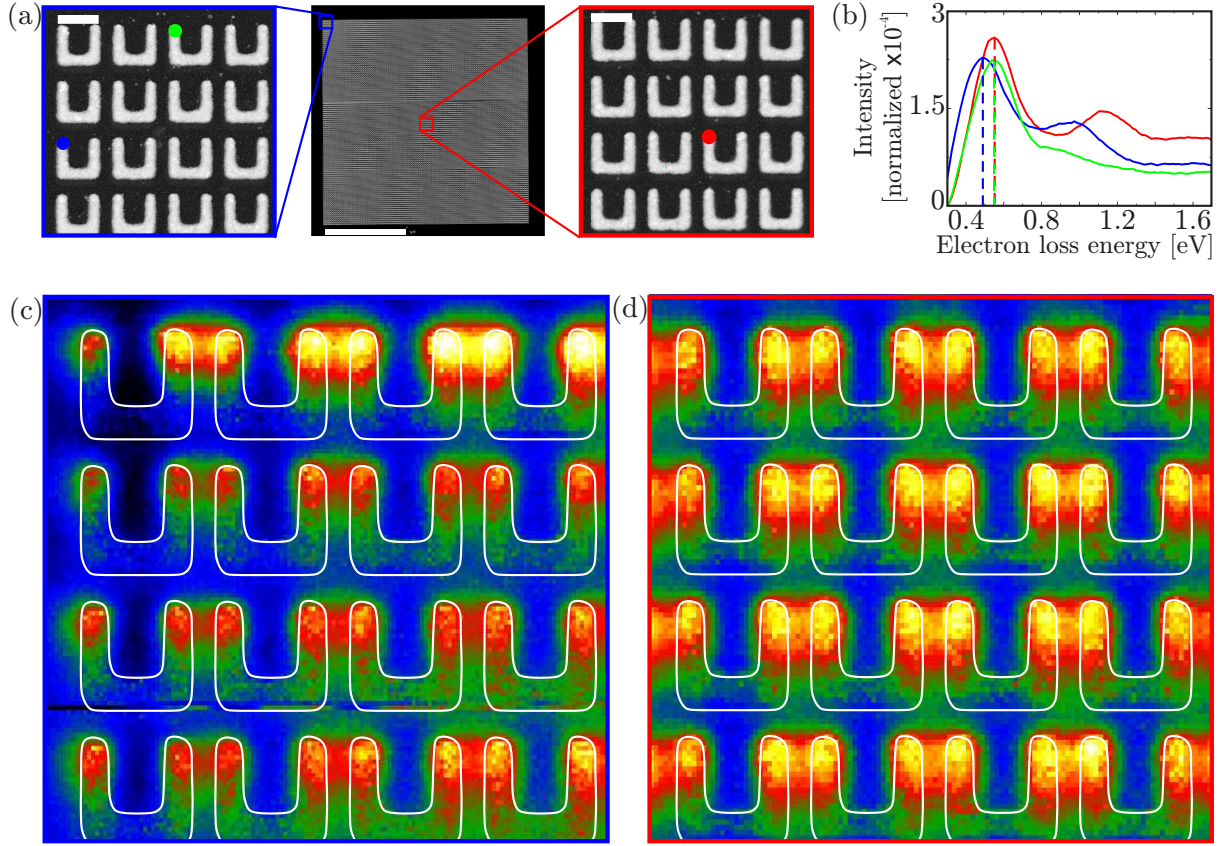
Figure 6.8: (a) Dark field images of a $100{\times}100$ SRR array. Center: over-view (scale bar is $10\,\mu m$); left hand side: close-up of the upper left corner of the array; right hand side: close-up of the interior. The scale bars are 200 nm. (b) Three EEL spectra recorded at the positions color-coded in (a). (c) EELS signal distribution of the upper left corner. (d) EELS signal distribution of the interior. The two EELS signal distributions are displayed at the same energy ($0.55\,eV$).

both the individual SRRs and their interaction [107, 108]. In the interior of a periodic array, each SRR "sees" the same environment. Hence, one expects to find for a given electron energy loss the same EELS signal distribution within each unit cell, which arises from the incoherent superposition of many modes. Figure 6.8 (d) exemplifies the EELS map recorded in the center of the array at an electron energy loss corresponding to the peak of the plasmonic resonance ($0.55\,eV$). As expected, the signal distributions for all unit cells are identical within the experimental accuracy: The EELS signal is always concentrated between two neighboring SRRs of a row. However, at the boundary of the SRR array the different sites are not equivalent and one anticipates in analogy to electronic surface states [119] the formation of photonic edge modes. For example, a SRR at the edge of the array has only three nearest neighbors instead of four, as in the interior of the metamaterial. As a consequence, the electromagnetic near field distribution is different. Figure 6.8 (c) depicts the EELS signal distribution for a corner of the array

at the same electron energy loss as in the previous case. Here, clear evidence for the anticipated photonic edge modes can be found. One can observe particularly strong EELS signals at the ends of the SRRs in the top row of the array. In contrast, the EELS intensity is considerably reduced for the SRRs on the outer left column of the array. The corresponding edge mode at the outer left column has a resonance energy, which is red shifted by 65 meV (not shown). Experimental EEL spectra recorded in the interior and at the boundaries of the array can be found in fig. 6.8 (b).

Compared to the spectrum of a single SRR, the first resonance of the SRR array (see red curve in fig. 6.8 (b)) is slightly broadened. This spectral broadening is an effect of the coupling of the SRRs in the array. Spectral broadening as a result of the interaction of the elements of an SRR array has also been observed in optical experiments [107–109]. Due to the limited spectral resolution of the microscope and the slightly different sizes of the isolated SRR and the SRRs in the array, a quantitative analysis of the spectral width was not performed.

6.4   Further considerations

So far, the SRRs in the ensembles all had the same orientation (the opening of the SRRs always faced in the same direction). A variety of different samples were produced to investigate facing, back-to-back, or arbitrarily rotated SRR ensembles. The mode profiles and resonances of these configurations can, in the simple cases of two interacting SRRs with parallel electric dipole moments, still be explained with the dipole coupling model. However, for more complex situations, where the electric dipoles of the SRRs are not parallel to each other and more than two SRRs are considered, the anticipated mode profile is not found quickly (which does not mean that the dipole model is not applicable). An EELS map of a SRR array, where one of the SRRs was rotated by 90°, is depicted in figure 6.9 (b). The SRRs in the array, which are not nearest neighbor with the rotated SRR, show the expected behavior already observed for the previous (symmetric) array. However, the nearest neighbor SRRs and the rotated SRR show deviations from this result. For example the SRRs on the left and right side of the rotated SRR show an EELS maximum only on one of their arms.

Furthermore, only the first plasmonic mode was considered in the coupling experiments so far. As is known from the previous chapters, there are multiple higher order modes, which of course also exhibit electric and magnetic dipole moments and thus also show electromagnetic interactions. The interest of these modes is limited, since most optical effects rely only on the first mode. As an example of a higher order mode coupling, the second mode of the on-top dimer configuration is presented in figure 6.9 (d,e). The effective electric dipole moment of the second resonance points from the tip of the arms to the bottom wire of the SRR, i.e., in the direction, the two SRRs are arranged. This leads to a coupling behavior, similar to the coupling behavior observed for the first mode, in the
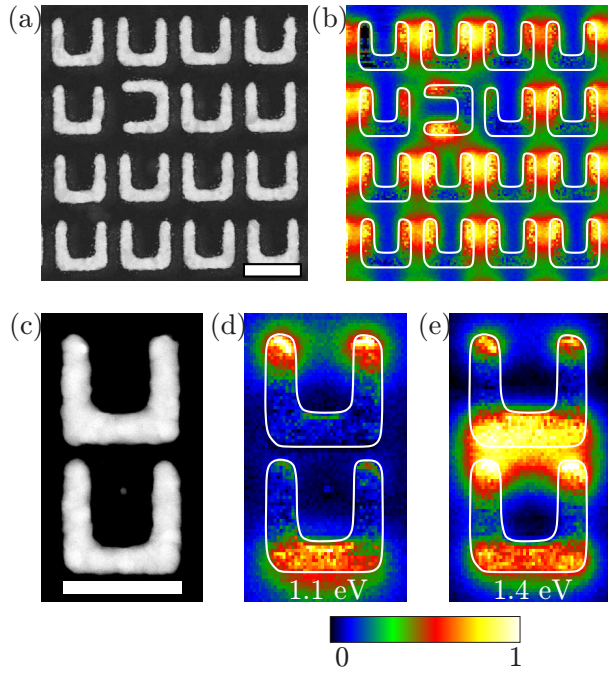
Figure 6.9: (a) Dark field image of an SRR array where a lattice defect was intentionally introduced by rotating one SRR by 90°. (b) EELS map of (a) at the resonance energy of the array. The lattice defect influences only the SRRs in its direct environment. (c) Dark field image of the on-top dimer, already discussed in section 6.2.2. Images (d) and (e) show the EELS maps of the in-phase and out-of-phase coupling of the second order mode.

side-by-side configuration. For the gap region, one obtains the following field distribution. The in-phase oscillation of the SRRs results in field lines which are perpendicular to the electron trajectory. Thus there is only a weak EELS signal for this mode (see fig. 6.9 (d). However, the out-of-phase oscillation has a strong E_z component in the gap between the SRRs and thus has an EELS maximum at this position (see fig. 6.9 (e)). The other higher order modes also show coupling effects (not shown).

Chapter 7

Angular-resolved EELS

In the last chapter it was shown that certain electric field configurations lead to a vanishing energy loss probability for normal incident electrons. This chapter addresses such field configurations by changing the incident angle of the electron beam. A tilt of the sample allows for the detection of different electric field components of the plasmonic modes. Electron energy loss spectra recorded under oblique incidence can therefore feature plasmonic resonances that are not observable under normal incidence. This chapter closely follows [120].

7.1 Expectations

For planar metallic nanostructures, charge densities usually appear as pronounced maxima in the corresponding EEL maps. Nevertheless, in some configurations of nanoparticles, there are 'hot spots' in the gaps between plasmonic particles, as in the case of the in-phase oscillation mode of a plasmonic dimer, which do not give rise to strong EELS signals for normal incidence of the electron beam [12, 13, 27, 51]. This observation can be easily explained by taking the influence of the excitation geometry on the EELS signal into account. In section 2.2.5 it was shown that the loss probability $\Gamma_{\text{EELS}}(\omega)$ is given by (equation 2.35):

$$\Gamma\left(\omega\right) = \frac{\text{e}}{\pi\hbar\omega} \int_{\text{t}=-\infty}^{\infty} dt \text{Re}\left[\text{e}^{-\imath\omega t} \boldsymbol{v} \cdot \boldsymbol{E}_{\text{ind}}\left(\boldsymbol{r}_{\text{e}}\left(t\right), \omega\right)\right], \tag{7.1}$$

where $\boldsymbol{v}$ is the velocity of the electron, $\boldsymbol{r}_{\text{e}}\left(t\right)$ is its trajectory, and $\boldsymbol{E}_{\text{ind}}\left(\boldsymbol{r}_{\text{e}}\left(t\right), \omega\right)$ is the induced electric field. Inspection of equation 7.1 immediately reveals that only the component of $\boldsymbol{E}_{\text{ind}}\left(\boldsymbol{r}_{\text{e}}\left(t\right), \omega\right)$ parallel to $\boldsymbol{v}$, and thus parallel to the electron trajectory is relevant for the loss probability.
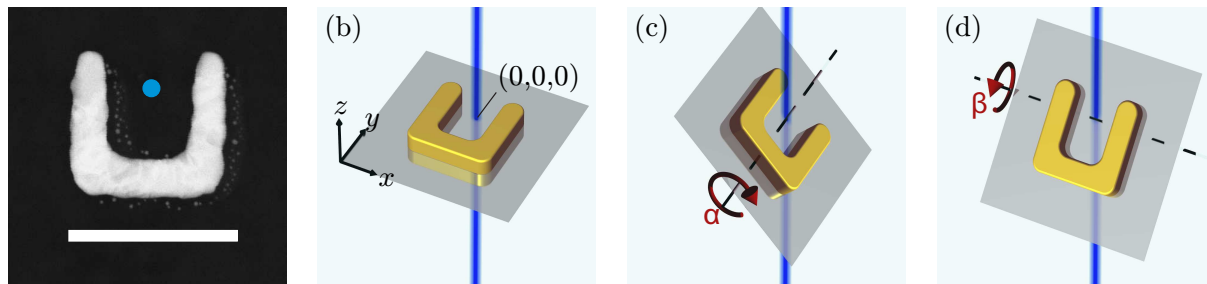
Figure 7.1: (a) Dark-field image of a split-ring resonator. The blue dot marks the position of the electron beam. The length of the scale bar is 200 nm. (b) Schematic view of the SRR and the electron beam (blue line) for normal incidence. In (c), the sample is rotated around the y-axis by $\alpha = 46°$ and in (d), the sample is rotated around the x-axis by $\beta = 46°$.

To demonstrate this, a split-ring resonator can serve as a model system (see fig. 7.1 (a)). Its first plasmonic mode exhibits a hot spot in the region between the two tips (see fig. 7.2). There, the field distribution closely resembles the field distribution of the in-phase mode in the gap of a plasmonic dimer. However, the spectral overlap between the first plasmonic mode and the second plasmonic mode of an isolated SRR is significantly smaller than the spectral overlap of the in-phase and out-of-phase mode of a dimer. This is a distinct advantage of the SRR compared to the plasmonic dimer for the intended experiments. EELS maps of the first SRR mode recorded under normal incidence feature very small signals in the region of the hot spot [15, 66, 97]. By performing oblique incidence EELS, one can probe different electric field components of the plasmonic mode with the electron beam and thus "cure the blindness of EELS to hot spots".

In a recent theoretical analysis, it was shown that a set of oblique incidence EELS maps can in principle even be used to fully reconstruct the three-dimensional plasmonic near field [121]. Corresponding experiments were presented in [122]. A quantitative reconstruction of the plasmonic near field is not performed, since the proposed scheme relies on the quasistatic approximation which is not applicable for the SRR used in this study (see section 4.2) [60].

The utilized SRR is depicted in figure 7.1 (a) and is slightly thinner than the previously investigated structures ((2 + 25) nm = Cr + Au). This was done due to the increased interaction length in the case of oblique penetration. These experiments were performed at Harvard University and the acceleration voltage was set to 80 kV (the simulations were also performed with 80 kV). To increase the signal-to-noise ratio, 40 individual spectra were recorded at each position and the zero-loss-peak of each spectrum was centered at 0 eV before averaging.
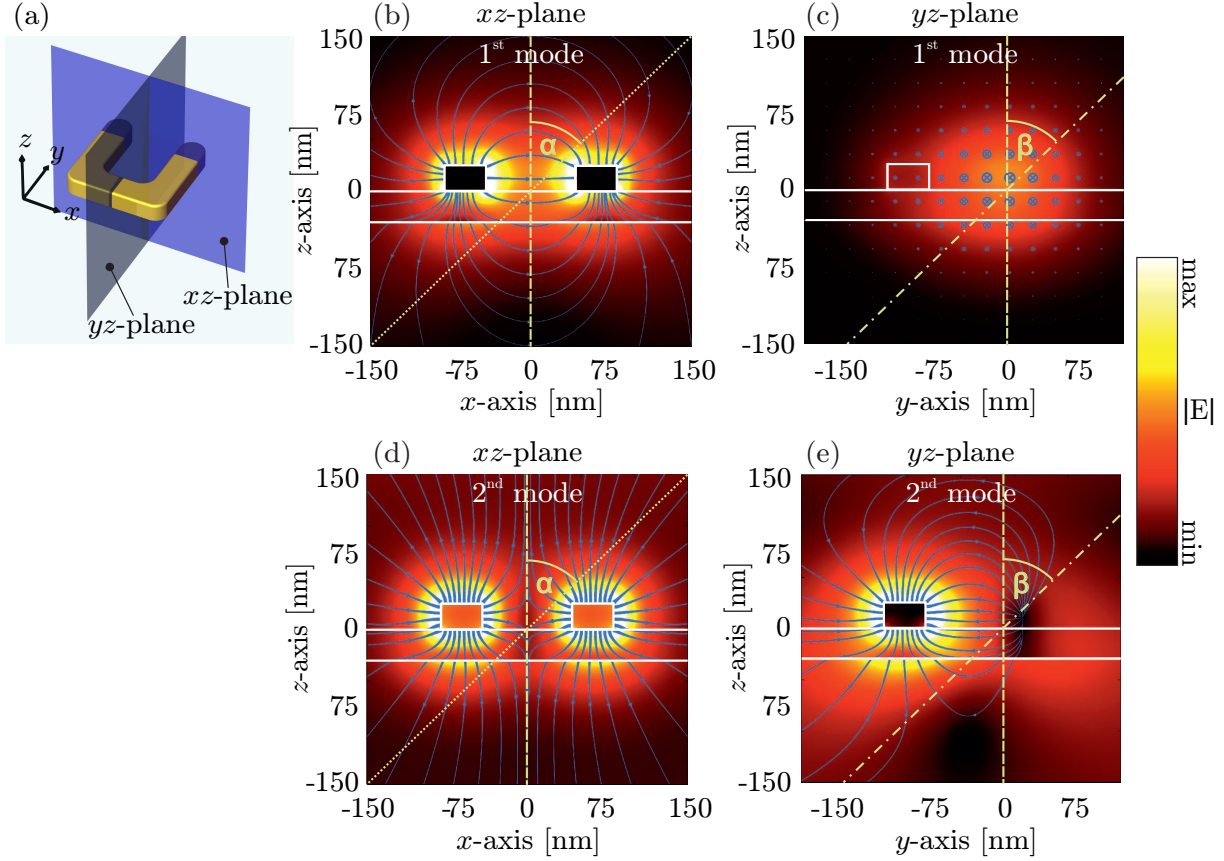
Figure 7.2: Calculated near field distribution of the first and second order mode of a split-ring resonator. (a) Shows the two planes relevant for the experiments. (b) Depicts the electric field of the first mode in the xz-plane at $y = 0$; the blue lines indicate the electric field lines and the color represents the modulus of the electric field $|\mathbf{E}|$. For $x = 0$, all field lines are oriented horizontally and point in one direction. (c) Shows the electric field within the yz-plane ($x = 0$) of the first mode. The electric field lines are perpendicular to this plane as indicated by blue crosses. Figures (d) and (e) show the electric field distribution of the second order mode in the xz-plane and yz-plane, respectively. The solid white lines are the boundaries of the membrane and the SRR. The dashed, the dotted and the dash-dotted line represent the electron trajectories for $\alpha = \beta = 0°$, $\alpha = 46°$, and $\beta = 46°$, respectively.

7.2   Tilt around x-axis

In the first step, an electron energy loss spectrum was recorded under normal incidence at one tip of the SRR (not shown). The resonance energies of the first and the second plasmonic mode of the SRR derived from this spectrum were 0.69 eV and 1.19 eV, respectively. Next, the sample was rotated from $\alpha = 0°$ to $\alpha = 46°$ in steps of 1° around the y-axis (see fig. 7.1 (c)). Larger rotation angles led to a blocking of the electron beam by the silicon frame that supports the Si_3N_4-membrane. For each angle of incidence, an electron energy loss spectrum was recorded at the center between the two tips of the

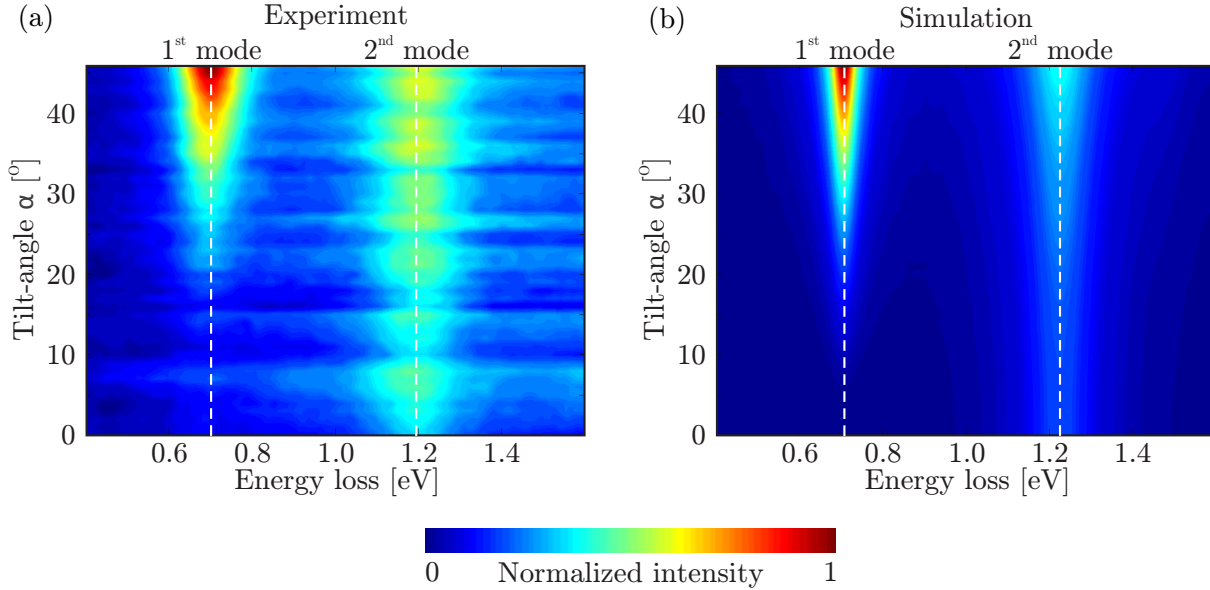SRR (see blue dot in fig. 7.1 (a)). Figure 7.3 (a) depicts this series of electron energy loss spectra.

Figure 7.3: (a) Measured oblique incidence electron energy loss spectra recorded between the two tips of a split-ring resonator for different tilt angles around the y-axis. (b) Corresponding calculated electron energy loss spectra. The dashed lines indicate the resonance energy of the first and the second plasmonic mode, respectively.

For normal incidence $(\alpha = 0°)$, there is no signature of the first plasmonic mode since its electric field is predominately oriented parallel to the substrate in the gap. However, for oblique incidence a peak emerges at the spectral position of the first plasmonic mode that continuously gains in strength with increasing α. This is in accordance with the expectations as the angle between the electron trajectory and the electric field lines of the first plasmonic mode in the region between the tips becomes smaller with increasing α. The second plasmonic mode at 1.19 eV is clearly visible even for normal incidence since its electric field distribution has a non-vanishing component along the electron trajectory (see fig. 7.2 (d,e)). With increasing angle of incidence, the intensity of the second plasmonic mode grows as well. However, this effect is less pronounced for the second plasmonic mode than for the first plasmonic mode. Therefore, for large values of α, the first plasmonic mode becomes the dominant spectral feature.

Within the experimental accuracy, the resonance energies of the two plasmonic modes do not shift with the angle of incidence and are identical to the values determined at the tips of the SRR for normal incidence. The depicted spectra were recorded for positive tilt angles. As might be expected from the geometry of the SRR, one finds, within the experimental accuracy, identical trends for negative tilt angles (not shown). The horizontal features in the contour plot are artifacts which stem from periodic cleaning of the sample in an

oxygen plasma to remove carbonaceous contamination caused by the illumination with the electron beam. The first cleaning of the sample with an oxygen plasma prior to the EELS experiments can result in a small blue shift of the resonances (see chapter 5). However, subsequent treatments with the oxygen plasma have no observable effect on the resonance frequencies.

Figure 7.3 (b) depicts the calculated electron energy loss spectra for the same conditions as in the experiments. The numerical calculations nicely reproduce the experimental results. In accordance with the experimental data, the calculated data show a dramatic increase of the intensity of the first plasmonic resonance (at 0.71 eV) and only a slight increase of the intensity of the second plasmonic resonance (at 1.22 eV) with increasing angle.

7.3   Tilt around y-axis

A control experiment was performed, in which the sample was rotated around the x-axis by $\beta = 46°$ (see fig. 7.1 (d)). In this case, the electron trajectory lies in the yz-plane and, hence, is normal to the electric field lines of the first plasmonic mode in the region between the tips (see fig. 7.2 (c)). The red curve in fig. 7.4 (a) depicts the corresponding electron energy loss spectrum recorded at the same position as in the previous experiment. In accordance with the expectations, the first plasmonic mode is absent in this spectrum. This finding is also reproduced by numerical calculations (see fig. 7.4 (b)).

It is interesting to compare the influence of the incidence angle on the intensity of the first plasmonic mode for different positions of the electron beam. Figure 7.5 depicts EELS maps of the first plasmonic mode for the cases (a) $\alpha = 0°, \beta = 0°$; (b) $\alpha = 46°, \beta = 0°$; and (c) $\alpha = 0°, \beta = 46°$. For a quantitative analysis, fig. 7.5 (d) shows line scans along
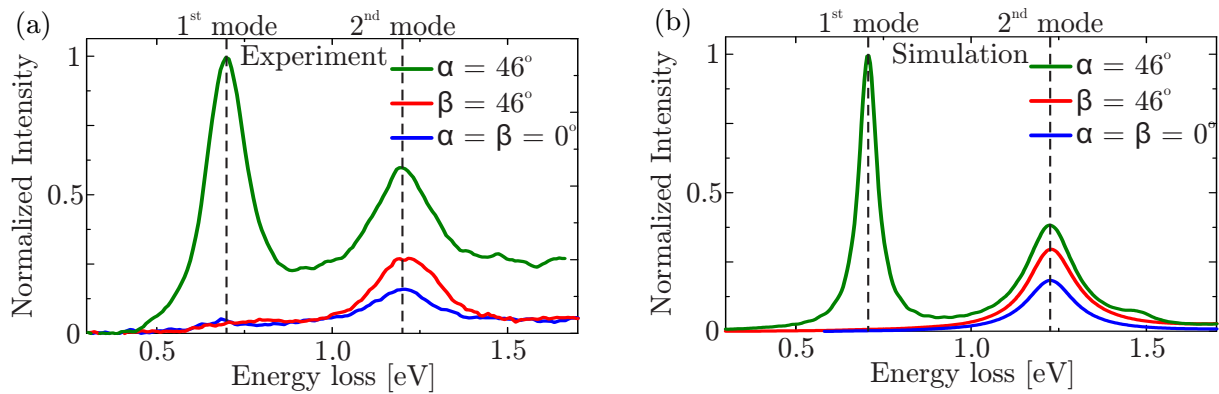

Figure 7.4: (a) Measured oblique incidence electron energy loss spectra recorded between the two tips of a split-ring resonator for different tilt angles around the y-axis. (b) Corresponding calculated electron energy loss spectra. The dashed lines indicate the resonance energy of the first and the second plasmonic mode, respectively.

the x-axis for $\alpha = 0°$ and $\alpha = 46°$ (see dotted lines in (a) and (b), respectively). Between the tips of the SRR, the intensity shows a strong dependence on α (see discussion above). In contrast, the intensity hardly changes if the electron beam incidents on one of the tips. A qualitative explanation for this behavior is that the electric field lines in the vicinity of the tips exhibit a radial character and thus always have a component parallel to the electron trajectory (see fig. 7.2 (b)).
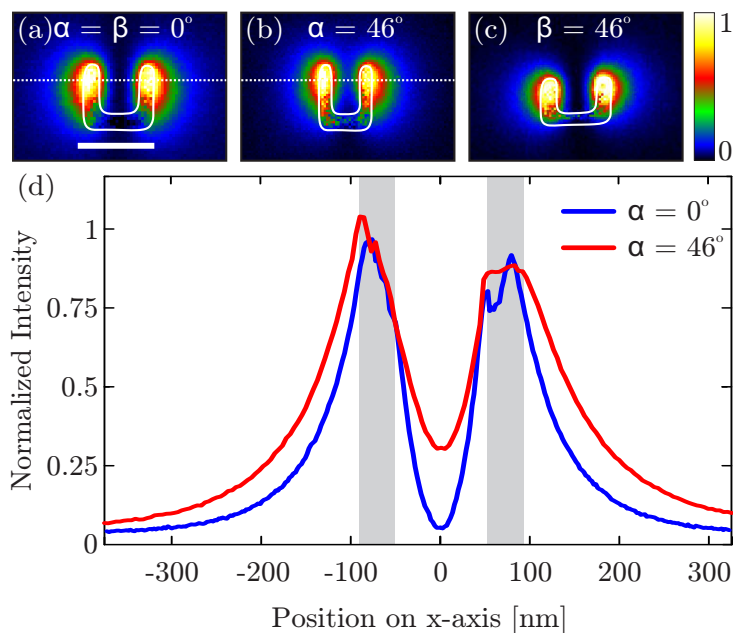

Figure 7.5: (a-c) EELS maps of the SRR depicted in fig. 7.1 (a) at an energy loss of 0.69 eV for three different tilt angles for $\alpha = 0°, \beta = 0°$; $\alpha = 46°, \beta = 0°$; and $\alpha = 0°, \beta = 46°$, respectively. The solid white lines indicate the boundaries of the SRR. The scale bar is 200 nm. (d) Line scans of the electron beam along the x-axis (dashed lines in (a) and (b)). The gray areas represent the positions of the SRR tips for $\alpha = 0°$.

7.4   Influence of the acceleration voltage

The above experiments were also performed at an acceleration voltage of 200 kV. Figure 7.6 (a) shows EEL spectra acquired at both acceleration voltages.

The resonance energies are identical for both acceleration voltages (within the experimental accuracy). This is not surprising, since the resonance energy is determined by the structure and not by the method of investigation (see the comparison to optical measurements in chapter 5). Nevertheless, two very interesting features can be seen in the spectra. (i) As expected the ZLP (the high tail emerging from the left, blue curve) is
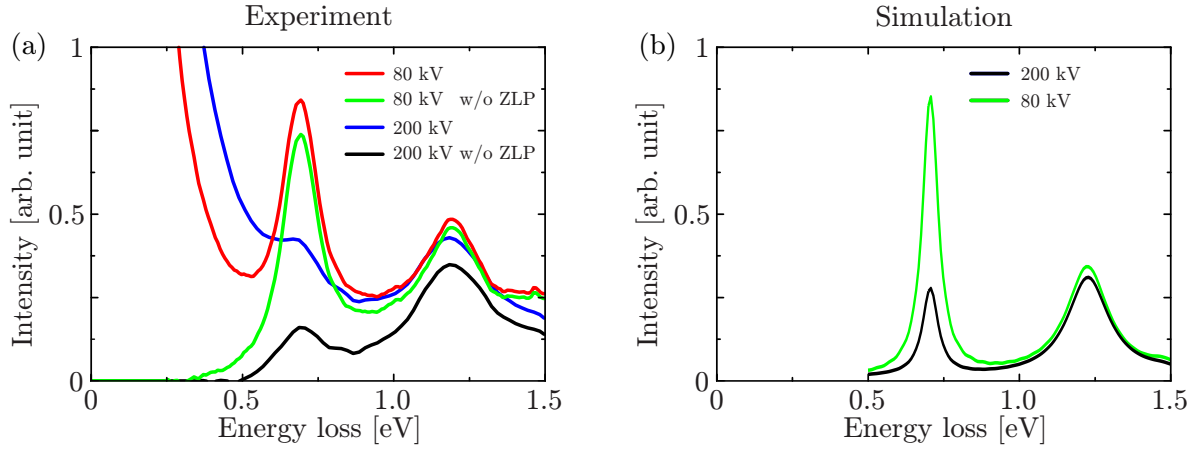
Figure 7.6: (a) Experimental EEL spectra acquired under $\alpha = 46°$ at the position marked in 7.1 (a) for an acceleration voltage of 80 kV and 200 kV. For both data sets, the original spectrum as well as the spectrum with a subtracted ZLP is displayed. (b) Corresponding simulated data.

essentially broader at an acceleration voltage of 200 kV (compare to 3.7 (b)). The plasmon resonance at 0.69 eV is thus only present as a 'shoulder' on the ZLP tail and needs to be extracted (black curve). The ZLP of the 80 kV spectrum is significantly narrower (red curve) and the plasmon resonance is clearly distinguishable even without a ZLP subtraction (green curve). (ii) More remarkable is the height of the resonances. While the second resonance has approximately the same height for both acceleration voltages, the first resonance shows an obvious difference. At 80 kV acceleration voltage, the height of the first resonance is approximately six times higher than in the case of 200 kV. Thus, the excitation probability of the first order mode is six times higher for 80 keV electrons than for 200 keV electrons. Since this observation holds only for the first (low energy) resonance, this effect is not only correlated to the electrons energy, but also to the plasmon energy. The simulations (fig. 7.6 (b)) show a similar trend and support the experimental findings.

Chapter 8

Conclusions

Electron energy loss spectroscopy (EELS) in combination with scanning transmission electron microscopy (STEM) was used to characterize the near field distribution of plasmonic nanostructures. The results were compared to optical experiments as well as numerical simulations. This work focuses on the near field properties of split-ring resonators (SRRs), which are one of the most prominent examples of metamaterials. The main results of this thesis are: (i) Proof of Babinet's principle in the near-infrared and visible regime, (ii) visualization of bright and dark modes in coupled nanoparticles, and (iii) a three dimensional analysis of the plasmonic near field of an individual SRR.

For the experiments in a transmission electron microscope, silicon nitride membranes served as an electron transparent substrate. The sample fabrication process via electron beam lithography was optimized for the membranes and structures with gap-distances down to 20 nm could be realized.

First of all, STEM-EELS was used on an isolated SRR to illustrate the versatile applicability of this technique. EEL spectra from preselected positions on the SRR revealed several resonances, which could be associated to plasmonic modes on the structure. The near field distributions of these modes were presented in EELS maps. A strong signal in an EELs map can be connected to a high energy loss probability of the incident electron and thus to a high charge density of the plasmonic mode. With increasing energy, the EELS map of the plasmonic modes exhibit an increasing number of maxima.

It is well known that the size of a nanoparticle influences its resonance frequency. To elucidate the influence of the size on the near field distribution, a series of SRRs with widths varying between 120 nm and 480 nm was fabricated. The recorded EELS maps revealed that the spatial mode distribution remains the same for all sizes (apart from a scaling factor). The resonance energies of the higher-order modes could also be investigated. It was disclosed that higher-order modes are more sensitive to the material dispersion of gold than the first-order mode.

Furthermore, EELS maps of the three lowest-order plasmonic modes of a SRR and the corresponding complementary SRR (CSRR) were compared. This comparison allows for

a direct visualization of Babinet's principle for all three modes, and thus showed that the generalized Babinet's principle still holds for near-infrared and visible frequencies. From the experimentalists' point of view this enables a new insight into metamaterials: Since magnetic fields do not change the kinetic energy of electrons, the magnetic near field of nanoparticles cannot be detected by EELS. Nevertheless, Babinet's principle allows for visualizing the magnetic near field of a metal nanoparticle, by investigating the electric field of its complementary structure. Simulations were employed and match the experimental results.

Plasmonic nanostructures are designed to interact with light. Therefore it is of upmost interest to compare the excitation of plasmons by electrons to the excitation by photons. On a set of four different antenna structures, optical extinction spectra were compared to EEL spectra. Within experimental errors, the two spectra exhibit identical resonance energies. The numerical approach shows a small red shift of the EEL spectra with respect to the optical simulations.

A metamaterial usually is composed of thousands or more nanoparticles. These nanoparticles show electromagnetic interactions among each other, which influence and change the near field distribution and the resonance energies of the plasmonic modes. For a thorough understanding of coupling effects in metamaterials, the evolution of the plasmonic near field was investigated in the course of the transition from an isolated SRR to a metamaterial. In accordance with the plasmon hybridization model, the interaction in small SRR ensembles resulted in the formation of distinct optical bright and dark eigenmodes. The occurrence of these modes can be explained by coupling dipoles. For large SRR arrays, the formation of a quasi-continuum of modes was observed in the interior of the array and edge-modes were found at the boundaries. Numerical simulations were performed for small SRR ensembles and support the experimental findings.

STEM-EELS probes the near field distribution of plasmons only in the direction of the electron beam trajectory. Electric fields that are perpendicular to the electron beam can therefore not be detected. For certain electric field configurations this leads to a vanishing energy loss probability. To probe the near field in three dimensions, one can tilt the sample and perform angular-resolved EELS. In particular, it was shown that angular-resolved EELS can detect a signal in between the two arms of a SRR which could not be detected under normal incidence. Simulations were also employed and are in excellent agreement with the experimental findings.

Outlook

In this work, plasmon mapping with a Libra 200 microscope was established. The results of this work can be used as basis for future projects. In particular structures with more complex near fields as for example, oligomers or dolmen-like structures are of high interest to the community.

Furthermore, one could investigate gold nanotips. They are used to concentrate and enhance non-linear optical effects, such as laser induced photoemission [123]. The nanotips are free standing cones on which plasmons travel towards the apex (diameter of approx. 20 nm) leading to a huge field enhancement.

Another interesting light harvesting device is a crescent, where the two ends touch and form a singularity. The plasmons are expected to travel towards the singularity, where their energy accumulates. Simulations provide a field enhancement at this position of approximately 10^4 [124].

Recently our group succeeded in the fabrication of stacked metamaterials on an electron transparent substrate. A second electron beam lithography step was used to place nanostructures on both sides of a silicon nitride membrane [125]. When investigated with EELS, two meta-atoms placed above each other should show similar coupling effects, as have already been observed in lateral dimensions. However, the 30 nm thin membrane between the meta-atoms may have an influence. Such results could be very helpful for the design of stacked-layer metamaterials.

CHAPTER 9

APPENDIX

9.1 The split-ring resonator as an RLC-circuit

A SRR excited by an external electric field can be described by a driven RLC-circuit. In this simplified picture, the ring of the SRR is represented by a coil (only one loop) with the inductance L. The gap (the split) is represented by a capacitor with the capacitance C (see figure 2.3). The damping of the SRR can be described by Ohmic losses, via the resistance R. The resonance frequency and the quality factor of the RLC-circuit are given by:

$$\omega_{\mathrm{LC}} = \frac{1}{\sqrt{LC}}, \tag{9.1}$$

$$Q_{\mathrm{LC}} = \frac{\omega_{\mathrm{p}}}{\Delta\omega} = \frac{\sqrt{L/C}}{R}, \tag{9.2}$$

where $\Delta\omega$ is the full width at half maximum (FWHM) of the resonance, and ω_{p} is the peak position. For a quantitative analysis of this analogy, textbook formulae are applied for the inductivity and the capacity ($L = N \cdot \mu_0 \frac{\mathrm{area}}{\mathrm{length}}$, with N being the number of loops, and $C = \epsilon_0\epsilon\frac{\mathrm{area}}{\mathrm{distance}}$). For a uniform current distribution, the thickness (l_{z}) of the SRR is assumed to be much smaller than its width (l_{x}) and height (l_{y}). Therefore one obtains:

$$L = 1 \cdot \mu_0 \frac{l_{\mathrm{x}} l_{\mathrm{y}}}{l_{\mathrm{z}}} \quad \text{and} \tag{9.3}$$

$$C = \epsilon_0\epsilon\frac{(l_{\mathrm{y}} - h)l_{\mathrm{z}}}{d} . \tag{9.4}$$

With equation 9.1, the resonance frequency becomes:

$$\omega_{\mathrm{LC}} = \frac{c_0}{\sqrt{\epsilon l_{\mathrm{x}} l_{\mathrm{y}}}}\sqrt{\frac{d}{l_{\mathrm{y}} - h}} \propto \frac{1}{\mathrm{size}} . \tag{9.5}$$

Although a few assumptions were made, this formula is a good tool to understand the SRR. First of all one can see that the resonance frequency is inversely proportional to the linear dimension of the SRR. Decreasing the size of the SRR leads to an increase of the resonance frequency. As will see be seen later, this holds only for frequencies well below the plasma frequency [58–60]. In the quasi-static regime, the resonance frequency is independent of the particles size, as can be seen in equation 2.17. The formula also allows to estimate the size of an SRR, which shows a resonant behavior at 1.5 μm. In that case the linear dimensions are in the range of $l_{\mathrm{x}} = l_{\mathrm{y}} = 200\,\mathrm{nm}$ with a thickness of about 50 nm [49]. The capacitance and the inductance for these dimensions are in the range of $C \approx 1\,\mathrm{aF}$ and $L \approx 1\,\mathrm{pH}$, respectively [58].

The RLC-circuit model also helps to estimate the permeability of a SRR. Therefore one considers an electromagnetic wave, where only the magnetic part can couple to the SRR (i.e., the magnetic field is perpendicular to the SRR plane). Furthermore, the quasistatic limit is assumed (i.e., retardation effects are neglected). In that case, the self-induced voltage of the inductance L plus the voltage drop at the capacitance C and the resistance R are equal to the induced voltage U_{ind} of the external field $U_{\mathrm{L}} + U_{\mathrm{R}} + U_{\mathrm{C}} = U_{\mathrm{ind}}$:

$$L\dot{I} + RI + \frac{1}{C}\int I dt \;=\; U_{\mathrm{ind}} \;=\; -\dot{\Phi}\,, \tag{9.6}$$

where $\Phi(t)$ is the total magnetic flux through the surface. Considering a homogeneous magnetic field in the coil, one can solve the surface integral for the external magnetic flux:

$$\Phi(t) = \int B(t)dS \;=\; \mu_0 l^2 H(t)\,, \tag{9.7}$$

where $H(t) = H_0 \exp(-\imath\omega t) + c.c.$ is the magnetic field of the incident electromagnetic wave and $l^2 = l_{\mathrm{x}}l_{\mathrm{y}}$. Inserting Φ and $H(t)$ into 9.6 and taking the time derivative, one gets:

$$\ddot{I} + \frac{R}{L}\dot{I} + \frac{1}{LC}I \;=\; \frac{1}{L}\dot{U}_{\mathrm{ind}} \;=\; +\omega^2 \frac{\mu_0 l^2}{L} H_0 \exp(-\imath\omega t) + c.c.\,. \tag{9.8}$$

With the ansatz $I = I_0 \exp(-\imath\omega t) + c.c.$ one obtains:

$$-\omega^2 I_0 + -\imath\omega\gamma I_0 + \omega_{\mathrm{LC}}^2 I_0 \;=\; \omega^2 l_{\mathrm{z}} H_0\,. \tag{9.9}$$

Here $\gamma = \frac{R}{L}$, $\omega_{\mathrm{RLC}} = \frac{1}{\sqrt{RLC}}$ and $L = \mu_0 \frac{l^2}{l_{\mathrm{z}}}$ was used. Now the magnetic dipole moment $l^2 I$ for a single LC-circuit is introduced, and the magnetization $M = (N_{\mathrm{RLC}}/V)l^2 I$ for multiple LC-circuits, where N_{RLC} is the number of LC-circuits and V is the corresponding volume. The magnetization and the magnetic field are correlated via: $M = \mu_0 \chi_{\mathrm{m}} H$, where $\chi_{\mathrm{m}} = \mu - 1$ is the magnetic susceptibility. Thus one can express the magnetic field as:

$$H = \frac{M}{\mu_0 \chi_{\mathrm{m}}} = \frac{N_{\mathrm{LC}} l^2}{V \mu_0 \chi_{\mathrm{m}}} I\,. \tag{9.10}$$

Inserting 9.10 into 9.9 yields:

$$-\omega^2 I_0 + -\imath\omega\gamma I_0 + \omega_{\mathrm{LC}}^2 I_0 \quad = \quad \frac{\omega^2 l_{\mathrm{z}} l^2 N_{\mathrm{LC}}}{\mu_0 \chi_{\mathrm{m}} V} I_0 \,. \tag{9.11}$$

Let the distance between two neighboring SRRs be a_{x}, a_{y}, and a_{z}, then $N_{\mathrm{LC}}/V = 1/(a_{\mathrm{x}} a_{\mathrm{y}} a_{\mathrm{z}})$. With $\chi_{\mathrm{m}} = \mu - 1$, this leads to:

$$\mu(\omega) \quad = \quad 1 + \frac{f\omega^2}{\omega_{\mathrm{LC}}^2 - \imath\omega\gamma - \omega^2} \,. \tag{9.12}$$

with f being a dimensionless quantity:

$$0 \;\leq\; f \;\; = \;\; \frac{l_{\mathrm{x}} l_{\mathrm{y}} l_{\mathrm{z}}}{a_{\mathrm{x}} a_{\mathrm{y}} a_{\mathrm{z}}} \;\leq\; 1 \,. \tag{9.13}$$

One can interpret f as the filling factor, where $f = 1$ correspond to touching nearest neighbors. Comparing equation 9.12 with equation 2.14, one can conclude that μ represents a Lorentz oscillator, with the additional filling factor. Equation 9.12 indicates that the permeability of a SRRs can be tuned, and for frequencies above the resonance frequencies can even reach negative values. A more detailed analysis of the inductance and the capacitance is presented in [126], in which the SRR is on a substrate, not in vacuum.

Bibliography

[1] S. Linden, C. Enrich, M. Wegener, J. F. Zhou, T. Koschny, and C. M. Soukoulis, "Magnetic response of metamaterials at 100 terahertz," Science **306**, 1351–1353 (2004).

[2] S. Zhang, W. J. Fan, B. K. Minhas, A. Frauenglass, K. J. Malloy, and S. R. J. Brueck, "Midinfrared resonant magnetic nanostructures exhibiting a negative permeability," Physical Review Letters **94**, 037402 (2005).

[3] C. Enrich, M. Wegener, S. Linden, S. Burger, L. Zschiedrich, F. Schmidt, J. F. Zhou, T. Koschny, and C. M. Soukoulis, "Magnetic metamaterials at telecommunication and visible frequencies," Physical Review Letters **95**, 203901 (2005).

[4] V. M. Shalaev, "Optical negative-index metamaterials," Nature Photonics **1**, 41–48 (2007).

[5] C. M. Soukoulis, S. Linden, and M. Wegener, "Negative refractive index at optical wavelengths," Science **315**, 47–49 (2007).

[6] A. V. Rogacheva, V. A. Fedotov, A. S. Schwanecke, and N. I. Zheludev, "Giant gyrotropy due to electromagnetic-field coupling in a bilayered chiral structure," Physical Review Letters **97**, 177401 (2006).

[7] S. Zhang, Y.-S. Park, J. Li, X. Lu, W. Zhang, and X. Zhang, "Negative refractive index in chiral metamaterials," Physical Review Letters **102**, 023901 (2009).

[8] J. K. Gansel, M. Thiel, M. S. Rill, M. Decker, K. Bade, V. Saile, G. von Freymann, S. Linden, and M. Wegener, "Gold helix photonic metamaterial as broadband circular polarizer," Science **325**, 1513–1515 (2009).

[9] C. Sonnichsen, S. Geier, N. Hecker, G. von Plessen, J. Feldmann, H. Ditlbacher, B. Lamprecht, J. Krenn, F. Aussenegg, V. Chan, J. Spatz, and M. Moller, "Spectroscopy of single metallic nanoparticles using total internal reflection microscopy," Applied Physics Letters **77**, 2949–2951 (2000).

[10] O. L. Muskens, N. Del Fatti, F. Vallee, J. R. Huntzinger, P. Billaud, and M. Broyer, "Single metal nanoparticle absorption spectroscopy and optical characterization," Applied Physics Letters **88**, 063109 (2006).

[11] M. Husnik, M. W. Klein, N. Feth, M. Koenig, J. Niegemann, K. Busch, S. Linden, and M. Wegener, "Absolute extinction cross-section of individual magnetic split-ring resonators," Nature Photonics **2**, 614–617 (2008).

[12] M.-W. Chu, V. Myroshnychenko, C. H. Chen, J.-P. Deng, C.-Y. Mou, and F. Javier Garcia de Abajo, "Probing bright and dark surface-plasmon modes in individual and coupled noble metal nanoparticles using an electron beam," Nano Letters **9**, 399–404 (2009).

[13] I. Alber, W. Sigle, S. Mueller, R. Neumann, O. Picht, M. Rauber, P. A. van Aken, and M. E. Toimil-Molares, "Visualization of multipolar longitudinal and transversal surface plasmon modes in nanowire dimers," ACS Nano **5**, 9845–9853 (2011).

[14] F.-P. Schmidt, H. Ditlbacher, U. Hohenester, A. Hohenau, F. Hofer, and J. R. Krenn, "Dark plasmonic breathing modes in silver nanodisks," Nano Letters **12**, 5780–5783 (2012).

[15] G. Boudarham, N. Feth, V. Myroshnychenko, S. Linden, J. Garcia de Abajo, M. Wegener, and M. Kociak, "Spectral imaging of individual split-ring resonators," Physical Review Letters **105**, 255501 (2010).

[16] C. Diaz-Egea, W. Sigle, P. A. van Aken, and S. I. Molina, "High spatial resolution mapping of surface plasmon resonance modes in single and aggregated gold nanoparticles assembled on DNA strands," Nanoscale Research Letters **8**, 337 (2013).

[17] R. H. Ritchie, "Plasma losses by fast electrons in thin films," Physical Review **106**, 874–881 (1957).

[18] J. Nelayah, M. Kociak, O. Stephan, F. J. Garcia de Abajo, M. Tence, L. Henrard, D. Taverna, I. Pastoriza-Santos, L. M. Liz-Marzan, and C. Colliex, "Mapping surface plasmons on a single metallic nanoparticle," Nature Physics **3**, 348–353 (2007).

[19] M. Bosman, V. J. Keast, M. Watanabe, A. I. Maaroof, and M. B. Cortie, "Mapping surface plasmons at the nanometre scale with an electron beam," Nanotechnology **18**, 165505 (2007).

[20] B. Schaffer, U. Hohenester, A. Trugler, and F. Hofer, "High-resolution surface plasmon imaging of gold nanoparticles by energy-filtered transmission electron microscopy," Physical Review B **79**, 041401 (2009).

[21] M. N'Gom, S. Li, G. Schatz, R. Erni, A. Agarwal, N. Kotov, and T. B. Norris, "Electron-beam mapping of plasmon resonances in electromagnetically interacting gold nanorods," Physical Review B **80**, 113411 (2009).

[22] F. Song, T. Wang, X. Wang, C. Xu, L. He, J. Wan, C. Van Haesendonck, S. P. Ringer, M. Han, Z. Liu, and G. Wang, "Visualizing plasmon coupling in closely spaced chains of Ag nanoparticles by electron energy-loss spectroscopy," Small **6**, 446–451 (2010).

[23] W. Sigle, J. Nelayah, C. T. Koch, and P. A. van Aken, "Electron energy losses in Ag nanoholes-from localized surface plasmon resonances to rings of fire," Optics Letters **34**, 2150–2152 (2009).

[24] A. L. Koh, A. I. Fernandez-Dominguez, D. W. McComb, S. A. Maier, and J. K. W. Yang, "High-resolution mapping of electron-beam-excited plasmon modes in lithographically defined gold nanostructures," Nano Letters **11**, 1323–1330 (2011).

[25] J. Nelayah, L. Gu, W. Sigle, C. T. Koch, I. Pastoriza-Santos, L. M. Liz-Marzan, and P. A. van Aken, "Direct imaging of surface plasmon resonances on single triangular silver nanoprisms at optical wavelength using low-loss EFTEM imaging," Optics Letters **34**, 1003–1005 (2009).

[26] D. Rossouw and G. A. Botton, "Plasmonic response of bent silver nanowires for nanophotonic subwavelength waveguiding," Physical Review Letters **110**, 066801 (2013).

[27] A. L. Koh, K. Bao, I. Khan, W. E. Smith, G. Kothleitner, P. Nordlander, S. A. Maier, and D. W. McComb, "Electron energy-loss spectroscopy (EELS) of surface plasmons in single silver nanoparticles and dimers: Influence of beam damage and mapping of dark modes," ACS Nano **3**, 3015–3022 (2009).

[28] J. D. Jackson, *Classical Electrodynamics* (John Wiley & Sons, Inc. 3rd edition, 1998).

[29] P. Drude, "Zur Elektronentheorie der Metalle," Ann. Phys. **306**, 566–613 (1900).

[30] N. E. Christensen and B. O. Seraphin, "Relativistic band calculation and optical properties of gold," Physical Review B **4**, 3321 (1971).

[31] C. Bohren and D. Huffman, *Absorption and scattering of light by small particles* (John Wiley & Sons, Inc., New York, 1983).

[32] A. Vial, A. S. Grimault, D. Macias, D. Barchiesi, and M. L. de la Chapelle, "Improved analytical fit of gold dispersion: Application to the modeling of extinction spectra with a finite-difference time-domain method," Physical Review B **71**, 085416 (2005).

[33] M. C. König, "Discontinuous Galerkin methods in nanophotonics," Ph.D. thesis, Karlsruher Instituts für Technologie (KIT) (2011).

[34] L. Novotny and B. Hecht, *Principles of Nano-Optics* (Cambridge University Press, 2007).

[35] H. Ibach and H. Lüth, *Festkörperphysik: eine Einführung in die Grundlagen*, Springer-Lehrbuch (Springer, 1999).

[36] A. Otto, "Excitation of nonradiative surface plasma waves in silver by method of frustrated total reflection," Zeitschrift Für Physik **216**, 398 (1968).

[37] E. Kretschmann and H. Raether, "Radiative decay of non radiative surface plasmons excited by light," Zeitschrift Für Naturforschung Part A - Astrophysik Und Physikalische Chemie **A 23**, 2135 (1968).

[38] Y. Y. Teng and E. A. Stern, "Plasma radiation from metal grating surfaces," Physical Review Letters **19**, 511 (1967).

[39] A. G. Brolo, "Plasmonics for future biosensors," Nature Photonics **6**, 709–713 (2012).

[40] P. Bharadwaj, B. Deutsch, and L. Novotny, "Optical antennas," Advances in optics and photonics **1**, 438–483 (2009).

[41] M. Kauranen and A. V. Zayats, "Nonlinear plasmonics," Nature Photonics **6**, 737–748 (2012).

[42] M. S. Tame, K. R. McEnery, S. K. Oezdemir, J. Lee, S. A. Maier, and M. S. Kim, "Quantum plasmonics," Nature Physics **9**, 329–340 (2013).

[43] K. Kneipp, Y. Wang, H. Kneipp, L. T. Perelman, I. Itzkan, R. Dasari, and M. S. Feld, "Single molecule detection using surface-enhanced Raman scattering (SERS)," Physical Review Letters **78**, 1667–1670 (1997).

[44] R. G. Freeman, K. C. Grabar, K. J. Allison, R. M. Bright, J. A. Davis, A. P. Guthrie, M. B. Hommer, M. A. Jackson, P. C. Smith, D. G. Walter, and M. J. Natan, "Self-assembled metal colloid monolayers - an approach to SERS subtrates," Science **267**, 1629–1632 (1995).

[45] B. Lamprecht, A. Leitner, and F. R. Aussenegg, "Femtosecond decay-time measurement of electron-plasma oscillation in nanolithographically designed silver particles," Applied physics B-Lasers and optics **64**, 269–272 (1997).

[46] A. Wokaun, J. G. Bergman, J. O. Heritage, A. M. Glass, P. F. Liao, and D. H. Olson, "Surface second-harmonic generation from metal island films and microlithographic structures," Phys. Rev. B **24**, 849–856 (1981).

[47] G. Mie, "Beiträge zur Optik trüber Medien, speziell kolloidaler Metallösungen," Ann. Phys. **25**, 377 (1908).

[48] N. Swanson and C. J. Powell, "Inelastic scattering cross sections for 20-kev electrons in Al, Be, and polystyrene," Phys. Rev. **145**, 195 (1966).

[49] N.-A. Feth, "Nonlinear optics of planar metamaterial arrays and spectroscopy of individual "photonic atoms"," Ph.D. thesis, Karlsruher Instituts für Technologie (KIT) (2010).

[50] F. J. Garcia de Abajo and M. Kociak, "Probing the photonic local density of states with electron energy loss spectroscopy," Physical Review Letters **100**, 106804 (2008).

[51] U. Hohenester, H. Ditlbacher, and J. R. Krenn, "Electron-energy-loss spectra of plasmonic nanoparticles," Physical Review Letters **103**, 106801 (2009).

[52] V. G. Veselago, "The electrodynamics of substances with simultaneously negative values of σ and μ," Soviet Physics Uspekhi-USSR **10**, 509 (1968).

[53] J. B. Pendry, "Negative refraction makes a perfect lens," Physical Review Letters **85**, 3966–3969 (2000).

[54] J. B. Pendry, A. J. Holden, W. J. Stewart, and I. Youngs, "Extremely low frequency plasmons in metallic mesostructures," Physical Review Letters **76**, 4773–4776 (1996).

[55] R. A. Shelby, D. R. Smith, and S. Schultz, "Experimental verification of a negative index of refraction," Science **292**, 77–79 (2001).

[56] W. N. Hardy and L. A. Whitehead, "Split-ring resonator for use in magnetic resonance from 200-2000MHz," Rev. Sci. Instrum. **52**, 213–216 (1981).

[57] J. B. Pendry, A. J. Holden, D. J. Robbins, and W. J. Stewart, "Magnetism from conductors and enhanced nonlinear phenomena," IEEE Transactions on microwave theory and techniques **47**, 2075–2084 (1999).

[58] S. Linden, C. Enrich, G. Dolling, M. W. Klein, J. Zhou, T. Koschny, C. M. Soukoulis, S. Burger, F. Schmidt, and M. Wegener, "Photonic metamaterials: Magnetism at optical frequencies," IEEE Journal of selected topics in quantum electronics **12**, 1097–1105 (2006).

[59] J. Zhou, T. Koschny, M. Kafesaki, E. N. Economou, J. B. Pendry, and C. M. Soukoulis, "Saturation of the magnetic response of split-ring resonators at optical frequencies," Physical Review Letters **95**, 223902 (2005).

[60] M. W. Klein, C. Enrich, M. Wegener, C. M. Soukoulis, and S. Linden, "Single-slit split-ring resonators at optical frequencies: limits of size scaling," Optics Letters **31**, 1259–1261 (2006).

[61] L. Novotny, "Effective wavelength scaling for optical antennas," Physical Review Letters **98**, 266802 (2007).

[62] M. Born and E. Wolf, *Principles of optics* (Cambridge University Press, Cambridge, 1999).

[63] F. Falcone, T. Lopetegi, M. A. G. Laso, J. D. Baena, J. Bonache, M. Beruete, R. Marqués, F. Martín, and M. Sorolla, "Babinet principle applied to the design of metasurfaces and metamaterials," Phys. Rev. Lett. **93**, 197401 (2004).

[64] T. Zentgraf, T. P. Meyrath, A. Seidel, S. Kaiser, H. Giessen, C. Rockstuhl, and F. Lederer, "Babinet´s principle for optical frequency metamaterials and nanoantennas," Phys. Rev. B **76(3)**, 033407 (2007).

[65] A. Bitzer, A. Ortner, H. Merbold, T. Feurer, and M. Walther, "Terahertz near-field microscopy of complementary planar metamaterials: Babinet´s principle," Opt. Express **19(3)**, 2537–2545 (2011).

[66] F. von Cube, S. Irsen, J. Niegemann, C. Matyssek, W. Hergert, K. Busch, and S. Linden, "Spatio-spectral characterization of photonic meta-atoms with electron energy-loss spectroscopy [Invited]," Optical Materials Express **1**, 1009–1018 (2011).

[67] P. Nordlander, K. L. C. Oubre, E. Prodan, and M. I. Stockman, "Plasmon hybridization in nanoparticle dimers," Nano Letters **4**, 899 – 903 (2004).

[68] E. Prodan, C. Radloff, N. J. Halas, and P. Nordlander, "A hybridization model for the plasmon response of complex nanostructures," Science **302**, 419–422 (2003).

[69] N. Liu, H. Liu, S. Zhu, and H. Giessen, "Stereometamaterials," Nature Photonics **3**, 157–162 (2009).

[70] T. Weber, "Nahfelduntersuchungen an plasmonischen Oligomeren," Master's thesis, University of Bonn (2012).

[71] T. H. P. Chang, "Proximity effect in electron-beam lithography," Journal of Vacuum Science & Technology **12**, 1271–1275 (1975).

[72] R. Erni, M. D. Rossell, C. Kisielowski, and U. Dahmen, "Atomic-resolution imaging with a sub-50-pm electron probe," Phys. Rev. Lett. **102**, 096101 (2009).

[73] D. B. Williams and C. B. Carter, *Transmission Electron Microscopy* (Springer, 2009).

[74] *Libra 200 user manual*.

[75] H. Rose, "Electrostatic energy filter as monochromator of a highly coherent electron source," Optik **86**, 95–98 (1990).

[76] F. Kahl, "Design eines Monochromators für Elektronenquellen," Ph.D. thesis, Technische Universität Darmstadt (1999).

[77] F. Zemlin, K. Weiss, P. Schiske, W. Kunath, and K. H. Herrmann, "Coma-free alignment of high-resolution electron-microscopes with aid of optical diffractograms," Ultramicroscopy **3**, 49–60 (1978).

[78] R. Erni, *Aberration-corrected imaging in transmission electron microscopy* (Imperial College Press, 2010).

[79] *Aberration corrector manual, CEOS.*

[80] O. L. Krivanek, A. J. Gubbens, and N. Dellby, "Developments in EELS instrumentation for spectroscopy and imaging," Micoscopy Micoranalysis Microstructures **2**, 315–332 (1991).

[81] A. J. Gubbens, H. A. Brink, M. K. Kundmann, S. L. Friedman, and O. L. Krivanek, "A post-column imaging energy filter with a 2048^2-pixel slow-scan CCD camera," Micron **29**, 81–87 (1998).

[82] H. Rose and E. Plies, "Design of a magnetic energy analyzer with small aberrations," Optik **40**, 336–341 (1974).

[83] W. Probst, G. Benner, J. Bihr, and E. Weimer, "An Omega energy filtering TEM - Principles and applications," Advanced Materials **5**, 297–300 (1993).

[84] S. Uhlemann and H. Rose, "The mandoline filter - a new high-performance imaging filter for sub-eV EFTEM," Optik **96**, 163–178 (1994).

[85] D. Krahl and S. Kujawa, "Elektronenmikroskop mit einem abbildenden magnetischen Energiefilter," (1999). EP Patent App. EP19,990,111,296.

[86] S. O. Kucheyev, T. van Buuren, T. F. Baumann, J. H. Satcher, T. M. Willey, R. W. Meulenberg, T. E. Felter, J. F. Poco, S. A. Gammon, and L. J. Terminello, "Electronic structure of titania aerogels from soft x-ray absorption spectroscopy," Phys. Rev. B **69**, 245102 (2004).

[87] J. Niegemann, M. Koenig, K. Stannigel, and K. Busch, "Higher-order time-domain methods for the analysis of nano-photonic systems," Photonics and nanostructures-Fundamentals and applications **7**, 2–11 (2009).

[88] K. Stannigel, M. Koenig, J. Niegemann, and K. Busch, "Discontinuous Galerkin time-domain computations of metallic nanostructures," Optics Express **17**, 14934–14947 (2009).

[89] K. Busch, M. Koenig, and J. Niegemann, "Discontinuous Galerkin methods in nanophotonics," Laser & Photonic Reviews **5**, 773–809 (2011).

[90] R. J. LeVeque, *Finite Volume Methods for Hyperbolic Problems* (Cambridge Texts in Applied Mathematics, 2002).

[91] C. Matyssek, J. Niegemann, W. Hergert, and K. Busch, "Computing electron energy loss spectra with the discontinuous Galerkin time-domain method," Photonics and nanostructures-Fundamentals and applications **9**, 367–373 (2011).

[92] P. B. Johnson and R. W. Christy, "Optical constants of noble metal," Physical Review B **6**, 4370–4379 (1972).

[93] M. Husnik, "Quantitative optische Spektroskopie einzelner metallischer Nanostrukturen," Ph.D. thesis, Karlsruher Instituts für Technologie (KIT) (2013).

[94] A. Arbouet, D. Christofilos, N. Del Fatti, F. Vallee, J. R. Huntzinger, L. Arnaud, P. Billaud, and M. Broyer, "Direct measurement of the single-metal-cluster optical absorption," Physical Review Letters **93**, 127401 (2004).

[95] M. Husnik, S. Linden, R. Diehl, J. Niegemann, K. Busch, and M. Wegener, "Quantitative experimental determination of scattering and absorption cross-section spectra of individual optical metallic nanoantennas," Physical Review Letters **109**, 233902 (2012).

[96] C. Rockstuhl, F. Lederer, C. Etrich, T. Zentgraf, J. Kuhl, and H. Giessen, "On the reinterpretation of resonances in split-ring-resonators at normal incidence," Optics Express **14**, 8827–8836 (2006).

[97] F. von Cube, S. Irsen, R. Diehl, J. Niegemann, K. Busch, and S. Linden, "From isolated metaatoms to photonic metamaterials: Evolution of the plasmonic near-field," Nano Letters **13**, 703–708 (2013).

[98] M. Husnik, F. von Cube, S. Irsen, S. Linden, J. Niegemann, K. Busch, and M. Wegener, "Comparison of electron energy-loss and quantitative optical spectroscopy on individual optical gold antennas," Nanophotonics **2**, 241–245 (2013).

[99] U. Kreibig and P. Zacharias, "Surface plasma resonances in small spherical silver and gold particles," Zeitschrift für Physik **231**, 128 (1970).

[100] M. N'Gom, J. Ringnalda, J. F. Mansfield, A. Agarwal, N. Kotov, N. J. Zaluzec, and T. B. Norris, "Single particle plasmon spectroscopy of silver nanowires and gold nanorods," Nano Letters **8**, 3200–3204 (2008).

[101] B. S. Guiton, V. Iberi, S. Li, D. N. Leonard, C. M. Parish, P. G. Kotula, M. Varela, G. C. Schatz, S. J. Pennycook, and J. P. Camden, "Correlated optical measurements and plasmon mapping of silver nanorods," Nano Letters **11**, 3482–3488 (2011).

[102] V. Myroshnychenko, J. Nelayah, G. Adamo, N. Geuquet, J. Rodriguez-Fernandez, I. Pastoriza-Santos, K. F. MacDonald, L. Henrard, L. M. Liz-Marzan, N. I. Zheludev, M. Kociak, and F. Javier Garcia de Abajo, "Plasmon spectroscopy and imaging of individual gold nanodecahedra: A combined optical microscopy, cathodoluminescence, and electron energy-loss spectroscopy study," Nano Letters **12**, 4172–4180 (2012).

[103] J. Zuloaga and P. Nordlander, "On the energy shift between near-field and far-field peak intensities in localized plasmon systems," Nano Letters **11**, 1280–1283 (2011).

[104] B. M. Ross and L. P. Lee, "Comparison of near- and far-field measures for plasmon resonance of metallic nanoparticles," Optics Letters **34**, 896–898 (2009).

[105] J. Nelayah, M. Kociak, O. Stephan, N. Geuquet, L. Henrard, F. J. Garcia de Abajo, I. Pastoriza-Santos, L. M. Liz-Marzan, and C. Colliex, "Two-Dimensional quasistatic stationary short range surface plasmons in flat nanoprisms," Nano Letters **10**, 902–907 (2010).

[106] L.-H. Shao, M. Ruther, S. Linden, S. Essig, K. Busch, J. Weissmueller, and M. Wegener, "Electrochemical modulation of photonic metamaterials," Advanced Materials **22**, 5173 (2010).

[107] I. Sersic, M. Frimmer, E. Verhagen, and A. F. Koenderink, "Electric and magnetic dipole coupling in near-infrared split-ring metamaterial arrays," Physical Review Letters **103**, 213902 (2009).

[108] M. Decker, N. Feth, C. M. Soukoulis, S. Linden, and M. Wegener, "Retarded long-range interaction in split-ring-resonator square arrays," Physical Review B **84**, 085416 (2011).

[109] N. Feth, M. Koenig, M. Husnik, K. Stannigel, J. Niegemann, K. Busch, M. Wegener, and S. Linden, "Electromagnetic interaction of split-ring resonators: The role of separation and relative orientation," Optics Express **18**, 6545–6554 (2010).

[110] M. Decker, S. Burger, S. Linden, and M. Wegener, "Magnetization waves in split-ring-resonator arrays: Evidence for retardation effects," Physical Review B **80**, 193102 (2009).

[111] B. Luk'yanchuk, N. I. Zheludev, S. A. Maier, N. J. Halas, P. Nordlander, H. Giessen, and C. T. Chong, "The Fano resonance in plasmonic nanostructures and metamaterials," Nature Materials **9**, 707–715 (2010).

[112] S. Linden, F. B. P. Niesler, J. Foerstner, Y. Grynko, T. Meier, and M. Wegener, "Collective effects in second-harmonic generation from split-ring-resonator arrays," Physical Review Letters **109**, 015502 (2012).

[113] S. Zhang, D. A. Genov, Y. Wang, M. Liu, and X. Zhang, "Plasmon-induced transparency in metamaterials," Physical Review Letters **101**, 047401 (2008).

[114] E. Prodan, C. Radloff, N. Halas, and P. Nordlander, "A hybridization model for the plasmon response of complex nanostructures," Science **302**, 419–422 (2003).

[115] W. Rechberger, A. Hohenau, A. Leitner, J. Krenn, B. Lamprecht, and F. Aussenegg, "Optical properties of two interacting gold nanoparticles," Optics Communication **220**, 137–141 (2003).

[116] J. A. Fan, C. Wu, K. Bao, J. Bao, R. Bardhan, N. J. Halas, V. N. Manoharan, P. Nordlander, G. Shvets, and F. Capasso, "Self-assembled plasmonic nanoparticle clusters," Science **328**, 1135–1138 (2010).

[117] M. Hentschel, D. Dregely, R. Vogelgesang, H. Giessen, and N. Liu, "Plasmonic oligomers: The role of individual particles in collective behavior," ACS Nano **5**, 2042–2050 (2011).

[118] D. J. Bergman and M. I. Stockman, "Surface plasmon amplification by stimulated emission of radiation: Quantum generation of coherent surface plasmons in nanosystems," Physical Review Letters **90**, 027402 (2003).

[119] C. Kittel, *Introduction to Solid State Physics, 8th ed.* (Wiley: New York, 2005).

[120] F. von Cube, J. Niegemann, S. Irsen, D. C. Bell, and S. Linden, "Angular-resolved electron energy loss spectroscopy on a split-ring resonator," Physical Review B **89**, 115434 (2014).

[121] A. Hoerl, A. Truegler, and U. Hohenester, "Tomography of particle plasmon fields from electron energy loss spectroscopy," Physical Review Letters **111**, 076801 (2013).

[122] O. Nicoletti, F. de la Pena, R. K. Leary, D. J. Holland, C. Ducati, and P. A. Midgley, "Three-dimensional imaging of localized surface plasmon resonances of metal nanoparticles," Nature **502**, 80–84 (2013).

[123] G. Herink, D. R. Solli, M. Gulde, and C. Ropers, "Field-driven photoemission from nanostructures quenches the quiver motion," Nature **483**, 190–193 (2012).

[124] A. Aubry, D. Y. Lei, A. I. Fernandez-Dominguez, Y. Sonnefraud, S. A. Maier, and J. B. Pendry, "Plasmonic light-harvesting devices over the whole visible spectrum," Nano Letters **10**, 2574–2579 (2010).

[125] N. Grünwald, "Fabrication and characterisation of double layer plasmonic nanostructures on silicon nitride membranes," Master's thesis, University of Bonn (2013).

[126] T. P. Meyrath, T. Zentgraf, and H. Giessen, "Lorentz model for metamaterials: Optical frequency resonance circuits," Physical Review B **75**, 205102 (2007).

Publications

Parts of this work have already been published in refereed scientific journals

- F. von Cube, J. Niegemann, S. Irsen, D. C. Bell, and S. Linden, "Angular-resolved electron energy loss spectroscopy on a split-ring resonator," Physical Review B **89**, 115434 (2014).

- M. Husnik, F. von Cube, S. Irsen, S. Linden, J. Niegemann, K. Busch, and M. Wegener, "Comparison of electron energy-loss and quantitative optical spectroscopy on individual optical gold antennas," Nanophotonics **2**, 241–245 (2013).

- F. von Cube, S. Irsen, R. Diehl, J. Niegemann, K. Busch, and S. Linden, "From isolated metaatoms to photonic metamaterials: Evolution of the plasmonic near-field," Nano Letters **13**, 703–708 (2013).

- F. von Cube, S. Irsen, J. Niegemann, C. Matyssek, W. Hergert, K. Busch, and S. Linden, "Spatio-spectral characterization of photonic meta-atoms with electron energy-loss spectroscopy [Invited]," Optical Materials Express **1**, 1009–1018 (2011).

Additional work on other topics has been published in refereed scientific journals

- H. Steigerwald, F. von Cube, F. Luedtke, V. Dierolf, and K. Buse, "Influence of heat and UV light on the coercive field of lithium niobate crystals", Appl. Phys. B **1**01, 535-539 (2010).

- H. Steigerwald, M. Lilienblum, F. von Cube, Y. J. Ying, R. W. Eason, S. Mailis, B. Sturman, E. Soergel, K. Buse "Origin of UV-induced poling inhibition in lithium niobate crystals" Phys. Rev. B **82**, 214105 (2010).

Acknowledgments

First of all I would like to thank Prof. Dr. Stefan Linden for giving me the opportunity to write my PhD thesis in his group. He was an excellent teacher and we have had many fruitful discussions, which definitely contributed to the success of my thesis. He gave me diverse opportunities to present my work at international conferences, and put a lot of trust in me and my work.

I also want to thank my co-advisor Dr. Stephan Irsen. His profound knowledge of electron microscopy was of great help and mandatory for my experiments −in particular in the beginning of my studies. I also owe him a lot for establishing the connection for my studies abroad.

I want to express my gratitude to Prof. Dr. David C. Bell for welcoming me at Harvard and for providing everything that was needed. I am looking forward to our next project. I would like to thank PD. Dr. Elisabeth Soergel for kindly agreeing to co-referee this thesis. I thank PD. Dr. Metsch, for being the third member of my thesis committee and I thank Prof. Dr. Ulrich B. Kaupp for his engagement regarding my DAAD-scholarship, his support at caesar and for being part of my thesis committee.

Prof. Dr. Kurt Busch, Dr. Richard Diehl, and in particular Dr. Jens Niegemann were responsible for the simulations in this work. I am grateful for their work, and the good communication, especially concerning the four papers published along the way.

I would also like to thank Dr. Martin Husnik, who was responsible for the optical experiments, and his supervisor Prof. Dr. Martin Wegener for the excellent collaboration.

I want to thank Dr. Niels Feth, who introduced me to the EBL process and provided a set of samples which allowed for a quick start of my experiments.

I would like to thank all members of the Linden, Irsen, and Bell groups for their support and the numerous discussions. In particular I want to thank the diploma/master students I had the pleasure to work with: Thorsten Weber and Nikolas Grünwald. I also thank Johannes Overbuschman, Manuel Peter, and Estelle Kalfon-Cohen (one representative for each group) mostly for their non-thesis related support.

I am indebted to all proof readers of this thesis for their supporting comments and hints which improved the readability.

Last, but not least, I would like to thank my parents and siblings for their support throughout my life. I would like to thank my wife Julia for her understanding and love during the past years. Her support and encouragement was in the end what made this thesis possible.